3-24-2016

Spectroscopic Measurement of Gas Temperature in Small Internal Combustion Engines

Matthew J. Deutsch

SPECTROSCOPIC MEASUREMENT OF GAS TEMPERATURE IN SMALL INTERNAL COMBUSTION ENGINES

THESIS

Matthew J. Deutsch, Captain, USAF

AFIT-ENY-MS-16-M-207

DEPARTMENT OF THE AIR FORCE
AIR UNIVERSITY

AIR FORCE INSTITUTE OF TECHNOLOGY

Wright-Patterson Air Force Base, Ohio

AFIT-ENY-MS-16-M-207

SPECTROSCOPIC MEASUREMENT OF GAS TEMPERATURE IN SMALL INTERNAL COMBUSTION ENGINES

THESIS

Presented to the Faculty

Department of Aeronautics and Astronautics

Graduate School of Engineering and Management

Air Force Institute of Technology

Air University

Air Education and Training Command

In Partial Fulfillment of the Requirements for the

Degree of Master of Science in Aeronautical Engineering

Matthew J. Deutsch, BSME

Captain, USAF

March 2016

AFIT-ENY-MS-16-M-207

SPECTROSCOPIC MEASUREMENT OF GAS TEMPERATURE IN SMALL INTERNAL COMBUSTION ENGINES

Matthew J. Deutsch, BSME

Captain, USAF

Committee Membership:

Dr. Marc D. Polanka
Chair

Dr. Kevin C. Gross
Member

Dr. Fred Schauer
Member

Dr. Andrew W. Caswell
Member

Abstract

Internal Combustion Engines (ICE) revolutionized transportation at the dawn of the 20th century. Continuous refinement of the theory and design of ICE has allowed them to become so well optimized to the task of human transport that they are often taken for granted, only thought of on the rare occasion when they fail to work properly. Nobody speaks about the challenge of designing an ICE that is acceptable for the task of moving people from one place to another. Today, in the age of the remotely piloted aircraft (RPA), another opportunity arises to instigate the continuous refinement of the ICE to a novel task. Small ICE have been used to propel small model aircraft for decades, but the recent exponential growth in demand for RPA in military applications has given rise to an expectation from small ICE which far surpasses current capabilities: RPA require the ability to operate at higher altitudes, in more extreme environmental conditions, and with greater fuel efficiency than is currently possible. Small internal combustion engines, particularly those ranging in power from 1 kW to 15 kW, propel many Group 1 and Group 2 remotely piloted aircraft (RPA) platforms that play an increasingly significant role in the Department of Defense. Most engines used for defense applications are commercial off-the-shelf products, designed for hand tools and hobby aircraft. Efficiency of these engines is low and thermal loss is a significant contributor to the energy loss. Existing thermal energy loss models are based on data from much larger engines. Whether these loss models scale to the engine size class of interest, however, has not yet been established. The Small Engine Research Bench (SERB) was used previously to measure spatially and temporally averaged heat flux, as well as local, instantaneous heat flux at several external locations, for a series of small engines. This investigation will obtain time averaged crank-angle-resolved measurements of the in-cylinder gas temperature using Fourier transform infrared (FTIR) absorption thermometry. The results, coupled with heat flux measurements, will enable the validation or refinement of existing thermal energy loss models.

Acknowledgements

I would like to thank my faculty advisor, Dr. Marc Polanka, for his expert guidance and support throughout the course of this thesis effort. I am also indebted to Capt Joseph Ausserer for his daily support. I thank Mr. Paul Litke, Dr. Keith Grinstead, Dr. Andrew Caswell, Dr. Keith Rein, Mr. Richard Ryman, and Mr. Jacob Baranski for their assistance. I thank Dr. Kevin Gross, Dr. Cameron Keenan, and Mr. Michael Rhoby for their support with spectral fitting code. Also, "Danke vielmals" to Mr. Peter Wintrich of Modellmotoren for providing technical drawings of the 3W-55i. Finally, I thank my wife, Anna, and daughters, Felicity and Lorelei, for their love, support, patience, and understanding (and for begging me to refer to one of my frequently-recurring plots as the "intersmearogram").

~ Matthew J. Deutsch

Table of Contents

List of Figures

List of Tables

List of Equations

Nomenclature

A	Absorbance
AFRL	Air Force Research Lab
aTDC	after top dead center
B	bore
BDC	bottom dead center
bTDC	before top dead center
c_p	specific heat at constant pressure
CI	Compression Ignition
DAQ	data acquisition device
EFL	effective focal length
FT	Fourier transform
FTIR	Fourier transform infrared
h	convective heat transfer coefficient
HCCI	homogeneous-charge compression ignition
I	single-beam spectrum
I_o	background spectrum
ICE	internal combustion engine
ILS	instrument line shape
IMEP	indicated mean effective pressure
IR	infrared
k	thermal conductivity
l	optical path length
L	stroke
M	molecular weight
N	rotational speed of the engine

NA	numerical aperture
Nu	Nusselt Number
OAP	off-axis parabolic
OPD	optical path difference (δ)
Pr	Prandtl number
$\dot{q}$	heat flux
R	ratio of the connecting rod to the crank radius
$\tilde{R}$	universal gas constant
r_c	compression ratio
Re	Reynolds number
RPM	revolutions per minute
RTD	resistance temperature detector
$\bar{S}_p$	mean piston speed
SERB	Small Engine Research Bench
SERL	Small Engine Research Lab
SI	spark ignition
SNR	signal-to-noise ratio
T	Transmittance
TDC	top dead center
WOT	wide-open throttle
δ	optical path difference (OPD)
Δ	mirror displacement
Δ_{max}	maximum mirror displacement
$\Delta\tilde{\nu}$	spectral resolution, cm^{-1}
λ	wavelength
μ	viscosity
$\emptyset$	equivalence ratio

ρ	density
θ	crank angle
$\tilde{\nu}$	wavenumber, cm^{-1}

I. Introduction

This thesis presents the application of Fourier transform infrared (FTIR) spectroscopy to thermodynamic and combustion events in a small ICE to calculate a representative gas temperature in the combustion chamber. Small ICE are defined as those which produce between 1 and 10 kW of power. The acronym FTIR is used throughout this document to refer to either the procedure or the instrument used to carry out the procedure. The primary objective of this research was to measure crank-angle-resolved, in-cylinder, bulk gas temperature in a small ICE. Such measurements can be used to validate or modify existing models and correlations for thermal losses. These, in turn, will contribute to a bigger-picture understanding of how energy loss mechanisms scale with ICE size.

An FTIR was used to determine the in-cylinder temperature because it was capable of measuring much broader spectra than are possible with laser techniques and benefitted from throughput and multiplexing advantages over grating spectrometers. FTIR measurements, however, require some finite amount of time to collect a single data point. If the subject of the measurement changes in that time, the data is corrupted. For this reason, it is not a technique typically pursued for dynamic measurement environments like the cylinder of an engine. The advantages of FTIR stated above have driven the development of work-arounds for this issue that work well for repeatable, cyclical processes like an engine cycle [7, 8]. One of these methods was implemented to make in-cylinder FTIR measurements possible.

The remainder of Chapter I provides and introductory discussion of the research. Section 1 is background information that highlights the significance of the research. Section 2 details the complete problem statement. Section 3 discusses the research objectives and scope. Section 4 briefly describes similar efforts in the literature and explains how this research is unique. Section 5 explains the organization of the remainder of this thesis.

1. Background

The drone market is currently exploding. The industry is expected to create 10,000 jobs per year and $8.2 billion per year in the next decade [9]. Many of the most transformative

platforms could be classified as small RPA, which in this document is meant to include less than 100 lbs. [5] Small ICE are commonly used as the power plants for small RPA so as the industry grows so too will the demand for small ICE.

The rise in demand reveals a need for basic research because little has yet been published about small ICE. Fuel conversion efficiency hovers around or below 10 % for ICE of this size. With energy density being 13,000 W-hr/kg for typical hydrocarbon fuels, there is an opportunity to realize tremendous gains in range, endurance, and operating cost of small RPA with modest improvements to the fuel conversion efficiency of small ICE.

Fuel conversion efficiency is improved by reducing energy losses. Many energy loss mechanisms are worth examination, but thermal losses in particular account for an increasing portion of the total energy losses as ICE size decreases. Temporally and spatially averaged thermal losses have been quantified for small ICE on the Small Engine Research Bench (SERB). Models and correlations can be developed for the crank-angle-resolved thermal losses through the cylinder wall, but such models depend on some estimate of the crank-angle-resolved, in-cylinder, bulk gas temperature to model the thermodynamic properties of the gas as a function of crank angle. While such temperature profiles can be estimated analytically, the models would benefit from experimental bulk gas temperature measurements.

2. Problem Statement

Little has been published on the measurement of the crank-angle-resolved, in-cylinder gas temperature of small ICE. One reason for this is because the scale of the engines in this size class makes the measurement difficult. Optical diagnostics must be used to remain nonintrusive, but even the modifications necessary for optical access can significantly affect the in-cylinder gas dynamics in small ICE. Another reason for the gap in published data is that there has been little interest. With the growing demand for small RPAs, however, this research has become more relevant. Crank-angle-resolved gas temperature measurements are required to model crank-angle-resolved heat loss in ICE. Such measurements in small ICE will contribute to a better understanding of how power loss mechanisms scale with engine size.

3. Research Objectives and Scope

The overarching objective of this research was to measure the crank-angle-resolved, cycle-averaged, in-cylinder, bulk gas temperature of a small ICE. This objective was broken down into four subordinate objectives: modify a small ICE to create robust, indefinite optical access to the combustion chamber, integrate a precision optical alignment system into the existing small engine research bench, develop and implement a methodology to measure gas temperature with a non-intrusive optical technique, and measure the effects of various changes to the operating condition.

The scope of this research was measurements in a single air-cooled, fuel-injected, 55 cc, two-stroke ICE. The measurements were taken at several operating speeds, combustion phasing settings, and with two fuels to examine the effects of these variables on the temperature profiles.

4. Uniqueness and Significance

To the author's knowledge, FTIR absorption spectroscopy has never before been applied to small ICE (1 – 10 kW). The scale of the combustion chamber presented a design challenge for which many considerations had to be made, as will be described in Chapter III, the optical engine was capable of running for hours, at multiple conditions, without stopping to replace or clean optical components, due to the robustness of the final design. The crank-angle-resolved temperature profiles measured at various operating conditions as a result of this research provide insight into the effects of varying combustion phasing, engine speed, and fuel octane number. Furthermore, the crank-angle-resolved temperature profiles are a key component for the development and validation of heat loss models and correlations, which could fill a gap in the literature on small ICE.

5. Organization

Chapter II provides a review of the key concepts and literature applicable to this research. Chapter III is a detailed description of the experimental setup and the process of producing gas temperature from raw data. Chapter IV is a discussion of the results of this research. Chapter V draws conclusions and suggests areas of future research.

II. Literature Review

This chapter provides a review of the literature on all subjects relevant to the research, to include similar research efforts completed elsewhere. The topics of discussion are centered by the objective of the research: obtain crank-angle-resolved, in-cylinder, bulk gas temperature in a small ICE. Section 1.4 provides some general background literature on the subject of in-cylinder gas temperature. Section 3 dives into relevant measurement techniques. Section 4 discusses the basics of Fourier Transform Infrared (FTIR) spectroscopy.

1. Small Internal Combustion Engines

Pulkrabek defines an internal combustion engine (ICE) very succinctly as "a heat engine that converts chemical energy in a fuel into mechanical energy, usually made available on a rotating output shaft." [10] ICE can be categorized in many ways: spark ignition (SI) and compression ignition (CI), two-stroke and four-stroke, size, number of cylinders, arrangement of cylinders, air intake process, method of fuel input, fuel used, method of cooling, intended application, and many more. This review will not attempt to cover the full breadth of the literature on ICE. It will focus on the specific attributes and operating characteristics of the Modellmotoren 3W-55i (Figure 1), the ICE selected for this research.

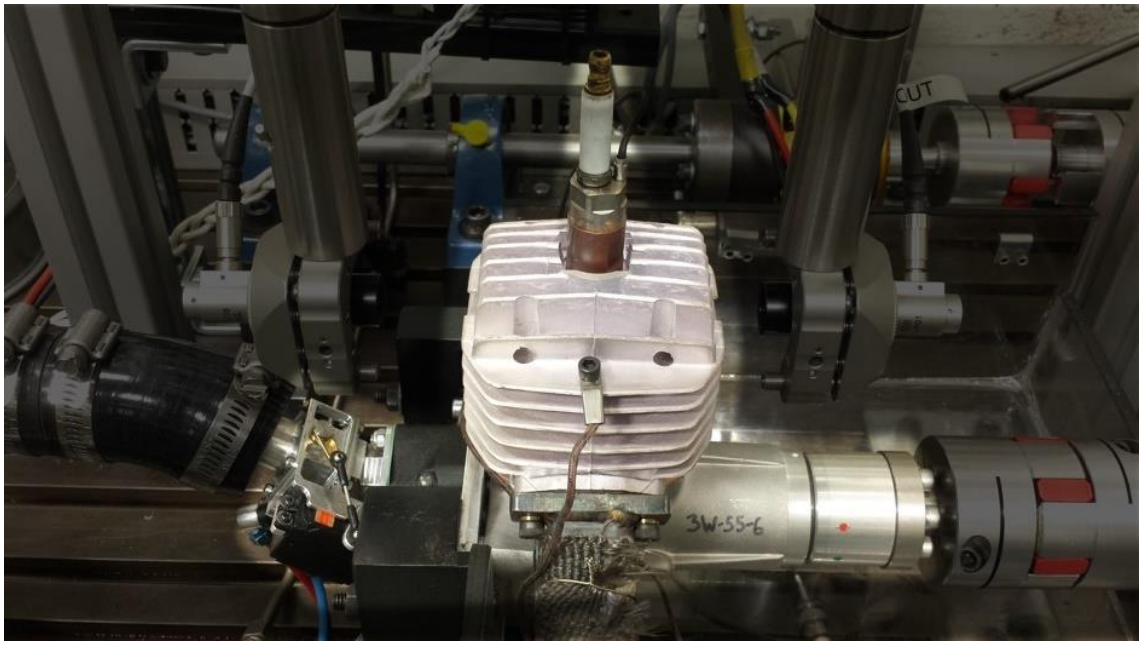

Figure 1. The Modellmotoren 3W-55i ICE.

1.1. Terminology

Before any further discussion the 3W-55i and how it operates, it is necessary to list the key components of the ICE. Figure 2 shows the features that can be seen from the exterior. The 3W-55i has a single cylinder. The cylinder is combined with the head, which means the head is not a separate part that can be removed from the rest of the cylinder as is often the case with ICE. The presence of a spark plug indicates that this is an SI engine. Cooling fins surround the cylinder on the sides and the top. The exhaust port directs exhaust flow away from and normal to the axis of the crankshaft, which in this picture would be directly out of the page. The crankcase houses the crankshaft, main bearings, connecting rod, piston, and reed valve. Upstream of the engine, in the air intake manifold, there is a fuel injector and a throttle body.

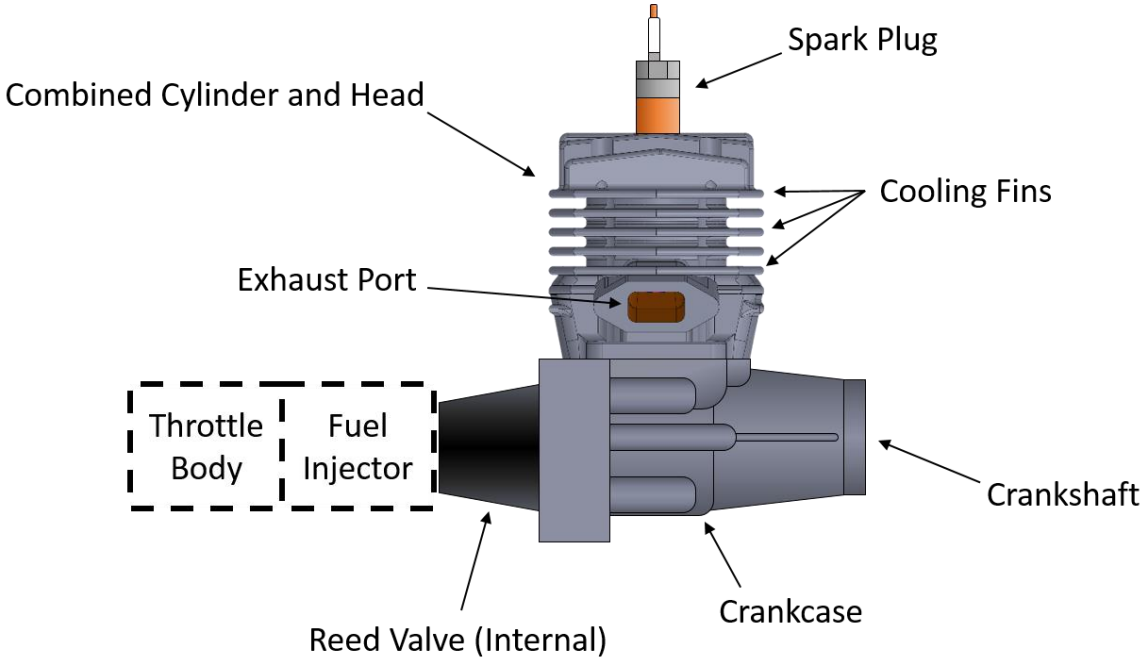

Figure 2. Primary external features of the 3W-55i.

Figure 3 shows cross-sections of the 3W-55i cylinder from two perspectives. These are labeled “back” and “left”, with “front” being the perspective given in Figure 1 and Figure 2. These perspectives are chosen to show the details of the three scavenging ports. Figure 4 is a generalized diagram of a crankcase-scavenged, two-stroke cycle ICE. This figure shows the remaining internal features of the engine. The diameter of the cylinder is called the *bore* (B), and the maximum distance traveled by the piston is called the *stroke* (L).

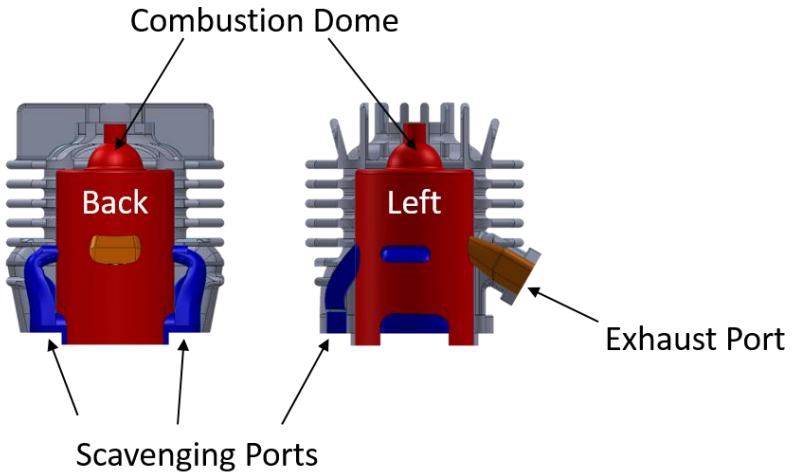

Figure 3. Primary internal features of the 3W-55i cylinder

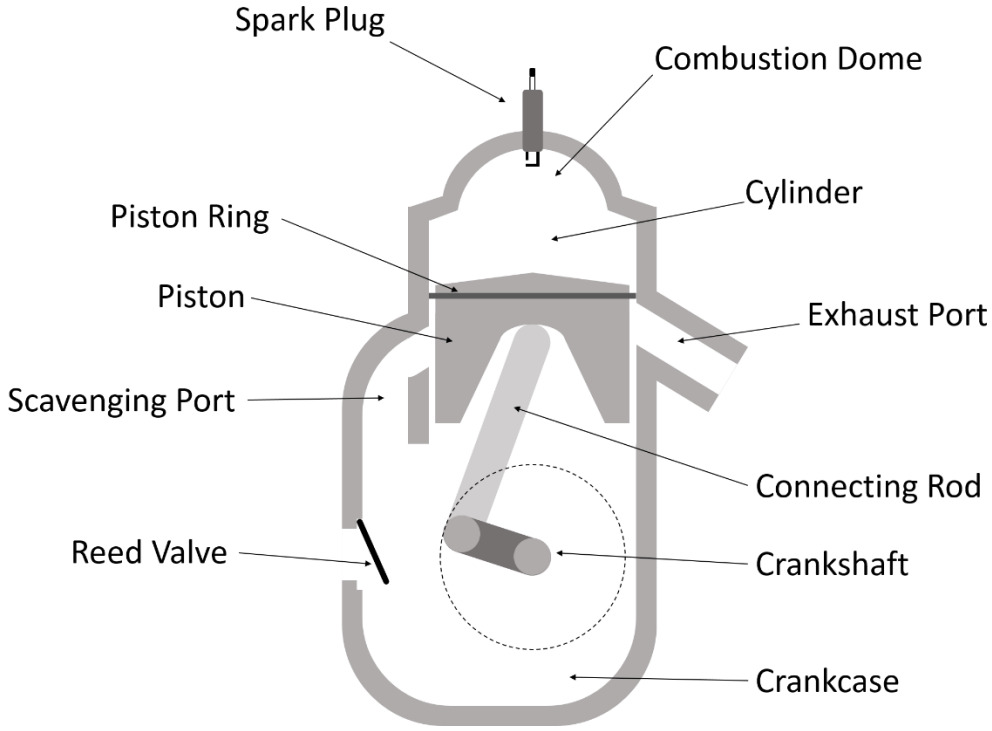

Figure 4. Primary internal features of a crankcase-scavenged, two-stroke ICE.

1.2. Spark Ignition

The 3W-55i is an SI engine. This means that the combustion process is initiated by a spark (the Otto cycle). This is as opposed to a CI engine, in which the combustion process is initiated by compression of the gas and auto-ignition (the Diesel cycle). The spark produces a flame kernel that expands through chain reaction to combust the entire air-fuel mixture in the cylinder. The combustion event begins slowly as the temperature and pressure build in the flame

kernel, until a critical point where the flame front expands rapidly, then slows again until it is quenched as the gas expands, the cold cylinder walls are reached, and the fuel-air mixture is spent.

1.3. The Two-Stroke Cycle

The 3W-55i is a crankcase-scavenged two-stroke ICE with scavenging and exhaust ports built into the cylinder walls to control the gas exchange process. A two-stroke cycle uses a single revolution of the crank shaft for each cycle. This is accomplished by consolidating the gas exchange process to a short period between expansion due to combustion and the compression of the next fresh charge. This gas exchange can be achieved with valves, as in a four-stroke engine, but more commonly employs ports built into the walls of the cylinder, as is the case with the 3W-55i. A crankcase-scavenged engine employs the downward stroke of the piston to compress fresh charge in the crank case, which forces the gas to flow through scavenging ports into the cylinder. This section walks through a full engine cycle in detail.

The engine cycle begins part-way through the upward stroke of the piston, with a homogeneous mixture of air and fuel trapped in the cylinder. This is shown in Figure 5. As the piston continues upward the air-fuel mixture in the cylinder is compressed. This process of *compression* causes rises in pressure and temperature. Beneath the piston, the crank case is simultaneously expanded, causing the pressure in the crank case to be lower than atmospheric pressure. The pressure differential forces a reed valve open, which allows fresh air-fuel mixture from the intake manifold to flow into the crank case and normalize the pressure. This process is called *induction*. Compression and induction continue for the full duration of the upward stroke of the piston. [11]

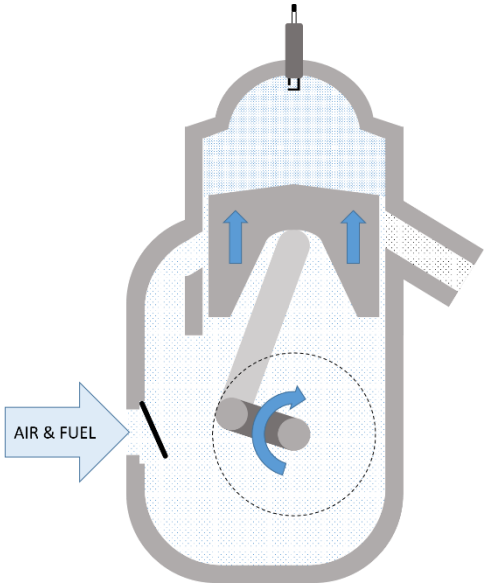

Figure 5. Engine cycle step 1 of 8: compression of the air-fuel mixture in the cylinder.

Near the end of the upward stroke of the piston an electric charge creates a spark across a gap in a spark plug, in the combustion dome. This spark provides the activation energy required to ignite the air-fuel mixture, which develops into a small flame kernel. Compression and induction continue. This step is shown in Figure 6. [11]

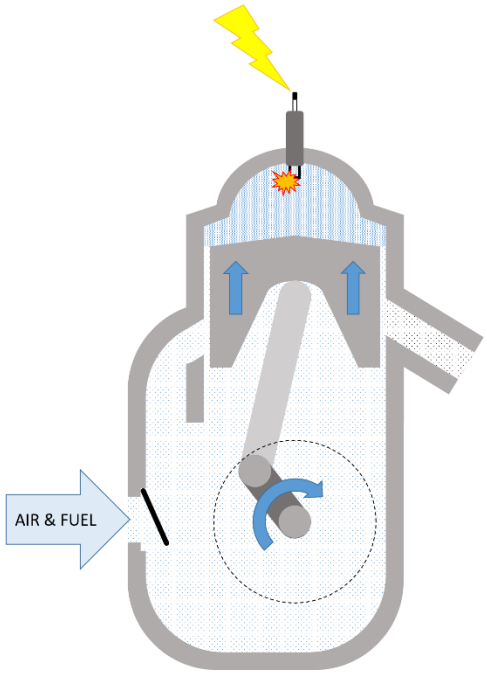

Figure 6. Engine cycle step 2 of 8: spark, ignition, and induction.

The highest position reached by the piston is called top dead center (TDC). This position is shown in Figure 7. TDC marks the end of compression and induction. It also marks the beginning of expansion of the cylinder, compression of the crank case, and typically rapid burning in the combustion dome. [11]

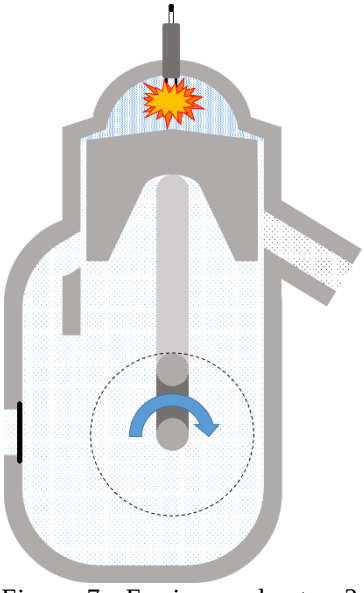

Figure 7. Engine cycle step 3 of 8: rapid burn begins.

Figure 8 shows the beginning of the power stroke, the downward stroke of the piston. Combustion causes rapid pressure rise in the gas, which drives the piston downward, which turns the crankshaft and produces useful power. The piston is simultaneously compressing the crank case, causing the pressure to rise above atmospheric pressure. As the power stroke continues, the combustion flame front begins to reach the cold cylinder walls and run out of combustible mixture. Expansion of the in-cylinder gas with the downward stroke of the piston also acts to reduce the temperature and pressure. The combination of these factors begins the process of flame quenching, as shown in Figure 9. Compression of the crank case continues. [11]

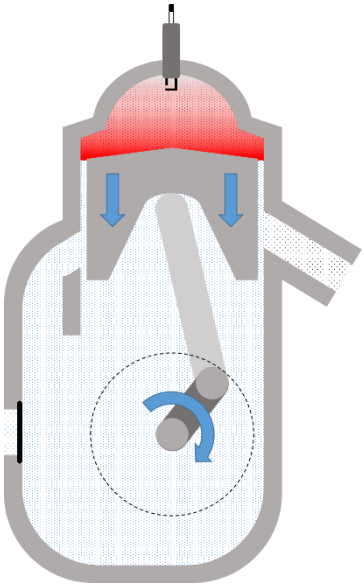

Figure 8. Engine cycle step 4 of 8: power stroke begins, rapid burn continues, air-fuel mixture in the crank case is compressed.

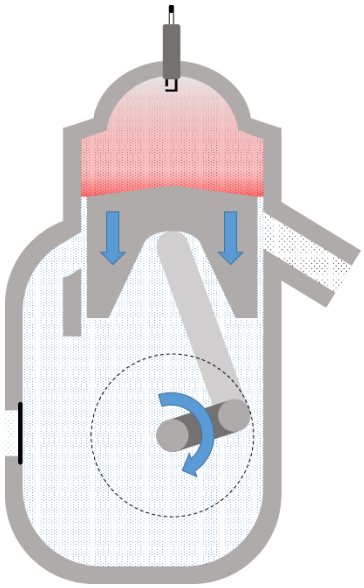

Figure 9. Engine cycle step 5 of 8: rapid burn ends, power stroke and compression continue.

As the combustion begins to slow the exhaust port opens. This is shown in Figure 10.

The in-cylinder exhaust is at a much greater pressure than the gas in the exhaust port, which is at

roughly atmospheric pressure. The pressure differential causes some of the exhaust to flow out through the exhaust port until the pressures are equalized, in a process called *blowdown*. [11]

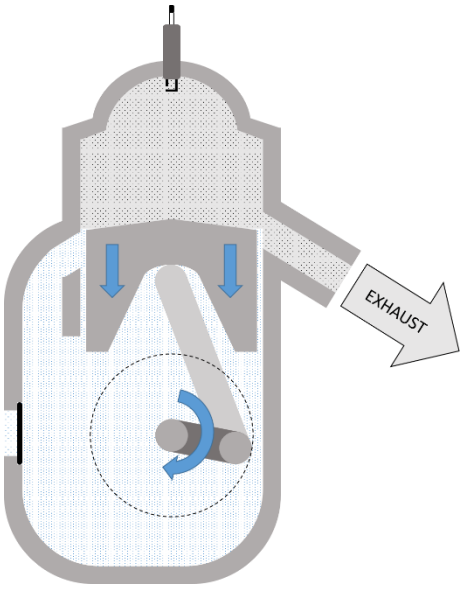

Figure 10. Engine cycle step 6 of 8: exhaust port opens, blowdown occurs.

After the exhaust port opens, one or several scavenging ports open. These ports allow compressed air-fuel mixture from the crank case to flow up into the cylinder and force more of the exhaust out the exhaust port in a process called scavenging. Scavenging is illustrated in Figure 11. This figure also shows the piston in its lowest position, called bottom dead center (BDC). This marks the end of the downward stroke and beginning of the upward stroke of the piston. Scavenging continues through the beginning of the upward stroke until the scavenging ports close. This step is shown in Figure 12. The exhaust port is still open for a short time after the scavenging ports close, allowing more exhaust to escape. It is worth noting that nothing prevents fresh air-fuel mixture from also escaping through the exhaust port. This loss mechanism is called *short circuiting* and is a significant source of energy loss in many two-stroke engines. When the upward stroke of the piston finally closes the exhaust port the cycle has begun again. [11]

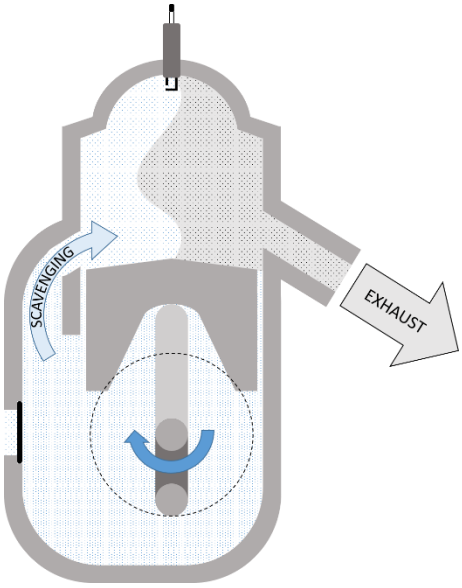

Figure 11. Engine cycle step 7 of 8: scavenging port opens, gas exchange begins.

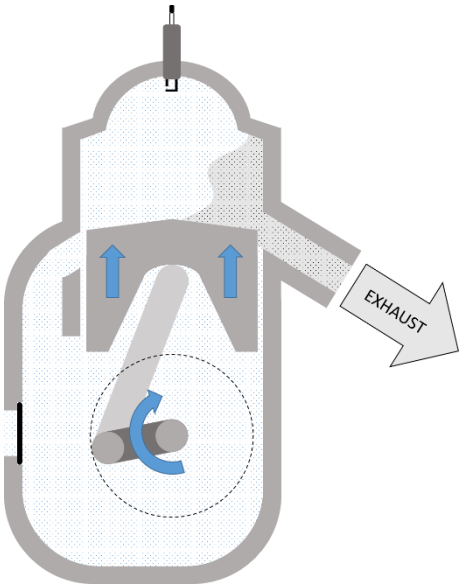

Figure 12. Engine cycle step 8 of 8: scavenging port closes, gas exchange continues.

1.4. Fuel Delivery

The 3W-55i is a carbureted ICE in its stock configuration, but was modified with an aftermarket throttle body fuel injector for this research. This modification improved the operator control of equivalence ratio through a broad range of operating conditions. With the fuel injector, a metered amount of fuel is pumped into the air intake manifold, just downstream of the

throttle plate and upstream of the reed valve. The timing and duration of the injection are set to maximize vaporization of the fuel and control the equivalence ratio. Lubricating oil is mixed in with the fuel and therefore delivered to the lubrication points via the flow of fuel through the engine.

1.5. Thermal Management

The 3W-55i is an air-cooled ICE. Some form of thermal management is required to draw thermal energy away from the engine cylinder and prevent overheating of critical components. Air-cooled ICE force air across cooling fins all around the hottest parts of the engine. The heat is transferred to the cool air, which is drawn away from the engine. Other engines circulate coolant through cavities in the cylinder walls, then through a radiator. Air is forced across cooling fins on the radiator where the heat is transferred to the cool air, which is then drawn away from the engine. Air-cooled ICE are typically lighter and have fewer, simpler components, making this the ideal thermal management system for ICE in small RPA.

1.6. Thermal Loss Models

Hot gas in an ICE cylinder transfers heat to its surroundings via convection and radiation. From the cylinder wall heat is transferred via conduction to the cooling fins, where it is transferred to the cooling air flow via convection. Figure 13, from Heywood [11], illustrates the flow path of heat through the cylinder wall and into a cooling flow. In this figure, subscripts CN, CV, and R indicate conduction, convection, and radiation, respectively. Subscripts g, w, and c indicate gas, wall, and coolant. The over bar indicates a bulk temperature for the associated flow.

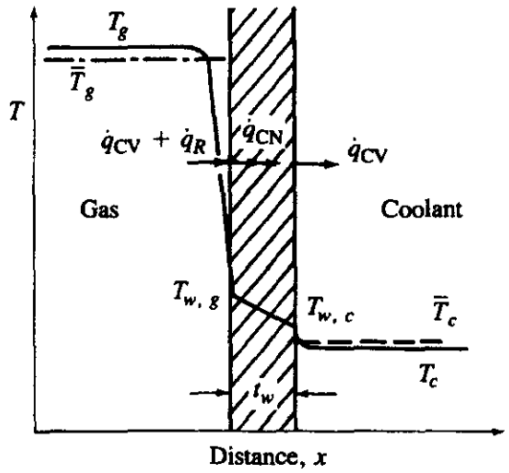

Figure 13. Illustration of heat transfer from the hot in-cylinder gases to the cooling flow reproduced from Heywood.

The heat-transfer process is typically assumed to be quasi-steady, so the one-dimensional, gas-side heat flux is expressed as stated in Eq. (1)

$$\dot{q} = \dot{q}_{CV} + \dot{q}_R = h\left(\bar{T}_g - T_{w,g}\right) + \sigma\varepsilon(\bar{T}_g^4 - T_{w,g}^4) \tag{1}$$

where $\dot{q}$ is heat flux, h is a convective heat transfer coefficient, T is temperature, σ is the Stefan-Boltzmann constant, and ε is the emissivity of the in-cylinder gas. Typically, the radiation term is negligible, and therefore neglected during analysis [11].

1.6.1. Dimensional Analysis

Dimensional analysis can be employed to aide in solving for or predicting the heat transfer coefficient for a given condition. Equation (2) presents the typical parameterization used for ICE heat transfer correlations.

$$F\left(\frac{hB}{k}, \frac{\rho\bar{S}_p B}{\mu}, \frac{c_p\mu}{k}, \frac{B}{L}, \frac{\dot{q}_{ch}}{\rho c_p NT}, r_c, R, y_1, \cdots, y_m, \theta, u_1, \cdots, u_n\right) = 0 \tag{2}$$

The first three terms are the Nusselt number (Nu), Reynolds number (Re), and Prandtl number (Pr). The chosen characteristic length is bore B, which is the diameter of the cylinder. The characteristic velocity is the mean piston speed, $\bar{S}_p$. The thermal conductivity is k, ρ is the density, μ is the viscosity, c_p is the specific heat at constant pressure, and L is the stroke, the axial distance traveled by the piston to get from one position limit to the other. $\dot{q}_{ch}$ is the heat released

by the chemical reactions occurring during combustion. N is the rotational speed of the engine. r_c is the compression ratio of the cylinder, R is the ratio of the connecting rod to the crank radius, and θ is the crank angle. The y and u parameters are length and velocity ratios, respectively. They are often wrapped up into a single parameter with a different value for each category of ICE, as defined by the creator of the correlation. [11]

Correlations typically assume that the Nusselt, Reynolds, and Prandtl numbers are related in the same way they would be for a turbulent flow in a pipe or over a flat plate, taking the form of Eq. (3).

$$\mathrm{Nu} = a\,\mathrm{Re}^m\mathrm{Pr}^n \tag{3}$$

where a, m, and n are constants. [11]

1.6.2. Correlations for the Heat Transfer Coefficient

Heat flux can be analyzed as a temporally and spatially averaged quantity for the system, an instantaneous spatially averaged quantity, a local temporally averaged quantity, or an instantaneous local quantity. The following sections will discuss correlations for three of these four possibilities. The selection of a correlation depends on what data can be measured readily and what questions need to be answered. The critical choices to make when using the various heat-transfer correlations are the velocity to be used in the Reynolds number; the gas temperature at which the gas properties in Eq. (3) are evaluated; and the gas temperature to use in Eq. (1). [11]

1.6.2.1. Temporal Average Correlations

Taylor and Toong solved for temporally and spatially averaged heat transfer coefficients on four engines. They used the form of Eq. (3) to correlate the engine heat-transfer data. They next extended their correlation to heat-transfer data from various commercial engines spanning a broad range of size and type. Their correlation hinged on the definition of a temporally averaged internal gas temperature, Tg,a, as defined in Eq. (4). [12]

$$\int Ah\left(\bar{T}_g - T_{g,a}\right)d\theta = 0 \tag{4}$$

where A is the surface area of the cylinder. The impact of Prandtl number is considered to be negligible, and thus omitted from the final correlation (i.e., in Eq. (3) $n = 0$). Equations (5) and (6) step through the substitutions required to arrive at the formulas for Nusselt number and Reynolds number used by Taylor and Toong.

$$\mathrm{Nu} = \frac{hl}{k} = \frac{\bar{\dot{Q}}l}{A(T_{g,a} - T_c)k} = \frac{\bar{\dot{Q}}B}{(\pi B^2/4)(T_{g,a} - T_c)k} = \frac{4\bar{\dot{Q}}}{\pi B(T_{g,a} - T_c)k} \tag{5}$$

$$\mathrm{Re} = \frac{\dot{m}l}{\mu A} = \frac{\dot{m}B}{\mu(\pi B^2/4)} = \frac{4\dot{m}}{\pi\mu B} \tag{6}$$

where $\dot{m}$ is the temporally averaged mass flow rate through the cylinder. Based on their data, Taylor and Toong suggest using the values $a = 10.4$ and $m = 0.75$ for Eq. (3). [12] Annand suggested a value of $m = 0.7$. He also adjusted a based on ICE type and size. [13]

1.6.2.2. Instantaneous Spatial Average Correlations

Annand created a correlation based on published data on instantaneous heat fluxes to specific cylinder head locations. Equation (7) presents the form. [13] Note that the characteristic velocity for the Reynolds number is the mean piston speed, a temporally averaged value. The gas properties, however, are evaluated as functions of the instantaneous bulk gas temperature, as determined using Eq. (8), a simple ideal gas relation. Here p is the instantaneous pressure, V is the instantaneous volume, m is the mass of the in-cylinder gas, $\tilde{R}$ is the universal gas constant and M is the molecular weight of the in-cylinder gas, which is assumed to be the air-fuel mixture throughout the entire cycle. Annand proposed $b = 0.7$ and values of a ranging from 0.35-0.8, depending on the intensity of charge motion and engine design.

$$\frac{hB}{k} = a\left(\frac{\rho\bar{S}_p B}{\mu}\right)^b \tag{7}$$

$$\bar{T}_g = \frac{pVM}{m\tilde{R}} \tag{8}$$

This class of heat transfer correlation is particularly important to the current research because the instantaneous heat transfer coefficient for convection from the in-cylinder gas to the cylinder wall is determined largely based on an estimation of $\bar{T}_g$, the instantaneous bulk in-cylinder gas temperature. What was historically estimated with a crude ideal gas law

approximation is measured directly in this research via a non-invasive optical diagnostic technique.

1.6.2.3. Instantaneous Local Correlations

LeFeuvre et al. and Dent and Sulaiman propose using a flat plate forced convection model as in Eq. (9) when considering instantaneous, local heat transfer. [14, 15]

$$\left(\frac{hl}{k}\right) = 0.036\left(\frac{\rho v l}{\mu}\right)^{0.8}\left(\frac{c_p \mu}{k}\right)^{0.333} \tag{9}$$

Diesel ICE inject fuel directly into the pressurized air in the cylinder. These engines commonly depend on a high level of gas "swirl" to quickly mix and air. The swirl also has a significant impact on the heat transfer at any given point on the wall. If the swirl patterns are well known, Eq. (10) through Eq. (11) can be incorporated into Eq. (9) to account for them. [11] Making these substitutions and combining Eq. (9) with Eq. (1), if Pr = 0.73 then the result is Eq. (12). [15]

$$l = 2\pi r \tag{10}$$

$$v = r\omega \tag{11}$$

$$\dot{q}(r) = 0.023\frac{k}{r}\left(\frac{\omega r^2}{v}\right)^{0.8}\left[\bar{T}_g(r) - T_w(r)\right] \tag{12}$$

When considering instantaneous local correlations, it is important to account for the combustion event. During combustion, unburned gas and burned gas will both be present in parts of the cylinder. The temperature and velocity differences are significant. This can be accounted for with zonal modeling, which results in two heat-transfer equations to choose from, Eq. (13) and Eq. (14), depending on the zone of interest. [11]

$$\dot{Q}_u = A_{u,w} h_u (T_u - T_w) \tag{13}$$

$$\dot{Q}_b = A_{b,w} h_b (T_b - T_w) \tag{14}$$

It is possible to further divide the burned gas zone into an adiabatic core and a thermal boundary layer. Such a scheme can result in a more accurate model. Equation (15) implements the adiabatic core model. k_e is the effective thermal conductivity in the boundary layer, T_{ac} is the adiabatic core temperature, and δ is the boundary-layer thickness. [11]

$$\dot{q} = \frac{k_e(T_{ac} - T_w)}{\delta} \tag{15}$$

1.7. In-Cylinder Gas Temperature

According to Heywood, peak burned gas temperatures in ICE can be of order 2500 K. However, to avoid fatigue cracking, regions of high heat flux in the engine block must be kept at much lower temperatures: less than about 650 K for cast iron and less than about 550 K for aluminum alloys. The cylinder walls must remain less than about 450 K to prevent deterioration of the lubricating oil film. All of these requirements result in heat fluxes to the cylinder walls as high as 10 MW/m^2. [11]

It is important to note the limitations of a bulk gas temperature measurement in the cylinder of an ICE. During combustion and gas exchange, which account for the vast majority of the engine cycle, strong temperature and species concentration gradients exist within the cylinder. To create a heat transfer model, then, that calculates in-cylinder gas properties for a bulk gas temperature certainly departs from the physical reality of engine gas dynamics because the gas in the region of the cylinder walls, where the convective heat transfer occurs, will consistently be cooler than the calculated bulk gas temperature. This is a necessary departure, however, for practical engine diagnostics.

1.8. The Effect of ICE Scaling on Energy Loss Mechanisms

The energy inputs to an SI engine are the air-fuel mixture and a spark. The energy outputs are more numerous. Aside from the useful power out through the crankshaft, called the *brake power*, there are several energy loss pathways through the engine. These include pumping losses in the air intake manifold, crank case, and fuel injector, vibration, short circuiting, incomplete combustion, exhaust enthalpy, conduction of thermal energy through the cylinder

wall, and friction losses. Some of the primary energy pathways through the 3W-55i are highlighted in Figure 14.

The relative importance of each of these energy pathways changes as a function of engine size. For example, as ICE scale smaller the ratio of cylinder surface area to cylinder volume increases. Thermal losses through the cylinder wall are a function of surface area, but power generation is a function of volume. Consequently, thermal losses through the cylinder account for an increasing percent of total power generation as ICE scale smaller. The relative importance of the other energy loss mechanisms similarly change as a function of engine size.

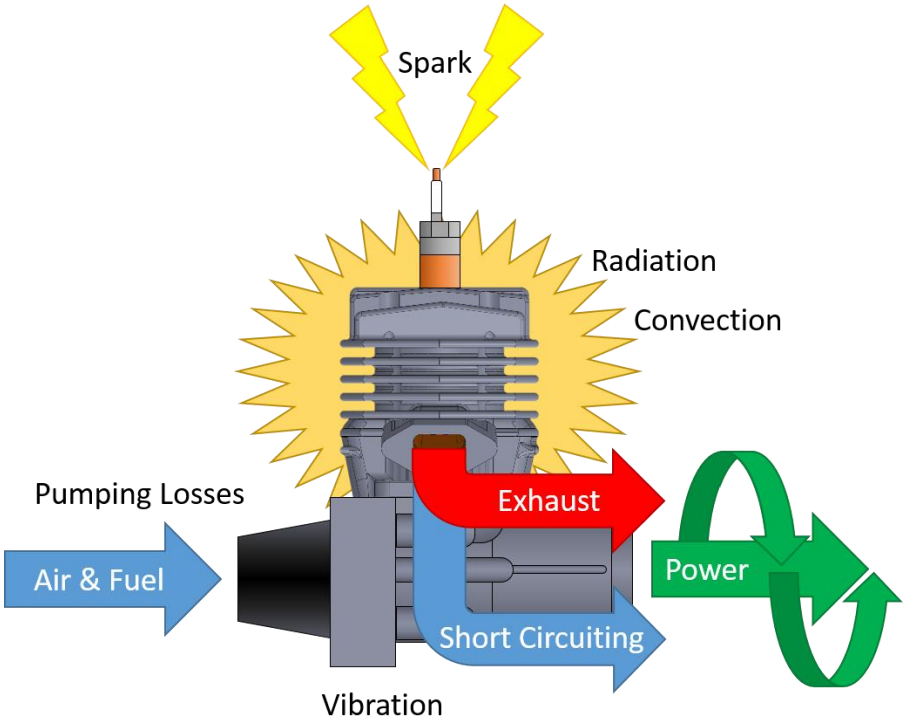

Figure 14. Summary of the energy pathways through a 3W-55i

Figure 15 indicated mean effective pressure (IMEP) as a function of ICE displacement volume, V_d. This plot shows that large ICE, with displacement volumes greater than 100 cc, follow a strong trend that is distinct from the strong trends observed in micro ICE, with displacement volumes less than one cubic centimeter. This suggests that somewhere between these two trends, with small ICE between 1 and 100 cc in displacement volume, there is a dramatic shift in the relative impact of various energy loss pathways, or the way those pathways

scale with size. Very little has been published about small ICE from which to resolve these unknowns. Furthermore, the demand for small ICE in small RPA applications is growing. If a better understanding of this transition region were to lead to small ICE designs with improved fuel conversion efficiency, the result would be significant gains in the range, duration, and affordability of small RPA.

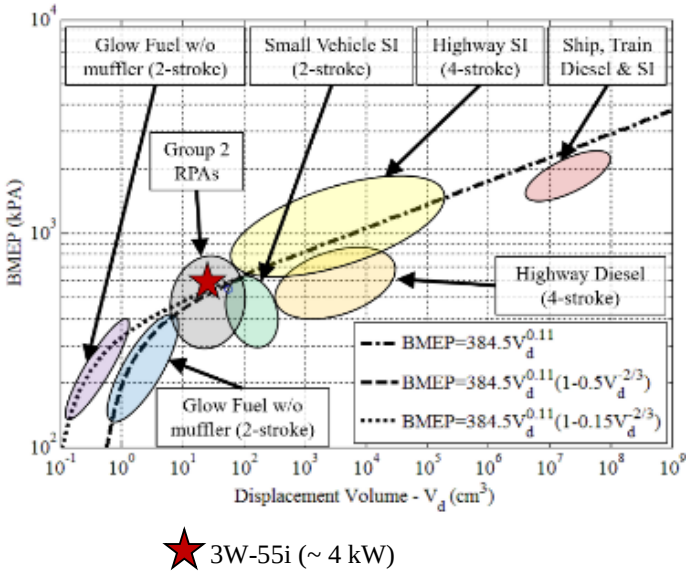

Figure 15. Figure from Ausserer, et al. [5], based on aggregated data from Menon & Cadou. [6]

2. The Small Engine Research Bench

The Small Engine Research Bench (SERB) was initially developed and validated for use in 2013 [16]. It was intended for small ICE in the 1 – 7 kW power output range, and designed specifically for three sizes of Modellmotoren 3W ICE: 28, 55, and 85 cc. Measurement capabilities began with torque, speed, power, and several key temperatures, pressures, and mass flowrates. The capabilities ultimately developed to include combustion analysis via spark plug pressure transducer and AVL Indismart software [17], drivetrain friction measurement [18], temporally and spatially averaged thermal loss quantification [19], and exhaust sampling for gas chromatography [5]. Studies have attempted to analyze ICE scaling effects [20]. The SERB is currently capable of quantifying what percent of fuel energy is converted into useful power and what percent is lost to cooling load, exhaust enthalpy, incomplete combustion, and short-

circuiting [5]. The SERB was modified for the purpose of this research to perform optical diagnostics. The details of these modifications are presented in Chapter III, Methodology, Section 2.

3. Optical Techniques for In-Cylinder Temperature Measurements

Many techniques may be considered for the measurement of crank-angle-resolved, in-cylinder gas temperature. However, according to Zhao [21]: "Since physical probes, such as thermocouples or thermistors, typically lack the necessary spatial resolution, time response, and durability, in-cylinder gas temperature measurements have been dominated by optical techniques." To this list of reasons for optical techniques one could add the potential for noninvasive in-cylinder measurements. For all of these reasons, this research considered optical techniques exclusively. Rein [22] breaks down the experimental design process for in-cylinder optical measurement techniques as a series of choices between light sources, light delivery methods, and spectroscopic instruments.

These design choices are informed by the spectral features one expects to find with in-cylinder gas measurements: emission features are only present during combustion; absorption and emission features are limited to those caused by the reactants and products of combustion. The specific requirements of the research can also play a role in these design choices: required level of accuracy, budget, schedule, data required, etc. Excepting these limitations, the experimental design choices become preferential, based on the experience and skill set of the research team, and the number of possible combinations of design choices leads to a broad field of experimental setups to consider. Section 3.1 provides some general information about electromagnetic radiation. The remainder of Section 3 summarizes Rein's coverage of the key design choices that must be made and provides some examples of in-cylinder gas temperature measurements from the literature.

3.1. Electromagnetic Radiation

Electromagnetic radiation, or light, is the self-sustaining coupling of a magnetic field and an electric field, which propagates itself through space. A beam of light transports both energy

and momentum. The electric field and magnetic field at any point in space are sinusoidal functions of time (usually sums of many sinusoids), and at any instant of time the spatial variation of the fields is also sinusoidal. The fields act orthogonally to one another and to the direction of propagation of the wave, as shown in Figure 16. [2]

When conceptualizing light it is convenient to limit the discussion to light of a single wavelength, or "monochromatic" light, even though a continuum of wavelengths are observed and studied in nature. A physical beam of light will always contain light of some combination and range of wavelengths. These concepts will be explored in greater detail later. For the moment the discussion will be limited to monochromatic light. It is also convenient to imagine a particle which travels at the speed of light and which allows a beam of light to transport momentum, as is observed in nature. This particle is called a photon by convention. Strictly speaking, a photon is a quanta of electromagnetic energy. [2]

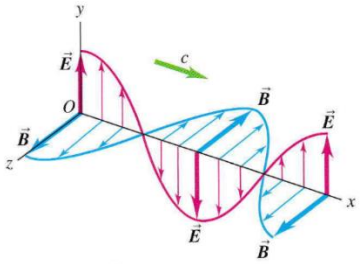

Figure 16. The complimentary electric and magnetic waves that propel a photon through space [2].

Imagine a photon traveling along the path of a beam of light. It rides on the crest of a coupled wave pair: an electronic wave and a magnetic wave that act in perpendicular planes to each other, and both in planes perpendicular to the path of the beam. This photon may or may not interact with atoms that it passes by, or through. When it does not interact, the light has been *transmitted* by the non-interacting medium. When it does interact, an atom will absorb the photon, which allows an electron to jump to a more excited state. In this case, the light has been

absorbed by the interacting medium. Conversely, when an electron falls from an excited state to a normal state, a photon is released. In this last case, light is *emitted* by the acting medium.

These three phenomena, transmission, absorption, and emission, can be quantified. Their values in any given system are dependent on the wavelength of light and the temperature, pressure, species concentration, and path length through the interacting or acting medium. If transmission, absorption, or emission are measured as a function of wavelength, analysis can be used to quantify the temperature, pressure, etc. that led to those measurements. This is the essence of spectroscopy.

3.2. Spectroscopy

According to Griffiths and de Haseth, *spectroscopy* is the science of obtaining qualitative and quantitative information from spectra. Spectroscopy strives to learn about matter by observing the intensity of a beam of light as a function of wavelength. The plot of light intensity as a function of wavelength is called a spectrum. Spectra measured experimentally can be compared to spectra from known substances and conditions to quantify properties of the substance under test, such as species, temperature, and pressure. The subject concerned with separating the electromagnetic radiation of various wavelengths, or measuring spectra, is referred to by Griffiths and de Haseth as *spectrometry* [7].

One can measure the spectrum emitted by a substance, or that which is transmitted by a substance. If one measures the spectrum of a light source, then compares it to the same light source after being transmitted through a substance of interest, the absorption of the substance is measured. The absorptivity, transmissivity, and emissivity of many gases have been characterized as functions of wavenumber, temperature, pressure, optical path length, and species concentration. This information has been collected into spectral databases. These databases make it possible to simulate any gas properties and plot the resulting simulated spectra. It is possible to determine the temperature and species concentration in a gas by comparing a measured spectrum to a series of simulated spectra by holding the known quantities constant,

varying the unknown quantities through a reasonable range, then searching for the simulated spectrum that best fits the measured spectrum, using some criterion for goodness of fit.

3.3. Experimental Design Choices

Available light sources include lasers, lamps, and natural emission. Lasers are powerful, directional light sources. They can, however, be expensive, difficult to use, and limited by narrow emission bandwidth. Lamps are generally inexpensive and provide flexibility with bandwidth, but typically emit in all directions and provide a less powerful signal than a laser. Natural emission can be a powerful tool, and engine combustion provides plenty of it. There is no emission during gas exchange, however, so if data is required for the full engine cycle another source must be used. [22]

Light can be transmitted through fibers or through free space. Fibers are useful when signal must be routed into tight spaces or harsh environments, but can be expensive and fragile. Fibers also cause some loss of signal. Transmission through free space can reduce the number of optical components required but, unless housed in a dark, purged casing, lead to increased absorption of the signal due to transmission through atmosphere. [22]

Spectrometers fall into two broad categories: dispersive instruments and interferometric instruments. Both ultimately measure the intensity of incident light as a function of wavenumber (or equivalently wavelength – they are inverses of each other). Dispersive instruments use grating, a prism, or some other technique to separate a beam into its various wavenumber components. Then the intensity of light of each wavenumber is measured separately. Interferometric instruments measure the intensity of a single beam of light that has been modulated – split into two equal parts with deliberate and controlled phase modulation – then recover the wavenumber-dependent light intensity information by taking the Fourier transform (FT) of the modulated light signal. For this reason, these instruments are also referred to as FT spectrometers. The FT is used in this context to transform information from the spatial domain (the spatial phase shift of the two beams of light) to the wavenumber domain. [22]

With dispersive instruments there is typically a tradeoff between spectral resolution and the range covered. Also, the degree to which light is dispersed by such an instrument is typically a nonlinear function of wavenumber that must be known and accounted for, or managed with additional resolution elements to minimize line shape errors. The range of an interferometric instrument is not dependent on the resolution desired, but rather the limitations of the optical components required to reflect, transmit, transport, and modulate the light, and the light itself. The resolution is determined solely by the maximum phase delay between the two parts of the modulated beam. There is no physical dispersion of light in an FT spectrometer so there is no concern about nonlinear, wavenumber-dependent instrument functions. [22]

Dispersive instruments can instantaneously collect data about specific wavenumbers of light, which gives them a distinct advantage over FT spectrometers for the dynamic gas sample encountered in engine data collection. FT spectrometers depend on the modulation of light through some amount of phase delay, which takes time. The sample must be static throughout the entire measurement time or the spectral information becomes some blurred combination of the time-dependent changes. This limitation can be worked around when the time-dependent changes in the sample subject are cyclically repeatable. [22]

FT spectrometers have two distinct advantages over dispersive spectrometers that can significantly improve the signal-to-noise ratio (SNR) of the resulting spectra. The first is the throughput, or Jacquinot, advantage. Whereas a dispersive instrument requires the signal to pass through some slit before reaching the detector, the FT spectrometer can direct the full beam signal to the detector. The second is the multiplex, or Fellgett, advantage. This is the ability of an FT spectrometer to sample all wavelengths of light at once with a single detector instead of being limited to some smaller set, based on the number of detector elements available as in a dispersive instrument. [23]

4. Fourier Transform Infrared Spectroscopy

The following discussion was inspired by similar discourse from several sources [7, 23, 24], but the figures are all original and the concepts and equations are all fundamental to the

subject unless otherwise stated. Fourier Transform Infrared (FTIR) Spectrometers take advantage of the wave properties of light in a unique way to achieve the separation of signals from various wavelengths. The heart of the device is a Michaelson Interferometer, like the one depicted in Figure 17. A light source is directed at a beam splitter, which reflects one half of the light toward a stationary mirror and transmits the other half toward a moving mirror. The mirrors reflect their respective beams of light back toward the beam splitter, which then reflects and transmits portions of each beam once again. Some light from each path is sent back toward the source, while the rest is sent through a sample and ultimately to a detector.

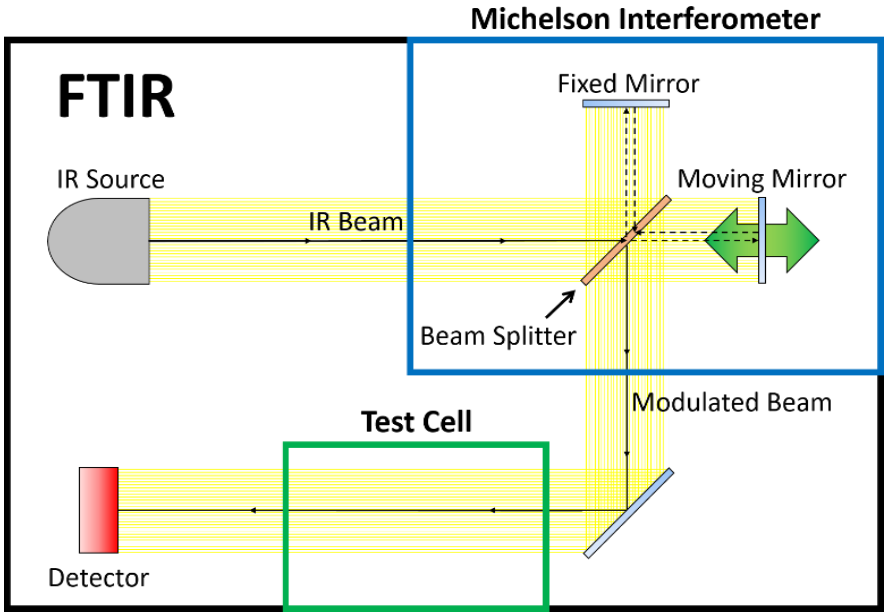

Figure 17. Primary components of an FTIR

When each mirror is the same distance away from the beam splitter, the two optical paths are perfectly in phase with each other. This is a condition called zero path difference (ZPD). At ZPD the intensity of light incident on the detector is be the same as the intensity of light emitted by the source, less any losses through the optical components between the two. As soon as the moving mirror departs from ZPD an optical path difference (OPD) is induced. OPD is equal to twice the displacement of the moving mirror, as characterized by

$$\delta = 2\Delta \tag{16}$$

where δ is the OPD and Δ is the displacement of the moving mirror from ZPD. A nonzero OPD implies some phase modulation has been introduced to the beam incident on the detector, which in turn causes destructive interference of certain wavenumbers of light. The OPD at which total destructive interference is observed for any wavelength is given by

$$\delta = \left(n + {}^{1}/_{2}\right)\lambda \tag{17}$$

where *n* is any integer, and λ is the wavelength of light that experiences total destructive interference. Conversely, the OPD at which total constructive interference (i.e. total lack of destructive interference) is observed for any wavelength is given by

$$\delta = n\lambda \tag{18}$$

Spectra collected with an FTIR are usually presented in terms of the wavenumber of the light as opposed to the wavelength. Wavenumber is simply the inverse of wavelength:

$$\tilde{\nu} = {}^{1}/_{\lambda} \tag{19}$$

where $\tilde{\nu}$ is the wavenumber and is typically reported in units of reciprocal centimeters, cm^{-1}.

The Michelson interferometer performs a Fourier transform on the source light by means of physical components. A Fourier transform is a mathematical construct by which information represented in one domain is made to be represented in another. The Fourier transform is presented in a general form in Eq. (20). The function $g(\alpha)$ contains some information of interest in the α domain. The Fourier transform of $g(\alpha)$ is the same information, but in the *x* domain, $f(x)$ [25]. In the case of the Michelson interferometer the information of interest, intensity of light as a function of wavenumber, is transformed by the Michelson interferometer from the wavenumber domain to the spatial domain: intensity of light as a function of OPD. A mathematical application of the Fourier transform to the detector signal as a function of OPD recovers the spectrum.

$$f(x) = \int_{-\infty}^{\infty} g(\alpha) e^{i\alpha x} d\alpha \tag{20}$$

To illustrate this concept, imagine the IR source in Figure 17 is limited to a single wavenumber (i.e. monochromatic light, like a laser), and the wavenumber happens to be 3000 cm^{-1}. This equates to a wavelength of 3.33 μm. At ZPD the intensity of the beam incident on the detector is equal to that emitted by the source. As the mirror moves the intensity incident on the detector begins to decrease until the first OPD to cause perfect destructive interference is reached, and the intensity of light incident on the detector is zero. According to Eq. (17) the first point of perfect destructive interference is at an OPD of 1.67 μm, which corresponds to a mirror displacement of 0.83 μm (see Eq. (16)). As the OPD continues to increase, another point of perfect constructive interference is reached at an OPD of 3.33 μm, or mirror displacement of 1.67 μm, as indicated by Eq. (18). The plot of light intensity incident on the detector as a function of mirror displacement (or OPD, but mirror displacement Δ will be used throughout this text) is called the *interferogram*. In this case, the interferogram is a cosine function with period 1.67 μm, as shown in Figure 18. Note that the sampling rate in this graph is consistent with the sampling rate typically employed with FTIR measurements. This corresponds to the half-period of the fringe pattern (i.e. interferogram) for a HeNe laser with λ = 632.8 nm, which is used in most FTIR to track and control the moving mirror's position.

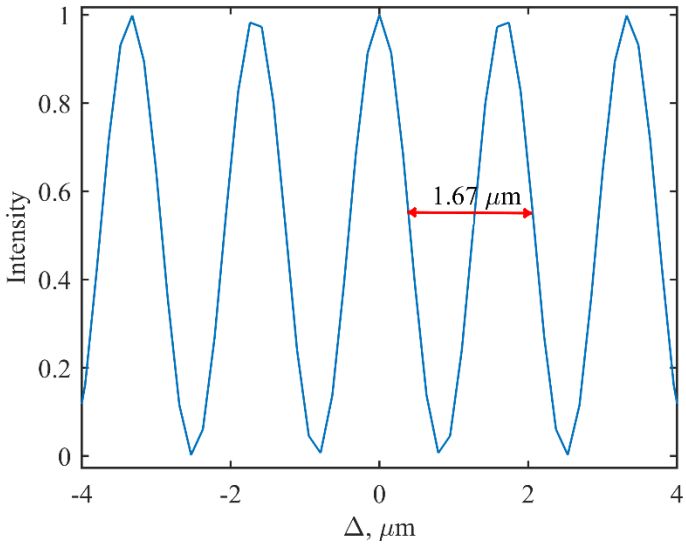

Figure 18. Close-up of the interferogram for a monochromatic light source with $\tilde{\nu}$ = 3000 cm^{-1}, λ = 3.33 μm. It is a cosine function with period 1.67 μm. The sampling rate in this plot is consistent with the sampling rate typically employed in FTIR measurements.

The Fourier transform of the interferogram in Figure 18 is a single feature at $\tilde{\nu}$ = 3000 cm^{-1}. This is the *spectrum* for the monochromatic light source that was passed through the FTIR.

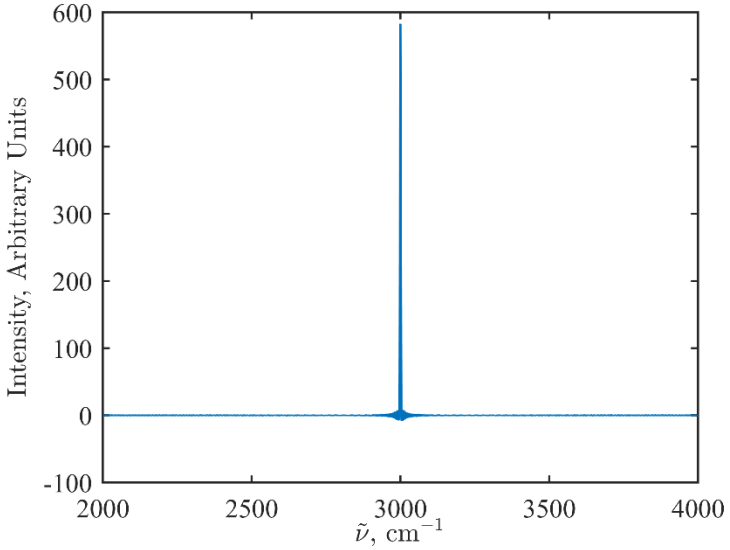

Figure 19. Spectrum associated with the interferogram in Figure 18.

Now imagine a light source with two discrete wavenumber components. One is

3000 cm^{-1}, as before, but the other is 1000 cm^{-1} and is only half the intensity of the first. The interferogram for this source beam is shown in Figure 20. A trained eye could probably look at this interferogram and determine that it is made by a source with two wavenumbers of light, one at 1000 cm^{-1} and one at 3000 cm^{-1}, and perhaps even that the component at 1000 cm^{-1} is less intense than the component at 3000 cm^{-1}. It is doubtful that anything more could be determined by simply looking at the interferogram. Notice that this function is the linear combination of two cosine functions, so $\Delta = 0$, ZPD, is a maximum. This is true for any theoretically-derived interferogram and even for most real interferograms, unless some phase shift has occurred for reasons that will be discussed fully in Chapter 5, Methodology, Section 3.4. The more wavenumbers that are present in the source, the more prominent the maximum at ZPD becomes, until it is the only remaining maximum in the interferogram. It is called the *centerburst* for this reason.

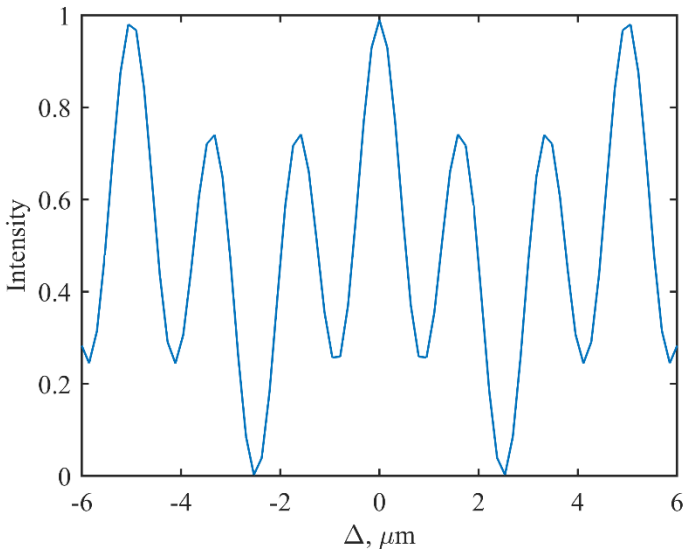

Figure 20. Interferogram produced by a source beam with two wavenumber components, one at 1000 cm^{-1} and one at 3000 cm^{-1}, the former being half the intensity of the latter.

The Fourier transform of the interferogram in Figure 20 is the spectrum shown in Figure 21. From the spectrum it is clear that there are only two wavenumber components, what those components are, and that the contribution from the component at 1000 cm^{-1} is half that from the

component at 3000 cm^{-1}. It is possible to conduct quantitative analysis on spectra by comparing as few as two features, by comparing their relative intensities.

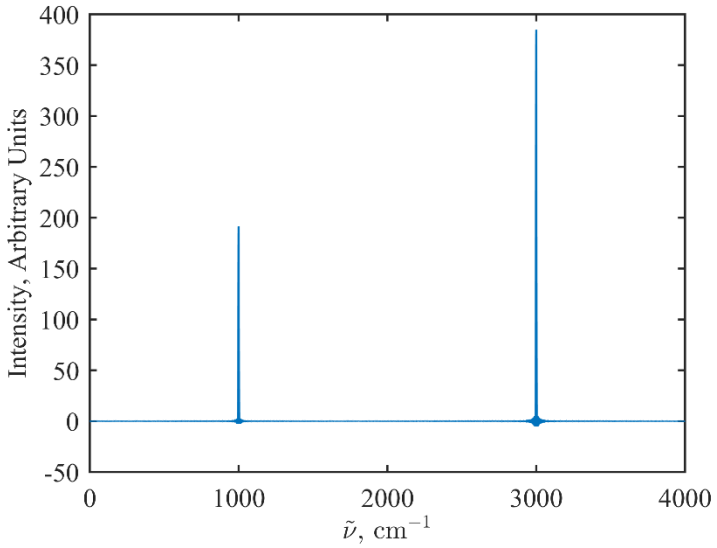

Figure 21. Spectrum associated with the interferogram in Figure 20.

Next imagine a source with the two wavenumber components seen in the previous example, with the same intensities. The difference in this case will be that the continuum of wavenumbers between the two will also be included, with intensity at each wavenumber being determined by linear interpolation. The interferogram is shown in Figure 22. In this case it is clear why the point at ZPD is called the centerburst. When the mirror displacement is extended even farther to each side of ZPD, as in Figure 23, the centerburst becomes even more pronounced. The extremes to the right and left of the centerburst where the signal dampens to almost nothing are called the *wings* of the interferogram. Also note that, unlike the previous cases, it is impossible to determine specific details about the corresponding spectrum by looking at the interferogram. This is where the power of the Fourier transform is made evident.

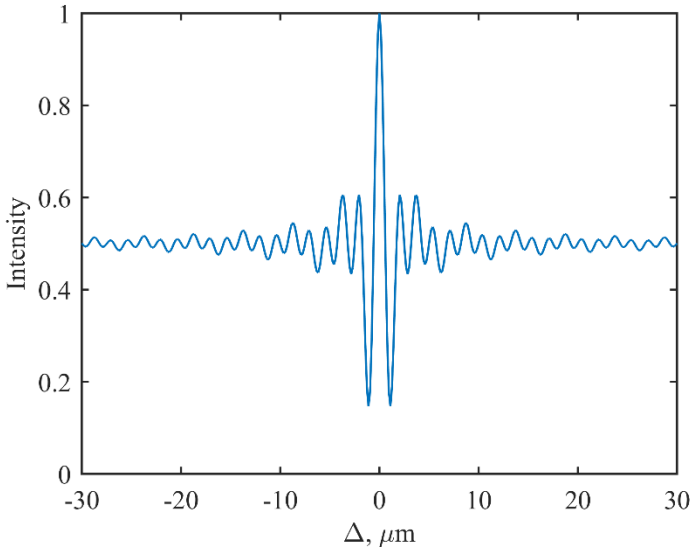

Figure 22. Interferogram produced by a light source composed of a continuum of wavenumbers between 1000 cm^{-1} and 3000 cm^{-1}.

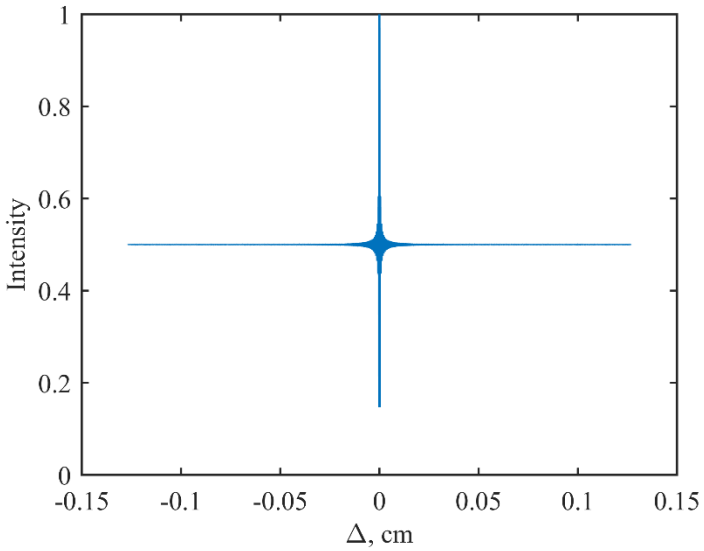

Figure 23. Interferogram produced by the same source as in Figure 22, but with a much greater maximum mirror displacement.

Figure 24 shows the spectrum corresponding to the interferogram in Figure 23. As expected, the intensity at 1000 cm^{-1} is half that at 3000 cm^{-1} and the intensity of light between these two extremes is a linear function of wavenumber.

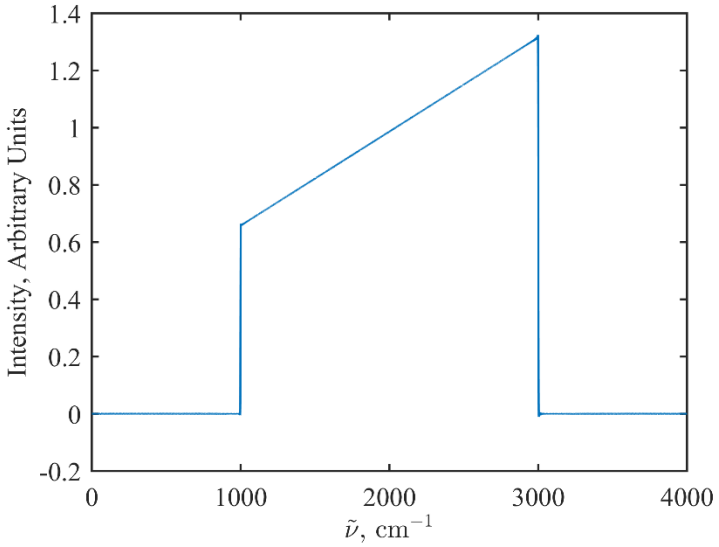

Figure 24. Spectrum associated with the interferogram in Figure 22.

This is an excellent opportunity to discuss the fact that the resolution of the spectrum is determined entirely by the maximum mirror displacement (or maximum OPD) in the corresponding interferogram. The relationship between the two is given by

$$\Delta\tilde{\nu} = (2\Delta_{max})^{-1} \tag{21}$$

where $\Delta\tilde{\nu}$ is the spectral resolution, or smallest discernable difference between two independent features, and Δ_{max} is the maximum mirror displacement. In this case Δ_{max} was approximately 0.125 cm so the resolution of the associated spectrum is 4 cm^{-1}. This means that spectral features closer than 4 cm^{-1} together look like a single feature. The interferogram for this example was generated by adding cosine functions to model individual spectral features that differed from each other by 2 cm^{-1}. The spacing of these features is closer than what can be resolved by the maximum mirror displacement so the spectrum has a single, broad feature. If the maximum mirror displacement captured by the interferogram is extended to 0.25 cm, however, as in Figure 25, the extended interferogram produces a similar spectrum, but with hundreds of individual features spaced 2 cm^{-1} apart and just distinguishable from one another, as shown in Figure 26. Also note that the full spectrum in the top half of this figure captures greater peak intensity than the lower-resolution spectrum in Figure 24.

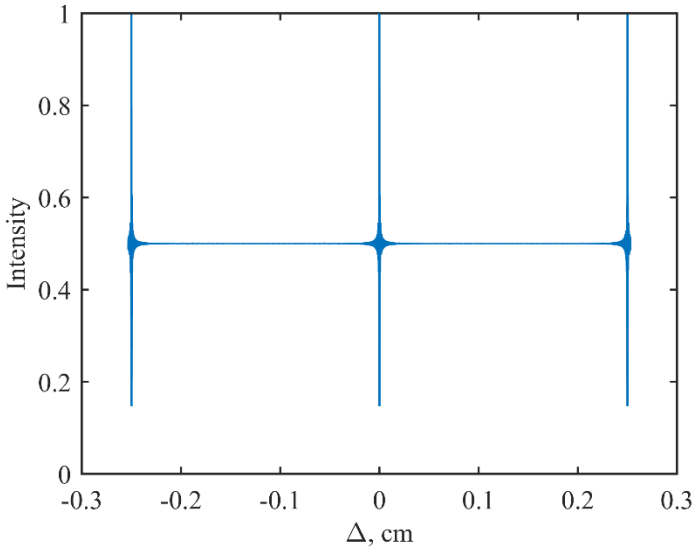

Figure 25. Interferogram produced by the same source as in Figure 22 and Figure 23, but with an even greater maximum mirror displacement, resulting in a spectral resolution of 2 cm^{-1}.

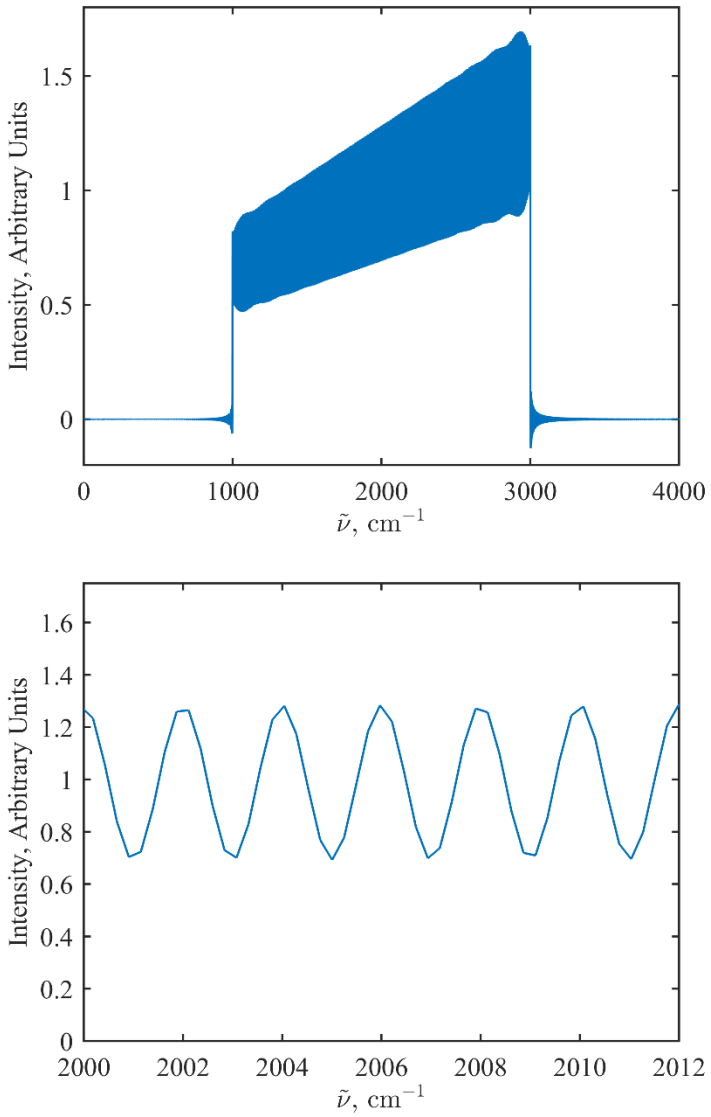

Figure 26. Spectra produced from the interferogram in Figure 25. The full spectrum (top) provides a direct comparison with the lower-resolution spectrum in Figure 24. The partial spectrum (bottom) shows the individual features spaced 2 cm^{-1} apart.

Finally, consider again the light source with a continuum of wavenumber components, as in Figure 24. This time, imagine that the modulated beam exiting the Michelson interferometer passes through an experimental test cell before reaching the detector, where an unknown gas absorbs 50 % of the light in the band 2000 cm^{-1} to 2050 cm^{-1}, but the absorption characteristics are unknown to the experimentalist. The resulting interferogram is shown in Figure 27. The

absorption due to the unknown gas causes no noticeable change to the interferogram from the case with no absorption, which is shown in Figure 22 and Figure 23.

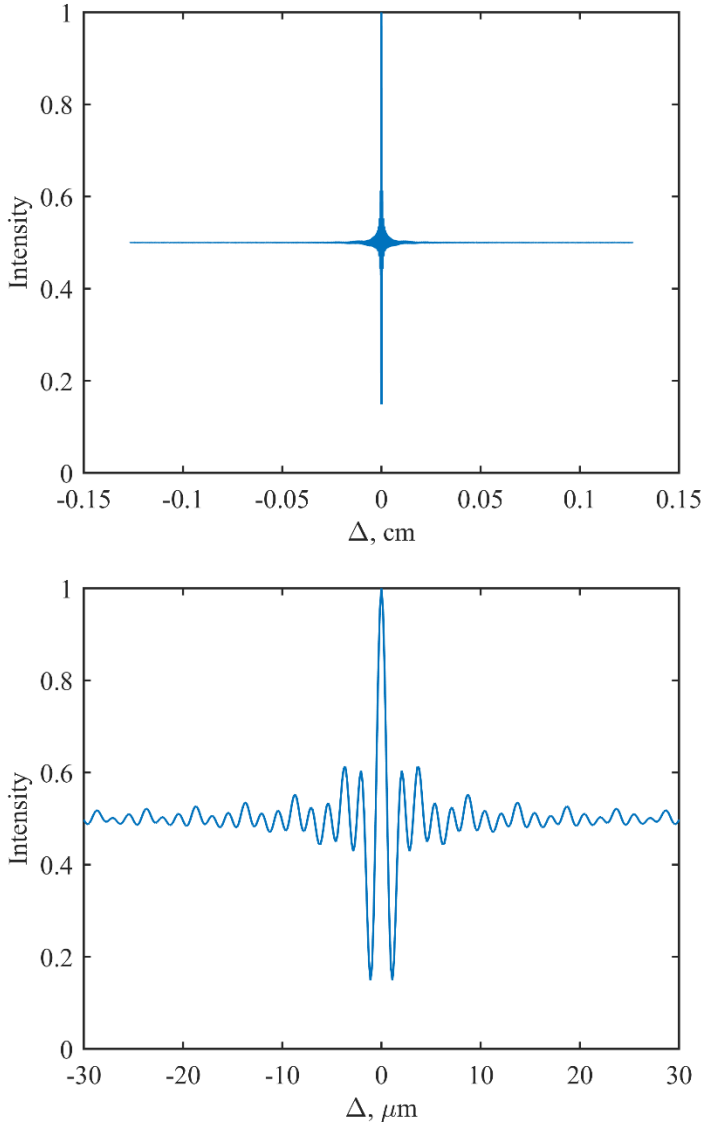

Figure 27. Interferogram produced by the same source as in Figure 22 and Figure 23, but with 50% absorption between 2000 cm^{-1} and 2050 cm^{-1}. The full interferogram (top) has a maximum mirror displacement of 0.125 cm. The centerburst (bottom) is shown for comparison with Figure 22.

The effect of the absorption is made apparent by the Fourier transform, the spectrum shown in Figure 28. The decreased signal intensity between 2000 cm^{-1} and 2050 cm^{-1} is called an absorption feature. The spectrum for the source beam with no absorption, Figure 24, is called the *background spectrum*. Its shape is sometimes called the *instrument line shape* (ILS) because

it characterizes the contribution of the instrument itself, in this case an FTIR, to the spectrum measured with a sample in the test cell. To isolate the effects of the unknown gas, the ILS can be divided out of the spectrum in Figure 28. The spectrum in Figure 28, then, is called the *single-beam spectrum* because it captures the combined effects of both the ILS and the absorbing gas. Another beam (i.e. the background spectrum) is required to isolate the effect of the absorbing gas.

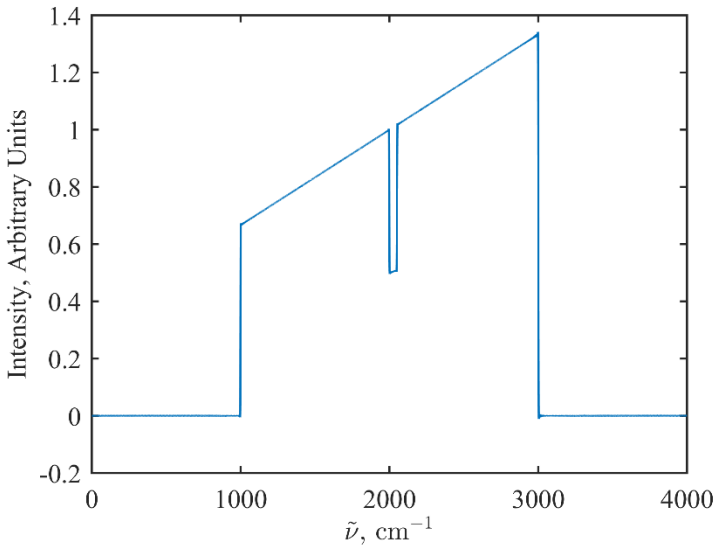

Figure 28. Spectrum associated with the interferogram in Figure 27. An absorption feature is visible near 2000 cm^{-1}.

The ratio of the single-beam spectrum to the background spectrum is called the transmittance, and is typically expressed as

$$T(\tilde{\nu}) = {I(\tilde{\nu})}/{I_o(\tilde{\nu})} \tag{22}$$

where T is transmittance, I is the single-beam spectrum, and I_o is the background spectrum. In the case of this example, transmittance will equal 1 everywhere except where there is division by 0 and in the region where absorption occurs. The transmittance plot for this absorption region is shown in Figure 29. This plot reveals that only 50 % of the light between 2000 cm^{-1} and 2050 cm^{-1} was transmitted through the unknown gas, while 100 % of the light at all other wavenumbers was transmitted, as was specified at the outset of this example.

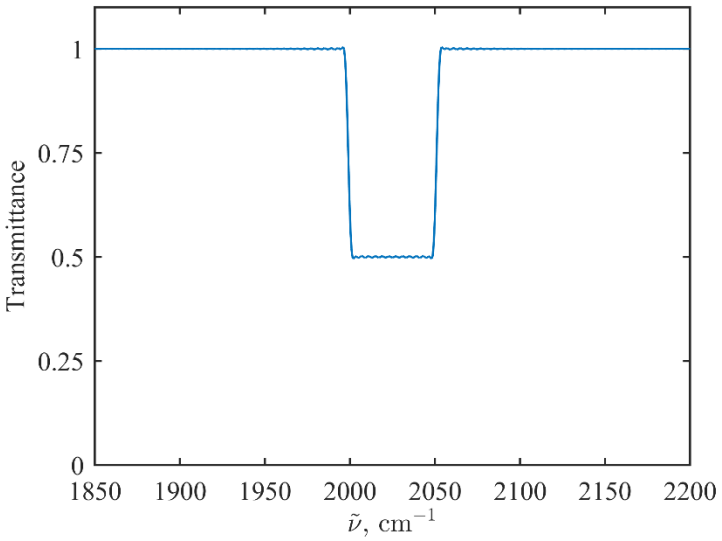

Figure 29. Transmittance for the single-beam spectrum in Figure 28.

Another plot that provides the same information as transmittance is called absorbance. Absorbance is defined as

$$A(\tilde{\nu}) = -\ln\big(T(\tilde{\nu})\big) = -\ln\left(I(\tilde{\nu})\Big/I_o(\tilde{\nu})\right) \tag{23}$$

Absorbance is important because it can be related to absorptivity, $\varepsilon(\tilde{\nu})$, species concentration, *c*, and optical path length, *l*, of each species by the Bouguert-Lambert-Beer Law:

$$A_i(\tilde{\nu}) = \varepsilon_i(\tilde{\nu})\, l\, c_i \tag{24}$$

The absorbance for this example is presented in Figure 30. This absorbance plot is ready for quantitative analysis via spectral fitting, which is described in Chapter 5, Methodology, Section 3.6.

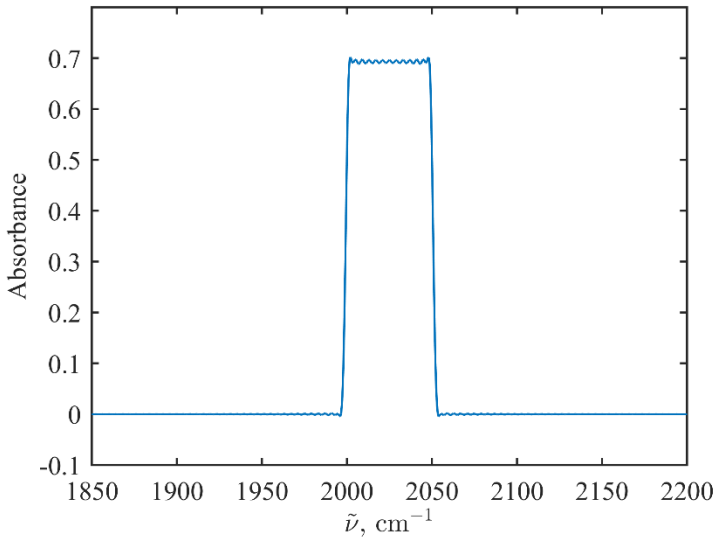

Figure 30. Absorbance for the single-beam spectrum in Figure 28.

5. Examples from the Literature

5.1. Emission Spectroscopy in a Small, Two Stroke SI Engine

Gegg, Kölmel, and Beck [3] modified a small, single-cylinder, two-stroke, SI engine with a displacement volume of 64 cc for optical measurement of the crank-angle-resolved, in-cylinder gas temperature. The figure they provide for their experimental setup is replicated below in Figure 31. They installed a single flush-mount optical probe looking down past the spark plug toward the piston. Emission signal from the engine was filtered using a three-beam interference filter and diffraction grating to isolate the Na and K emission lines at 589 nm and 768 nm, respectively. In-cylinder gas temperature was determined by line-emission method, which is described in detail by Beck, et al. [26]. The temperature is a function of the ratio of the intensity of the two emission lines and known atomic or molecular constants.

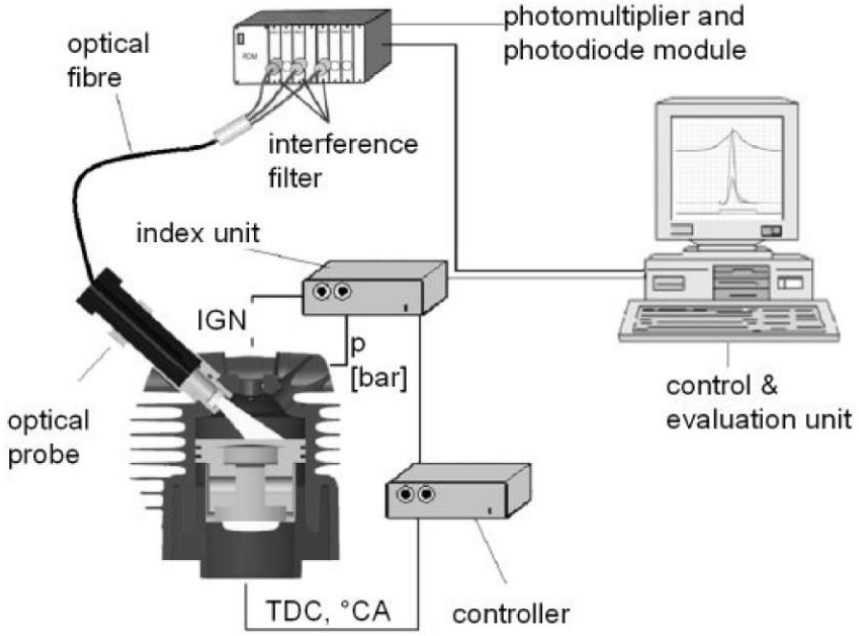

Figure 31. Experimental setup from Gegg, et al. [3]. (2010-32-0062Reprinted with Permission from SAE International)

Gegg, et al. operated their engine at wide-open throttle (WOT), 9000 revolutions per minute (RPM) and measured the temperature between 30° before top dead center (bTDC) and 90° after top dead center (aTDC) with a sampling frequency of 200 kHz. Their temperature profile is replicated in Figure 32 below. They reported an average peak cycle temperature of 2200 K with cycle-to-cycle variation as great as 400 K. The peak temperature was observed between 15° and 20° aTDC each cycle. [3]

Their measurement technique featured sample times fast enough to measure instantaneous temperature profiles, cycle by cycle, a definite strength. Some weaknesses include that emission spectroscopy provides no means to quantify temperature during gas exchange. The data becomes very erratic at temperatures lower than about 1200 K, as can be seen in the data between 40° and 15° bTDC. Finally, the temperature determination relies on only two spectral features. If more spectral features were taken into consideration, the results could be reported with greater confidence.

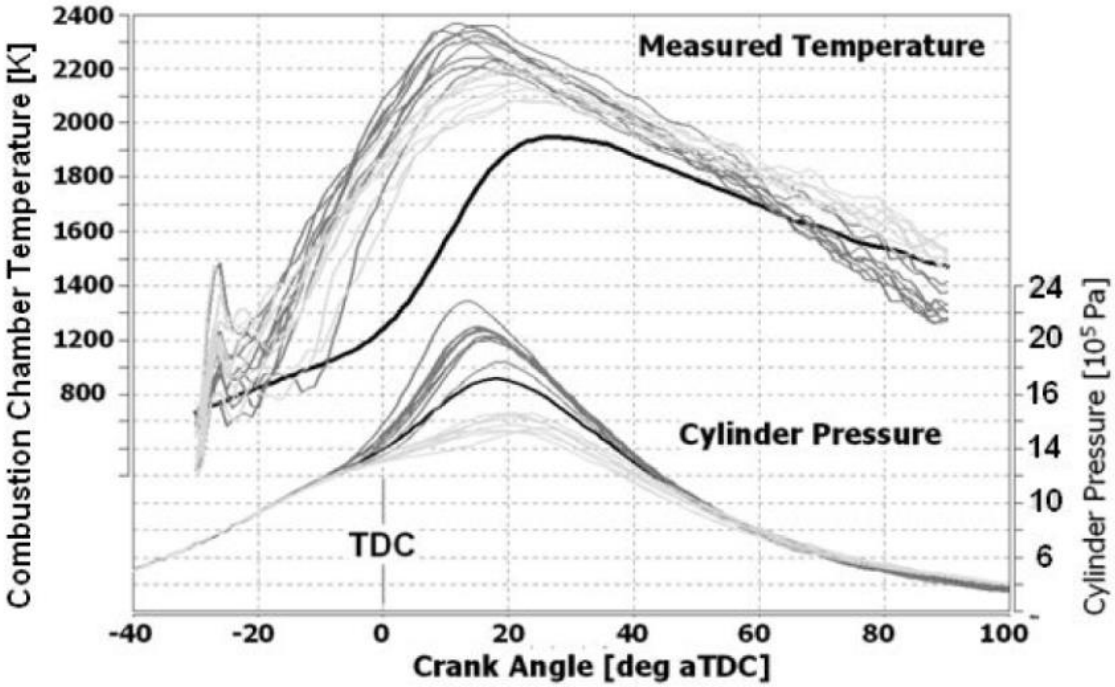

Figure 32. Results from Gegg, et al. [3]. (2010-32-0062Reprinted with Permission from SAE International)

5.2. Absorption Spectroscopy in a Four-Stroke SI Engine

Rein and Sanders [1] used a stock engine with no optical access: a single-cylinder, four-stroke, SI engine with a displacement volume of 190 cc. The setup provided in their article is replicated below in Figure 33. They installed a spark plug with a built-in optical probe. The probe consisted of two parallel fibers, a pitch and a catch, and a stainless mirror mounted 6 mm out into the combustion chamber. The optical probe consequently provided a 12-mm optical path with which to sample the in-cylinder gas. The built-in fibers were sapphire with 420 μm core diameter. The built-in fibers were coupled with 550 μm core diameter sulfide fiber-optic cables. The fibers transported a modulated IR beam from an FT spectrometer to the engine and back to a detector. The integrity of the FT spectroscopy was maintained while sampling this transient process by allowing the engine and the spectrometer to run simultaneously at independent cycle rates until all of the required combinations of crank angle and phase delay (i.e. mirror position for an FTIR spectrometer) were satisfied. With a sampling frequency of 500 kHz, at slow engine operating speeds and fast mirror scanning speeds, large portions of the

crank-angle-resolved interferograms could be collected each engine cycle. Thermal emission signal was filtered out of the interferometer signal using a current amplifier with a built-in high-pass filter.

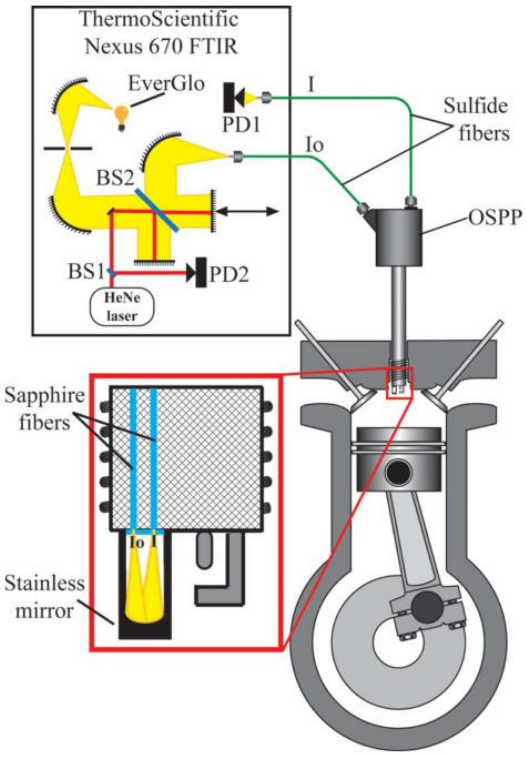

Figure 33. Experimental setup from Rein, et al. [1].

They operated the engine at 1750 RPM, 25% load, and an equivalence ratio of 1.18. Spectra were measured with a resolution of 0.67 cm^{-1} and a range of 2700 to 4200 cm^{-1}. Their temperature profile results are replicated in Figure 34 below. A time-averaged, crank-angle-resolved temperature profile was reported with a peak temperature of approximately 2400 K occurring at approximately 15° aTDC. The gas temperature prior to spark ignition was reported to be approximately 700 K. These results show that the greatest rate of change of species mole fraction for both H_2O and fuel coincide roughly with the greatest rate of increase in the temperature profile. The peak pressure notably comes much later in the cycle.

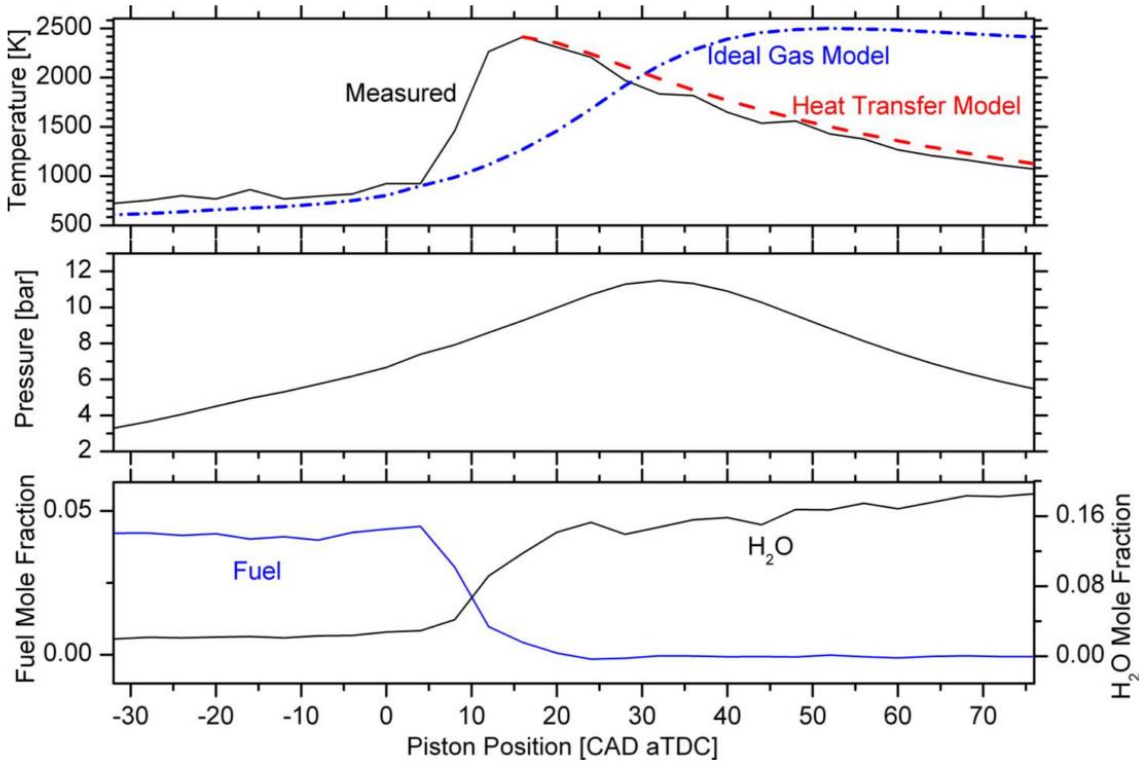

Figure 34. Results from Rein, et al. [1].

The downside of the spark plug optical probe is that the path length sampled may not be representative of the temperature throughout the rest of the cylinder. In fact, the protruding mirror may have caused a turbulent pocket around the probe that resulted in higher heat transfer in the region around the probe.

5.3. Absorption Spectroscopy in an HCCI Engine

Caswell [4] used a single-cylinder test engine with two optical windows on opposite sides. This makes his temperature much more representative of a bulk gas temperature than would be expected from the results in Rein, et al. The figure Caswell provides for his experimental setup is replicated below in Figure 35. He ran the engine in homogeneous-charge compression ignition (HCCI) mode. Water vapor lines from ~ 7300 to 7500 cm^{-1} were measured using a Fourier domain mode locked (FDML) laser. With this setup Caswell was able to determine the crank-angle-resolved temperature with a resolution of 28 data points per crank angle degree and with a RMS error of 5 K at TDC. The temperature prior to combustion was 500 K and the peak temperature was 2000 K. His temperature profile results are replicated

below in Figure 36. Unlike Rein, et al., the peak pressure in Caswell's data coincides almost exactly with peak temperature and maximum H_2O mole fraction. This is most likely due to the differences in combustion processes between the two studies.

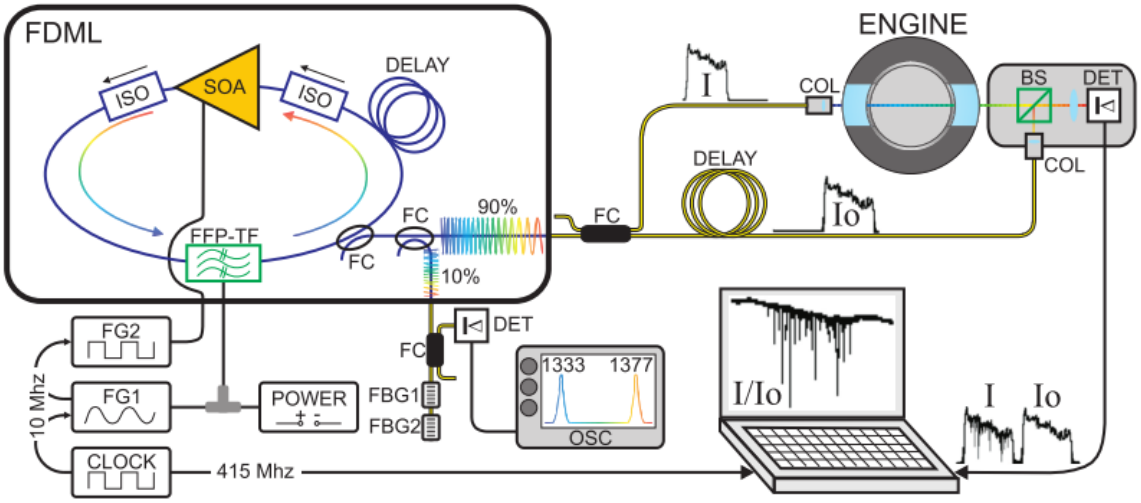

Figure 35. Experimental setup from Caswell [4].

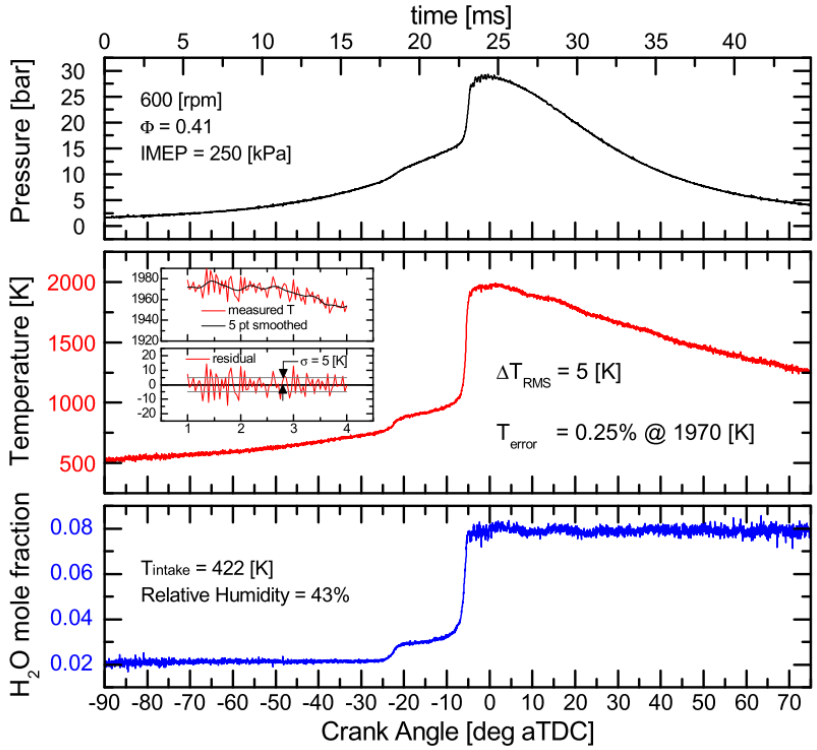

Figure 36. Results from Caswell [4].

III. Methodology

This chapter discusses the hardware developed and the engine employed in order to quantify the objectives of this research. The primary objective of this research was to measure the crank-angle-resolved, in-cylinder, bulk gas temperature of a small ICE in the least invasive way possible. To accomplish this objective FTIR spectroscopy was selected because it can provide data with extremely high temporal resolution and can be non-invasive. FTIR is discussed in detail including the choice of focusing on the mid-IR spectroscopic band. The process of collecting FTIR interferograms is discussed including how to reduce these to processed species and temperatures. Strengths and weaknesses of this experimental method are outlined and what can be learned from these measurements. Implementation of this system into a Modellmotoren 55 cc engine is explained including obtaining optical access and system calibration. The experimental test parameters are outlined and the test matrix discussed.

1. Optical Diagnostics Design Choices

It was clear that some form of optical diagnostics would be required to get non-invasive temperature measurements, but several possible techniques had to be considered. The measurement was required to include the full engine cycle, resolve the crank-angle-dependent temperature to within four crank angle degrees, and handle the rapidly-changing gas state within the optical path. The optical access had to facilitate a cylinder-averaged (i.e. "bulk") gas temperature measurement without impacting engine performance. A series of design choices narrowed down the options until ultimately FTIR absorption spectroscopy with a "pitch-catch" optical setup was selected. The following subsections walk through each of these design choices.

1.1. Emission or Absorption

One of the first choices to be made when considering optical diagnostics is whether to collect absorption or emission spectra. Absorption spectroscopy requires that an external radiation source be directed through sample, then collected again and analyzed. Emission spectroscopy analyzes the radiation emitted by the sample itself. For engine diagnostics, this

choice implies whether the setup requires one optical probe or two. Absorption spectroscopy is used for quantitative analysis with much greater success due to the applicability of Beer's Law (Eq. (24)) in many situations and the fact that absorption is a function of T while emission is a function of T^4. The equation for emission is

$$E_i(\tilde{v}) = \varepsilon_i(\tilde{v})\sigma T^4 \tag{25}$$

where E is the emissive power as a function of wavenumber, ε is in this case the emissivity, not the absorptivity as in Beer's Law, σ is the Stefan-Boltzmann constant, and T is the temperature. One can see that at if temperature is what you are trying to measure and it happens to be a very small value, the result will be very sensitive to small errors in the emissive power measurement. Emission spectroscopy is limited not only by its quantitative value, but also by the fact that the subject of research must actively emit. It can, however, be a powerful technique when emission is strong and consistent, and the temperature is high. Absorption spectroscopy was chosen for this effort due to the quantitative power of absorption data and the inconsistency of emission in an ICE.

1.2. Measurement Techniques

Many techniques can be employed for engine optical diagnostics. The decision of which technique to use comes down to the signal strength, the bandwidth, and the sample rate required. Tunable lasers provide strong signal and fast sample rates, but limited bandwidth. Multiplexed grating spectrometers can provide fast sample rates and excellent bandwidth, but may be limited by signal. An FTIR has similar strengths and weaknesses as a grating spectrometer, but benefits from two distinct advantages. There is a throughput advantage because the full beam intensity is measured by a single detector whereas grating spectrometers pass only a small band of light to each detector. There is also a multiplexing advantage (replicated by most grating spectrometers with a detector array) because every wavenumber is measured simultaneously. These advantages are also called the Jacquinot advantage and the Felgett advantage, respectively [23]. The ability of an FTIR to measure a broad, continuous spectrum simultaneously made it an attractive choice for this measurement. FTIR spectroscopy was chosen for its unique ability to

provide tremendous amounts of data in a short period of time [7]. This benefit of FTIR meant that temperature measurements could be verified by many features throughout the spectrum instead of relying on just one or two discrete absorption lines.

1.3. Optical Probe Selection

Absorption spectroscopy requires two points of optical access to the ICE: one for the source beam to enter and one for it to exit. Rein et al. used a commercially-available probe that was built into a spark plug [1]. Proves of this kind have two fiber ports on the external side, collimating lenses within, and a mirror that protrudes a few millimeters into the engine (see Figure 37). The entrance and exit fibers are side by side so the light enters the cylinder, reflects off the mirror, and then exits. This setup provides a short path length, which can be desirable to avoid excessive absorption of a line of interest. The fact that a mirror protrudes into the cylinder, however, makes this method invasive. The protrusion may cause localized turbulence, increase heat transfer, and in this way skew the temperature results, as was postulated by Rein, et al. Whether or not this is true, this setup undoubtedly fails to capture any temperature gradients across the combustion dome because the optical path is limited to such a small portion of the space.

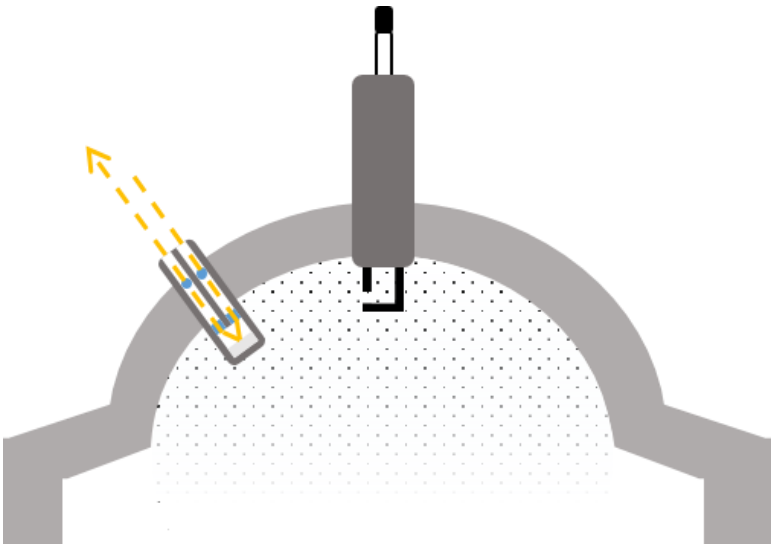

Figure 37. Common optical probe design with a mirror protruding into the cylinder.

A “pitch – catch” concept was adopted for the optical access early in the planning phase. This concept consists of optical ports on opposite sides, so the source beam is passed across the full expanse of the combustion chamber (see Figure 38). Such a setup can be implemented with flush-mount optical probes, so hot spots are less of an issue. Plus, the results can be interpreted as a bulk representation of the in-cylinder gas because the spectra are the spatially-averaged result of absorption across the entire beam path. Such a concept does not, however, lend itself to commercially available components so flush-mount optical probes were designed and built in-house. The details of the specific probe design for this research are provided in Section 2.3.

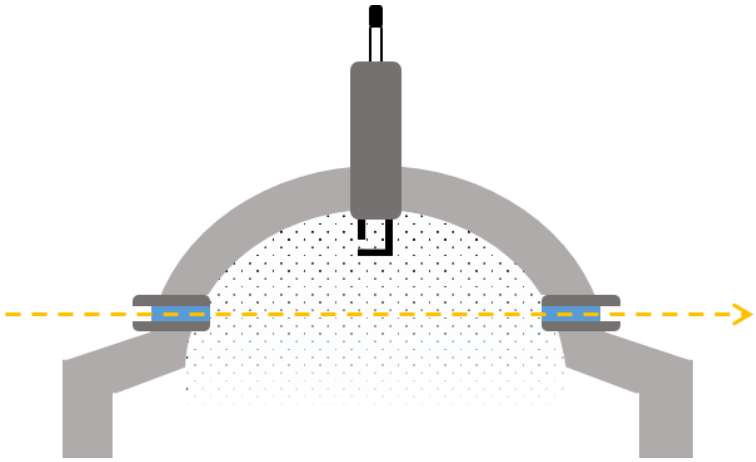

Figure 38. Flush-mount optical probe design with pitch and catch probes on opposite sides of the cylinder.

1.4. Managing a Dynamic Sample

A key challenge was that FTIR spectroscopy requires a finite amount of time to collect a single measurement. In the case of this experiment, for example, at 6000 RPM 16 engine cycles were captured by each scan of the mirror. The nature of an FTIR scan is that the information at every wavenumber depends on the data collected at every mirror position, so a sample must be in steady state to get meaningful results. This potential issue can be resolved either by using a step scan measurement technique (measure many engine cycles at each mirror position before moving on to the next) or by allowing both the engine and the FTIR to run continuously at independent speeds and collecting scans until many samples have been collected at each combination of mirror position and crank angle. This technique randomly samples the engine cycle for every

mirror position over a long period of time, as opposed to marching through mirror positions chronologically, which can introduce time-dependent biases to the resulting interferograms. Either way, FTIR measurements require long data collection periods and rely on the assumption that cycle-to-cycle variation is negligible. The latter technique was chosen for this research, and the particulars of its execution are provided in Section 2.4 and Section 2.

1.5. Choosing Absorption Lines

There are many strong absorbers in-cylinder throughout the engine cycle (e.g., H_2O, CO_2, CO, and CH_4) but the quantity of each species fluctuates. The mid-IR, particularly from 2000 cm^{-1} to 4000 cm^{-1}, provides features for H_2O, CO_2, and CH_4. This can be shown with a simple simulation, as is possible with the internet-based application SpectraPlot.com. SpectraPlot, in turn, creates its figures using the HITRAN spectral database [27]. Figure 39 shows the input fields used to generate a simulated spectrum that approximates the conditions in the 3W-55i during combustion, and the spectrum itself. There is a strong, isolated CO_2 feature between 2200 cm^{-1} and 2400 cm^{-1}, and a weak, overlapping one between 3400 cm^{-1} and 3800 cm^{-1}. There are isolated H_2O features above 3800 cm^{-1}, and isolated CH_4 features around 3000 cm^{-1}. The isolated features for H_2O and CO_2 are prime candidates for quantitative analysis via Beer's Law. The absorption due to CH_4 is in reality confounded by absorption of larger hydrocarbon chains, but hydrocarbons can be analyzed qualitatively as a group.

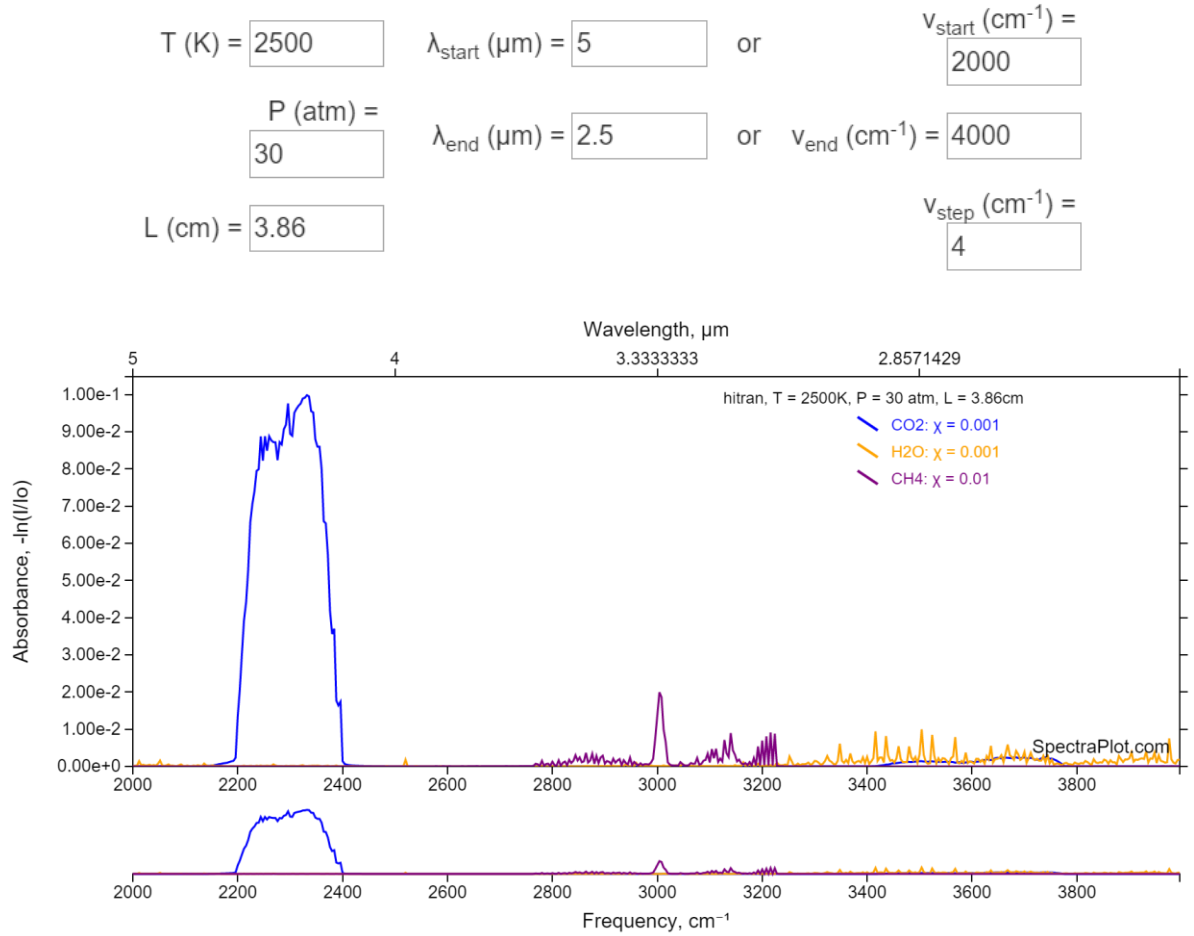

Figure 39. The inputs and resulting simulated multi-species spectrum produced by SpectraPlot.com.

1.6. Summary of Spectroscopy Design Choices

In summary, the FTIR absorption spectroscopy with a pitch-catch optical probe system was chosen to measure the temperature of the in-cylinder gas because it is a noninvasive measurement technique. Also, FTIR can provide data across a broad spectrum in a relatively short amount of time. This measurement technique does not benefit from the signal to noise possible using laser diagnostics, and it depends on the assumption that there is negligible cycle-to-cycle variation in engine gas dynamics. Despite these weaknesses, FTIR absorption spectroscopy was determined to be the best choice for this measurement.

The nature of FTIR spectroscopy is such that the information provided by each mirror position has an impact on every value in the spectrum. It therefore takes a finite amount of time to collect a spectrum: the amount of time it takes for the mirror to traverse from one extreme of

its path to the other. If the sample changes during the course of the mirror's traverse, the entire spectrum is affected, and sometimes rendered useless. This problem can be managed by tracking the mirror position and engine cycle position associated with each data point collected, then sorting by crank angle. This method relies on the assumption that the cycle-to-cycle variation of in-cylinder gas dynamics and combustion processes is negligible with respect to the strength of the signal. The following sections provide the details of how to collect all the data needed for the sorting process, how to sort the data, and how to determine the temperature of the gas based on crank-angle-resolved spectra.

2. Experimental Setup

This research was completed in parallel with other activities to support the research objectives. As a consequence, the optical components used for this specific effort was grafted into the heavily instrumented research bench where the engine was run. The experiment required custom engine modifications to provide optical access. The FTIR was appropriately configured to handle the unique challenges presented by this research. A data acquisition system was developed to meet the demands of this data-heavy research. The following subsections go into detail about each of these vectors of effort with an emphasis on the setup of physical hardware.

2.1. Small Engine Research Bench

The Small Engines Research Lab (SERL), part of the Air Force Research Labs (AFRL) propulsion branch, built the Small Engine Research Bench (SERB) to quantify the energy losses associated with small ICE. The literature documents the incremental development of the SERB over the past several years [5, 16, 17, 19, 28]. Figure 40 depicts the primary attributes of the SERB as it was set up for this research. For clarity, the optical setup is discussed separately, in Section 2.4.

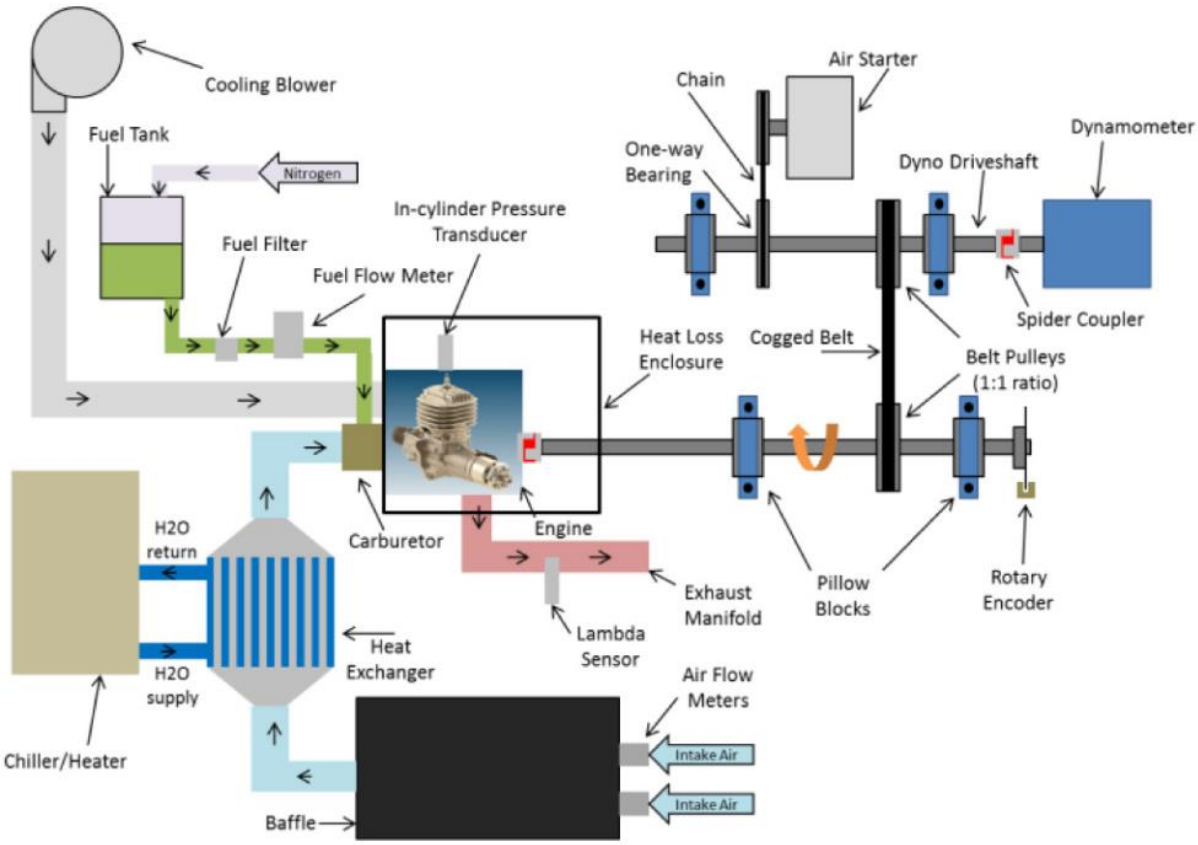

Figure 40. Experimental setup of the SERB.

The following description of the components of the SERB is an abbreviated excerpt from Horn [28]:

> "The engine was mounted on a steel plate and connected to a drive shaft. A dynamometer and air starter were attached to a parallel drive shaft. The two shafts were coupled with a cogged belt. The dynamometer and engine were coupled to the drive shaft assembly via Ruland jaw couplers with 98 Shore A hardness spiders. The air starter was a GAST 2A-NCW-7B pneumatic motor and was connected to the drive shaft with a one-way bearing to reduce parasitic friction losses. The dynamometer was a Magtrol 1 WB 65 series eddy current model. Its torque and speed capacity were 10 N-m and 10,000 rpm respectively. Torque and speed measurements were accurate to ±0.5% of full scale. A US Digital E6 optical encoder was used to track shaft rotation with 1800 counts per revolution. In-cylinder pressure measurements were taken using a Kistler type 6113B pressure measuring spark plug capable of detecting pressure from 0-200 bar with an accuracy of ±1% Voltage signals from the pressure transducer were amplified with a Kistler 2852 Signal Conditioning Platform. Pressure data and crank angle position were collected using an AVL Indismart combustion analyzer."

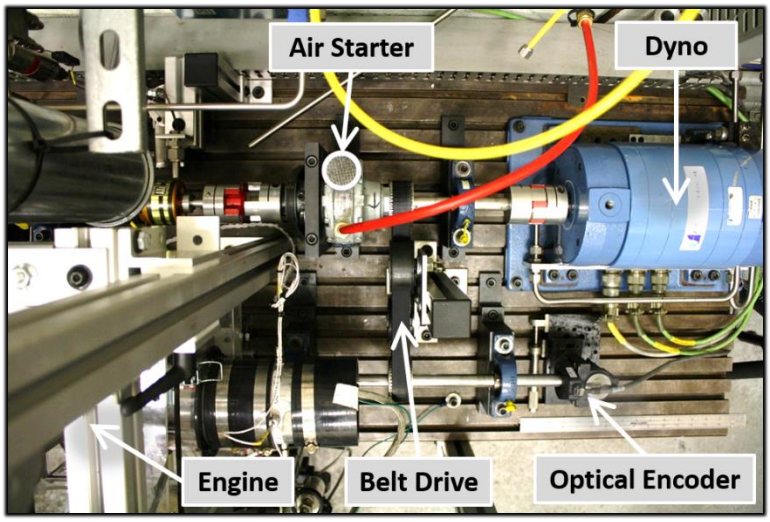

Figure 41. The primary components of the drivetrain assembly on the SERB.

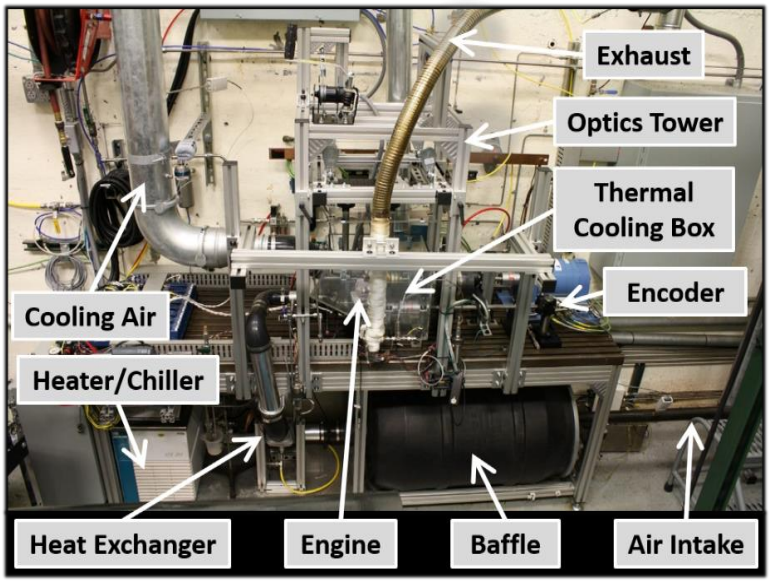

Figure 42. The SERB fitted with the optics tower.

A full description of the test bench setup is given by Horn [28]. The current setup differed from Horn in that the FTIR was set up to pass a beam through the engine cylinder instead of the exhaust manifold, as is described in detail in Section 2.4.

2.2. Thermal Cooling Box

One feature of the SERB was a transparent acrylic glass box built around the engine. The purpose of the box was to isolate the cooling flow forced across the engine from the surrounding air and direct it through an outlet where temperature and mass flow rate were measured and

compared to the same measurements upstream of the engine. This setup provided a spatially and temporally averaged thermal loss measurement during engine operation.

The thermal cooling box used for previous research efforts was too small to accommodate the optical components required for the current research effort. A larger box was built for this purpose. Figure 43 shows the two boxes side-by-side. On the new box, the nearest ducting coupler (the large black cylindrical part) had to be slanted up at a 30° angle to clear the throttle body and engine air intake manifold. Service ports were added to the new box on both sides of the engine (seen covered with square plates mounted with a screw at each corner). These allowed access to the box for quick adjustments without removing the lid. The new box was designed to have the same footprint as the old box at the points of contact with the SERB. Figure 44 shows the box disassembled for installation around the engine. Weather strips were applied to all of the seams between adjoining parts to prevent the cooling air flow in the box from leaving the system through any path besides the downstream duct.

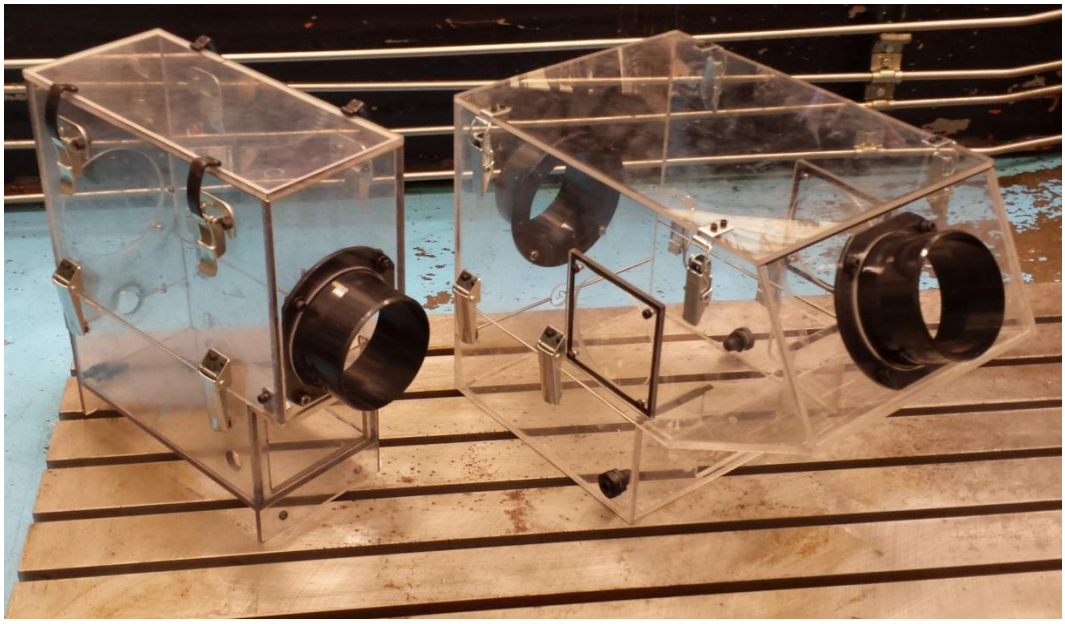

Figure 43. The old (left) and new (right) thermal cooling boxes side-by-side.

Figure 44. The new thermal cooling box disassembled for installation around the engine.

2.3. Engine Head Modification

The head of the engine was modified to take optical measurements inside the combustion chamber. Sapphire windows were installed to allow the optical access, as shown in Figure 45. Threaded ports were machined through opposite sides of the head immediately above the TDC position of the piston and low enough to clear the electrodes on the spark plug. The ports were threaded to receive 16 mm-long M3 bolts. The bolts were bored and used as threaded casings for sapphire windows. Sapphire rods 12.7 mm long and 1.6 mm in diameter were glued in the holes in the bolts. The sapphire and bolt assembly is henceforth called the optical probe. The probes were installed in the ports with copper washers used to set the penetration depth and provide air-tight seals. The probes were designed to be flush with the combustion chamber wall to minimize the impact of the engine modification on compression and gas dynamics during combustion. This design allowed for fast installation and removal of the optical probes and easy access to the optical surfaces that required frequent cleaning.

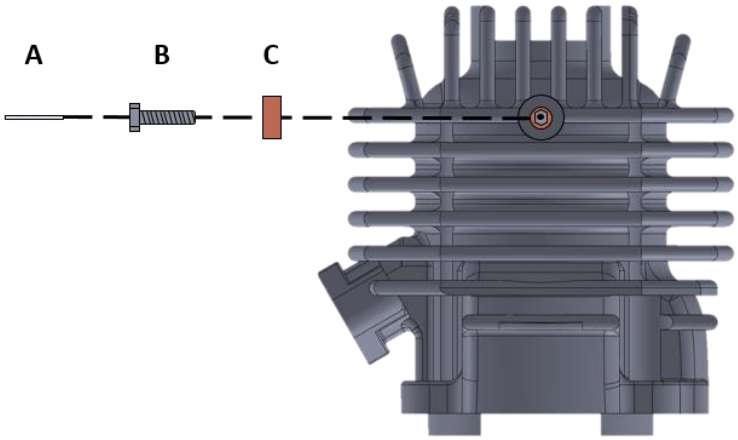

Figure 45. Exploded engine modification assembly. A) Sapphire rod; B) M3 bolt; C) Copper washer.

2.3.1. Port Location

Measurements of the head and manufacturer drawings were used to determine the true dimensions of the head within 0.1 mm. Figure 46 shows the cross-section of the cylinder wall at the combustion chamber with all of the dimensions required to proceed with the modification except the protrusion depth of the spark plug electrodes, which was 2.8 mm below the mouth of the combustion dome. The threaded ports were machined just above the squish region of the cylinder, as shown in Figure 47. Notice that the diameters of the ports were limited by the thickness of the cylinder wall, especially above the squish region. This consequently limited the diameter of sapphire rods, which was a limiting factor for signal throughput. Signal to noise was a constant challenge during data acquisition.

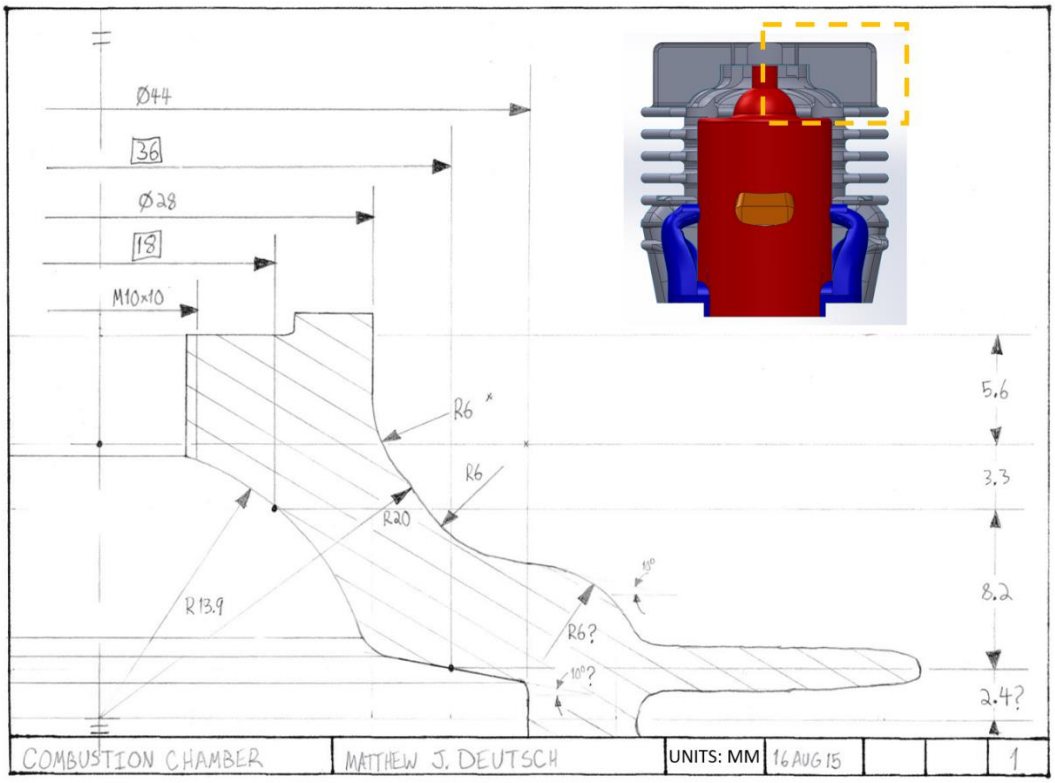

Figure 46. Cross-section of the cylinder wall at the combustion chamber. Dimensions are derived from manufacturer drawings and verified with measurements where possible.

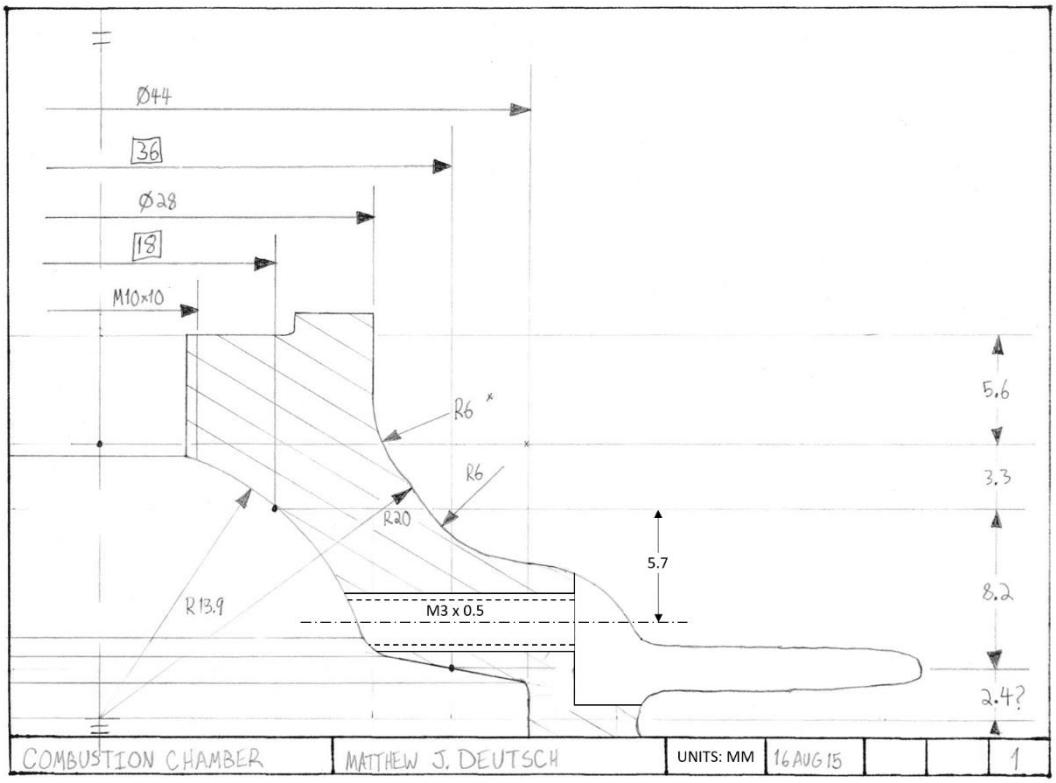

Figure 47. Drawing of a threaded port.

2.3.2. Sapphire Window Design

Sapphire was chosen for the window material because of its hardness, coefficient of thermal expansion, and transmissivity in the radiation band of interest, 4000 cm^{-1} to 2000 cm^{-1} (2.5 μm to 5 μm). Thirty optical-grade sapphire rods measuring 12.7 mm in length and 1.6 mm in diameter were purchased from Swiss Jewel Company. The size of the windows was limited by the size of the engine, as discussed in Section 2.3.1. The design was also influenced by a desire for windows that could be removed and cleaned easily. Several concepts were considered during the early development of the design. Details about the concepts that were ultimately rejected are included in Appendix A.

The windows chosen for these experiments had to be hard. Exposure to the combustion chamber, frequent handling and installation, and periodic cleaning made these windows susceptible to soot buildup and scratching. Sapphire has a hardness of 9 on the Mohs' Hardness Scale. This simplified handling the windows. The windows could be cleaned by bathing in methanol solution and scrubbing with the tip of a toothpick.

Sapphire has coefficients of thermal expansion of 6.66 x 10^{-6} m / (m K) parallel to optical axis and 5 x 10^{-6} m / (m K) perpendicular to optical axis. This compares to that of steel, 12.0 x 10^{-6} m / (m K), and that of aluminum, 22.2 x 10^{-6} m / (m K). Because the assembly consisted of sapphire rods inside of steel bolts inside of an aluminum engine head, it was not possible for one material to crush another during thermal expansion, assuming uniform temperature distribution across the three materials.

Sapphire has a transmissivity of better than 0.8 in the visible spectrum and extending down into the near infrared, as low as about 2000 cm^{-1}. This complemented the other optical components, which set the system spectral range from 4000 cm^{-1} to 2000 cm^{-1}.

2.3.3. Bolt Modification

The early concept for the bolt modification was simply a hole slightly larger than 1.6 mm in diameter, just large enough to slide in a sapphire rod coated with glue, through the entire length of the bolt. It was assumed that the rods could be glued inside the bolts with an

appropriate adhesive and in this way permanently secured. This design proved to be problematic because it was difficult to ensure the glue coated the surfaces of both the sapphire and the steel properly during assembly. Later bolts were designed to have a slightly reduced hole diameter toward the exterior of the engine, as shown in Figure 48. This reduced diameter prevented a sapphire rod from being ejected during engine operation, should the glue fail. This added safety measure came at the cost of reduced signal due to the smaller aperture size upstream of the sapphire rod, but proved to be a necessary precaution.

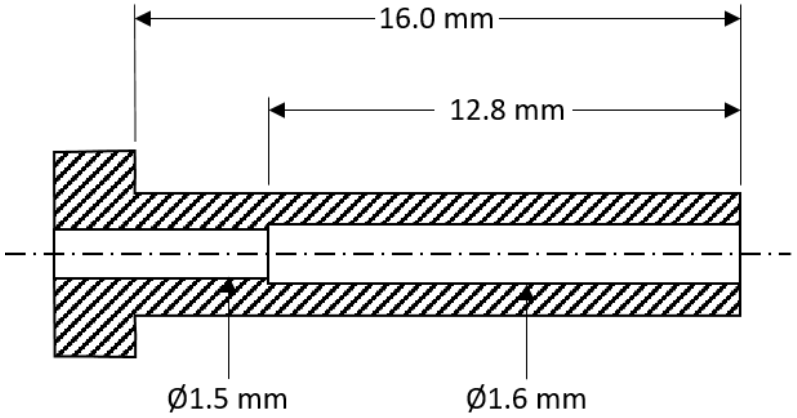

Figure 48. Bolt modification with reduced inner diameter on the outside to prevent the sapphire rod from being forced out.

2.3.4. Optical Probe Assembly

A sapphire rod was glued inside each modified bolt to complete the optical probes. Early probes used Resbond 904, a high-temperature zirconia adhesive rated for shear stresses of up to 3000 psi and temperatures up to 4000 °F. It proved difficult to ensure this glue completely filled the gap between the sapphire rod and the surrounding wall of the bolt, leaving affected probes prone to failure or leaking. Later probes used a standard two-part epoxy with less frequent issues.

Recognizing that technique was important when applying the glue, the assembly process was perfected through iterative trial and error. With the ceramic glue it was possible to submerge the entire bolt and sapphire into a glue bath and slide the two parts back and forth to work glue into the gaps. The threads of the bolt and the optical surfaces of the sapphire were

coated with wax prior to the glue bath, as shown in Figure 49 and Figure 50. Next the assembly was heated at 200 °F for four hours. The heat treatment melted away the wax coating and hardened the glue. Excess glue was removed with razor blades and pins, and the optical surfaces were polished with toothpicks. The glue bath was not possible with the two-part epoxy because it set so quickly and could only be mixed in small batches. Instead, the mixed epoxy was applied liberally to the sapphire rod, then worked into the gap between the rod and the bolt as before. Most of the excess epoxy could be cleaned away immediately with a paper towel. After the epoxy had set, any remaining epoxy was removed with pins, then the optical surfaces were polished as described previously.

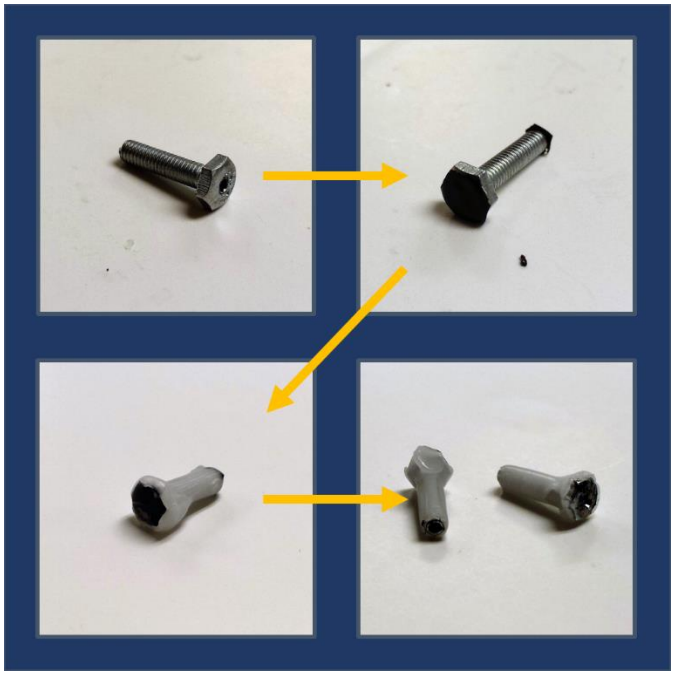

Figure 49. Steps for builing optical probes. Top Left: modified bolt; Top Right: holes covered with electrical tape; Lower Left: after dipping in wax; Lower Right: after removal of tape.

Figure 50. Preparing a sapphire rod for a glue bath by coating optical surfaces with wax.

2.4. Optical Setup

The FTIR was coupled to the ICE as depicted in Figure 51. A modulated beam was routed from the FTIR to the SERB and back with optical fiber so the two could be physically separated by a thick concrete wall. The wall prevented data acquisition issues due to vibrations and spark noise but posed a challenge due to signal losses in the fibers. Off-axis parabolic mirrors were used to focus or collimate the beam at each fiber terminal, as appropriate. The following subsections describe the optical setup in detail.

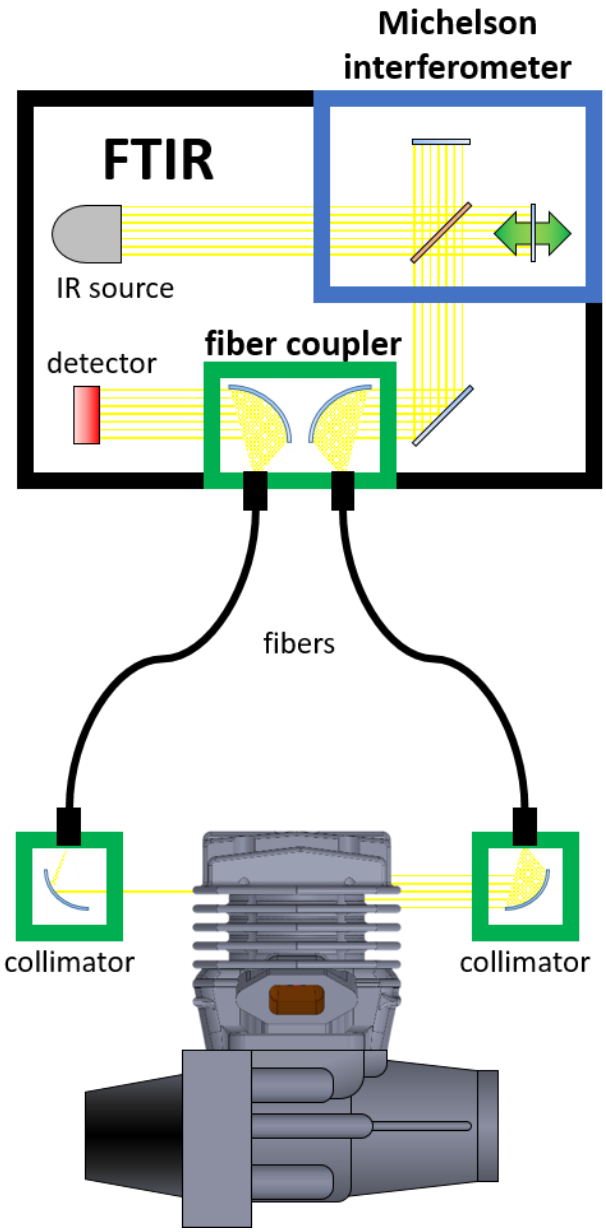

Figure 51. Optical setup for data collection in the modified engine

2.4.1. FTIR Setup

The FTIR chosen for this effort was the Thermo Scientific™ Nicolet™ iS™-50R research spectrometer. This instrument had a spectral range of 7,800 cm^{-1} to 350 cm^{-1}. The instrument was capable of spectral resolutions as small as 0.09 cm^{-1}. It was equipped with a coated KBr beamsplitter in the interferometer to allow operation in the mid-wavelength infrared (mid−IR) spectral range: 5,000 cm^{-1} to 2,000 cm^{-1} (2 µm to 5 µm). A HeNe laser signal was

used to track and control the position of the moving mirror in the interferometer. The instrument was also equipped with a mercury cadmium telluride (MCT) detector with external AC and DC analog signal outputs. The body of the FTIR spectrometer was desiccated and purged by dry nitrogen.

Figure 52 highlights the primary components in the rear compartment of the FTIR: the source and the Michelson interferometer. There is an air-tight lid over the top of this compartment to hold a nitrogen gas purge in the instrument during operation, but it was removed to show the components underneath. There was one more compartment behind what is shown in this figure, which houses the HeNe laser. The laser beam was directed to the Michelson interferometer from the far side and then captured by its own detector. The resulting interference fringe was used to track the position of the moving mirror. Figure 53 shows the full FTIR from the side (the rear compartment is in the right half of the image).

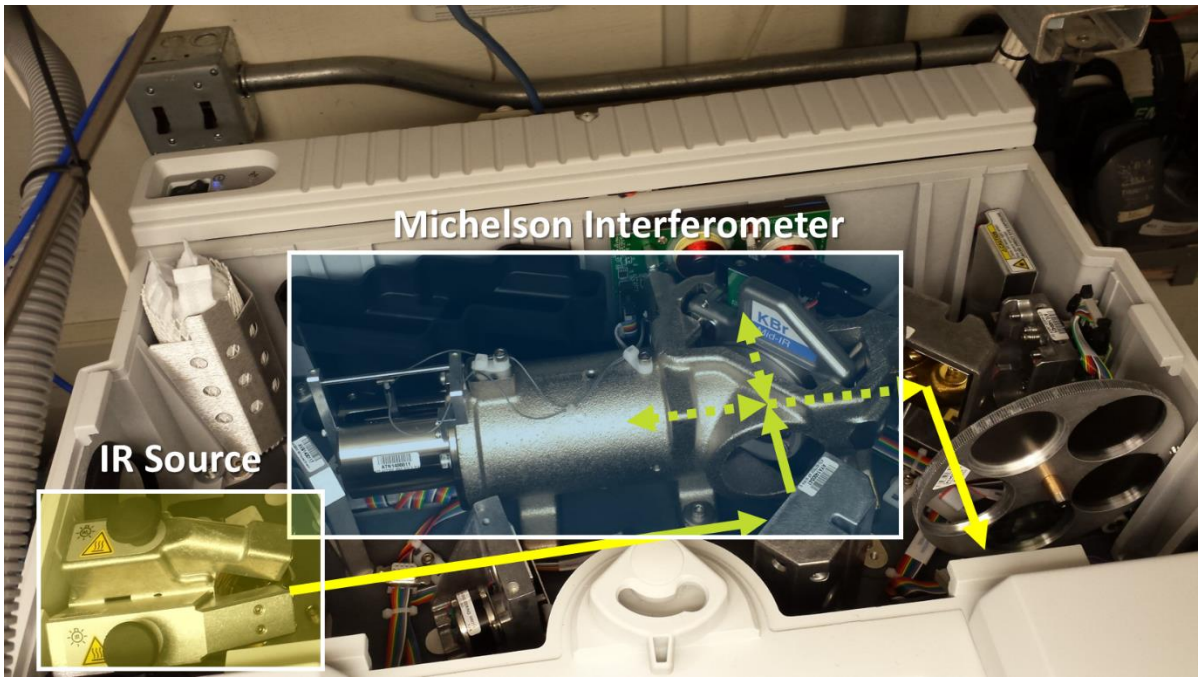

Figure 52. The rear compartment of the Thermo Scientific™ Nicolet™ iS™-50R research spectrometer. The IR beam path is indicated by yellow arrows.

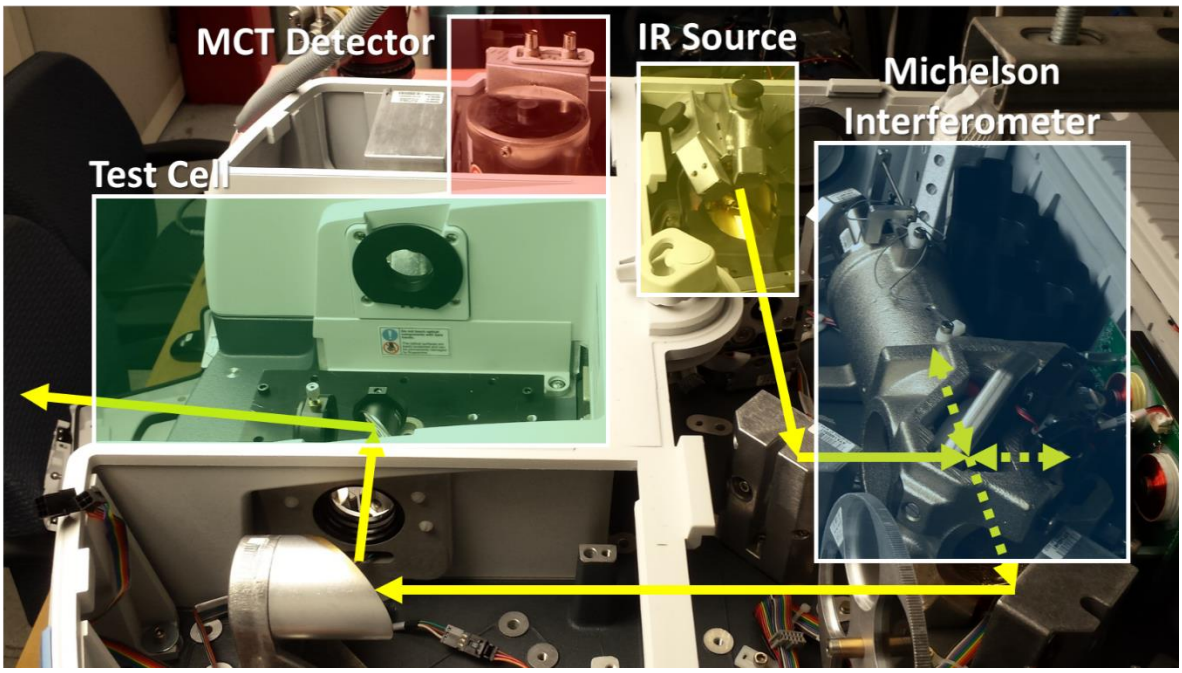

Figure 53. The Thermo Scientific™ Nicolet™ iS™-50R research spectrometer. The IR beam path is indicated by yellow arrows. An optical fiber (not shown) routes the IR beam to the Small Engine Research Bench (SERB) and through the engine.

The internal MCT detector can be seen on the far side of the test cell in Figure 53. This detector was used in early tests, but eventually abandoned for an external MCT detector that was DC-coupled and provided greater control over filtering and amplification of the signal. This new (Figure 54) detector was the InfraRed™ Associates, Inc. MCT-5-0.5PV.

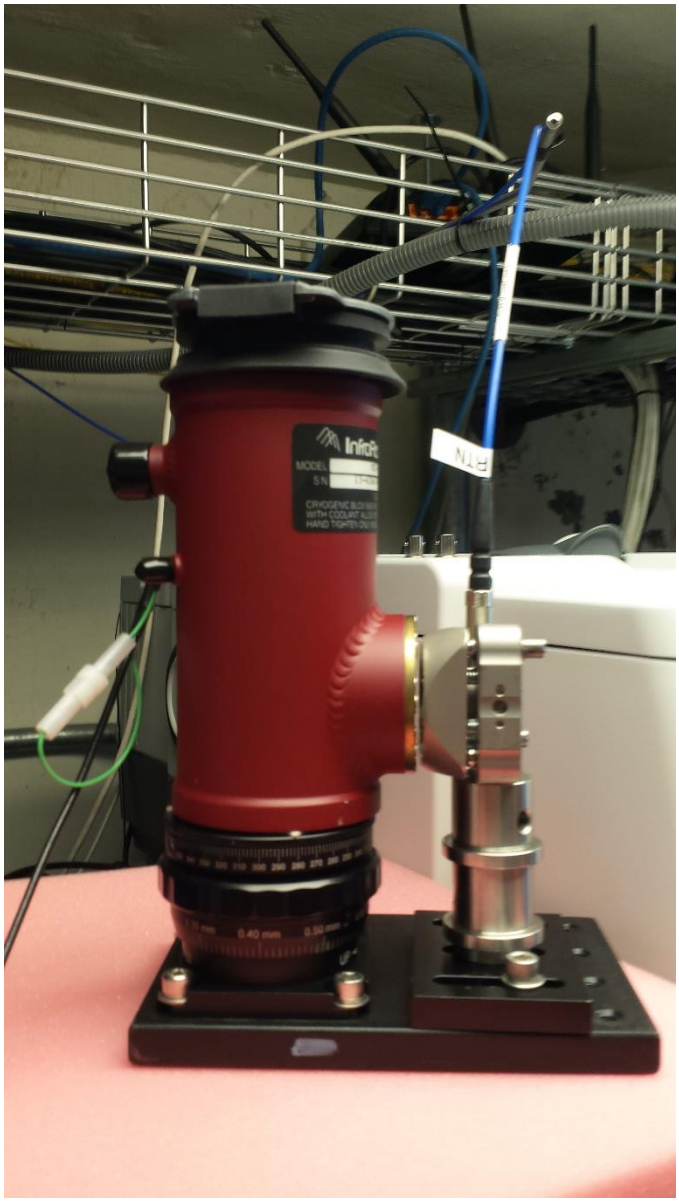

Figure 54. The InfraRed™ Associates, Inc. MCT-5-0.5PV detector.

The FTIR was designed to examine samples in a test cell internal to the device. For this application, the FTIR was separated from the sample by a concrete wall. Fiber cables were used to route the modulated beam from the test cell to the SERB and back. Off-axis parabolic mirrors were used to focus the beam in the FTIR test cell on to the fiber terminal. This was first attempted with an all-in-one fiber coupling device called the Harrick FiberMate2™. When the signal-to-noise ratio of the data was found to be insufficient during early testing every optical component was considered for possible ways to improve signal to the engine. It was determined

that free-standing components could provide a better signal than could the FiberMate2™, so later testing used individually-procured off-axis parabolic mirrors and fiber terminals connected to translation stages and kinematic mounts. Figure 55 shows the final optical components in the test cell of the FTIR. With more degrees of freedom than the fiber coupler, the new setup provided improved control over alignment and spot size on the fiber terminals. The parabolic mirrors were shaped to be 90° off the axis of symmetry and reflect up to a 1" diameter collimated beam.

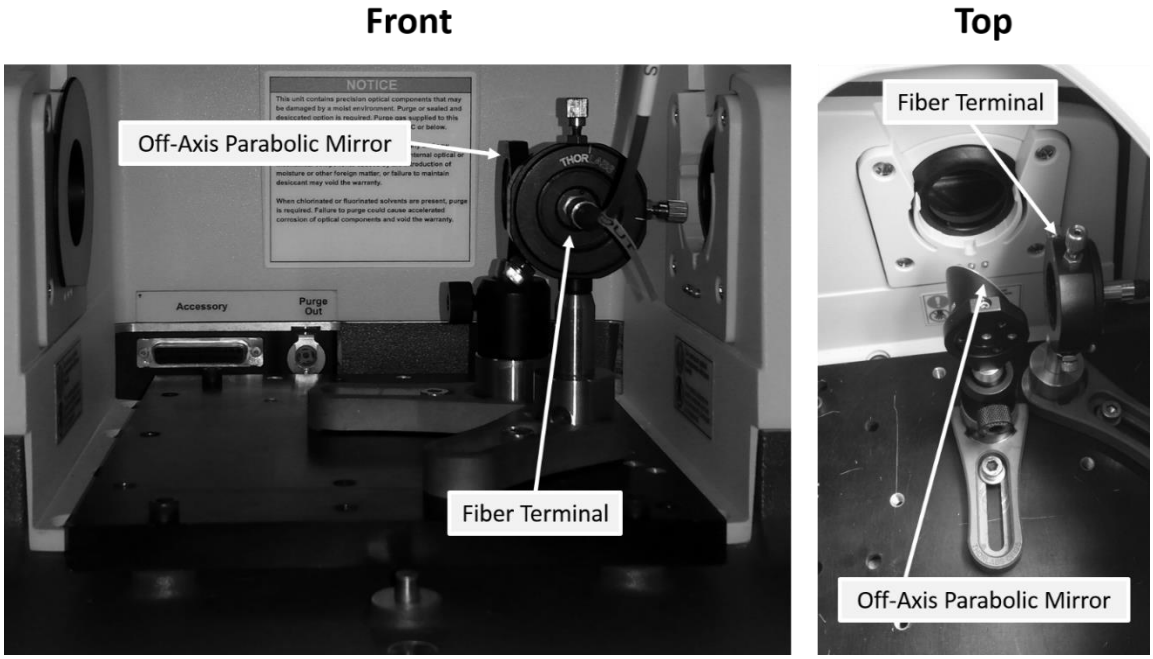

Figure 55. The optical components in the test cell of the Thermo Scientific™ Nicolet™ iS™-50R research spectrometer. The IR beam is focused to a point on the fiber terminal for transport to the Small Engine Research Bench (SERB).

The collective transmissivity of the various components allowed a spectral range of 4,000 cm^{-1} to 1800 cm^{-1}, or 2.5 µm to 5.6 µm. The maximum displacement of the scanning mirror was 0.132 cm, so the maximum OPD was 0.264 cm and the resolution of each scan was ~ 4 cm^{-1}. The data acquisition device (DAQ) used for this effort collected data continuously at 200 kHz. The FTIR scanned continuously with a mirror speed of 1.898 cm/s and used a HeNe laser to track mirror position. This resulted in a distance of 0.190 nm between samples, or approximately three samples per HeNe fringe.

Some of the problems with early data were thought to be caused by signal processing performed on the interferogram by the FTIR prior to output. The detector actively adjusted the baseline of the interferogram to remain at zero. The periodic spikes in signal caused by emission in the engine resulted in a reactionary response from the detector that was potentially degrading or drowning out data. This problem was solved by routing the beam to another MCT detector independent of the FTIR. The signal beam was focused to a spot on the new detector instead of returned to the FTIR.

Figure 56 compares an interferogram collected with the old, built-in detector, to one collected with the new, external detector. A critical difference lies in the intensity of the centerburst for each case. Each centerburst is circled in red for clarity. Centerbursts with the old setup were less than 0.3 V from peak-to-peak, while they were greater than 2.5 V with the new setup. This gave the new data far-superior bit resolution when passed to an analog-to-digital converter. The significance of this improved bit resolution is made evident when looking at similar interferograms after digitization and application of a digital bandpass filter, as shown in Figure 57. The important metric for comparison in these interferograms is the ratio of centerburst intensity to emission signal intensity. It is clear to see that the emission signal is filtered out much more effectively in the new setup when compared to the old setup.

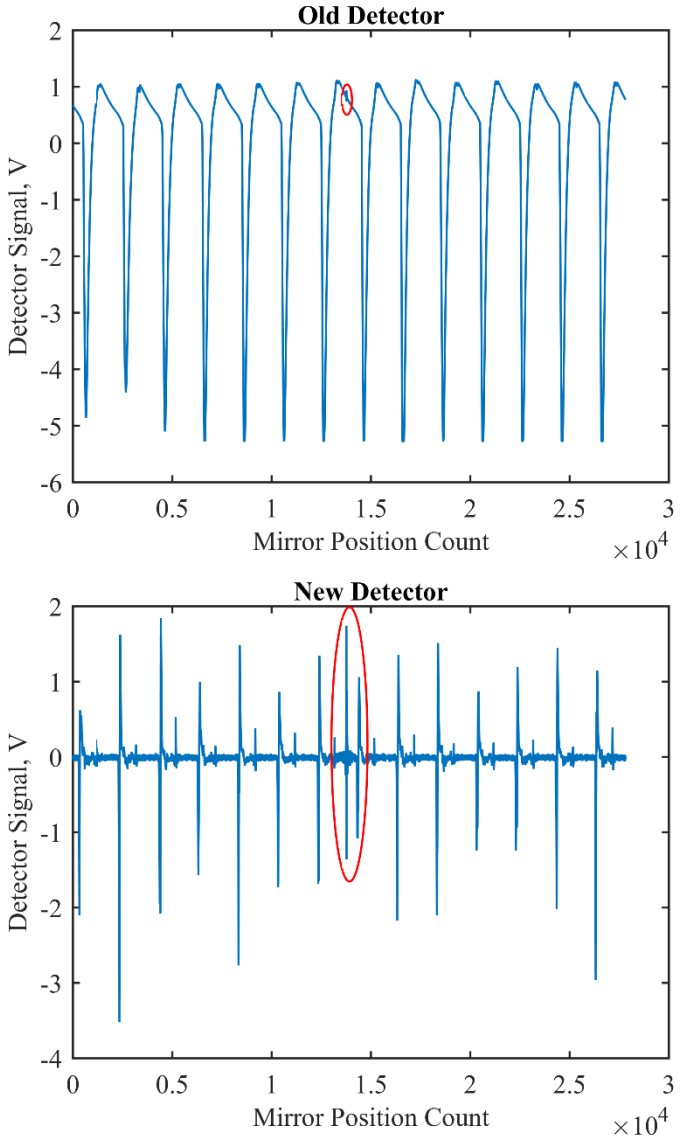

Figure 56. Sample raw interferograms from the old and new MCT detectors, as labeled. The centerburst in each case is circled in red.

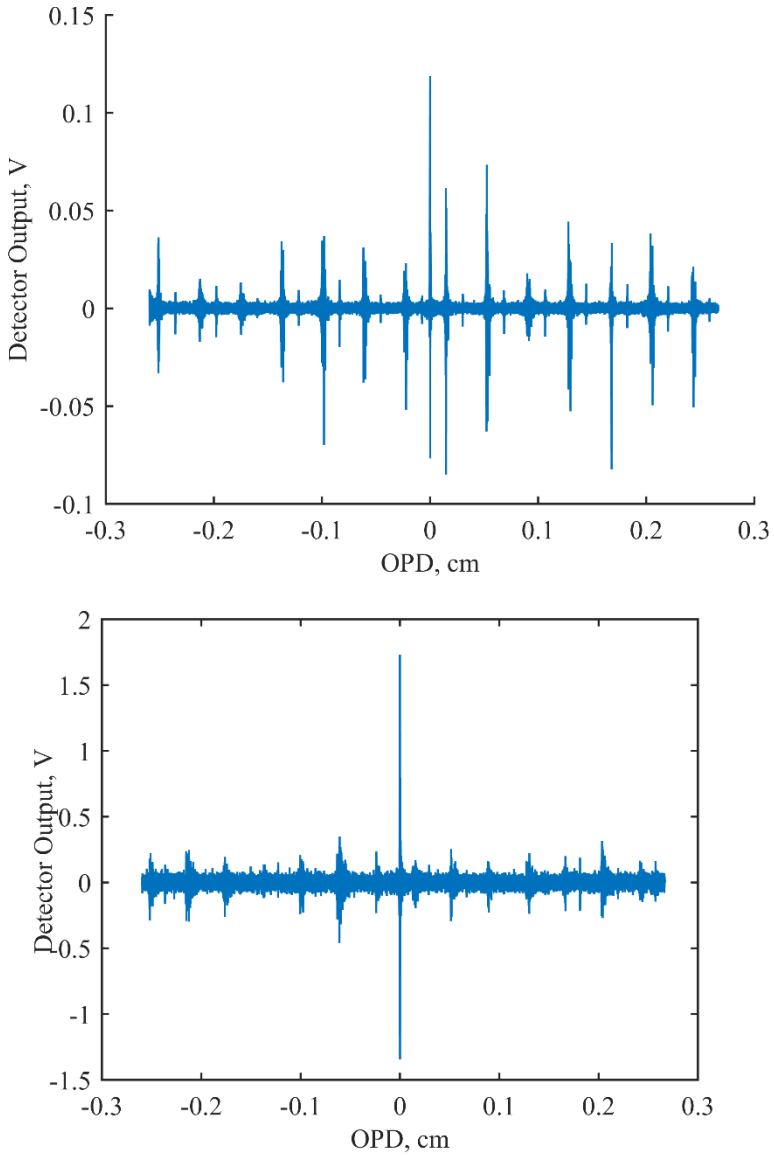

Figure 57. Sample interferograms from the old detector (top) and new detector (bottom) after digitization and application of a bandpass filter.

2.4.2. SERB Setup

The modulated signal beam was routed from the FTIR to the optical engine and back via multimode fibers. The fibers had 100 μm diameter InF^3 cores with a numerical aperture (NA) of 0.26 and were 4 m long each. Once at the engine, collimators were required to collimate the beam, direct it through the modified engine, receive the beam on the opposite side, and focus the beam to a spot on the terminal of the return fiber. Lenses can produce collimated beams less than the 1.5 mm limiting diameter of the optical probes, but the refractive index of any lens

causes some of the wavelengths of interest to be less collimated than others at any given time. Off-axis parabolic (OAP) mirrors, on the other hand, collimate and focus beams using reflection instead of refraction and there is consequently no wavelength dependency. For this reason, OAP mirror collimators were selected for this application.

Unfortunately, it was not possible to collimate a beam with a small enough diameter with OAP mirror collimators. The smallest available collimator had an effective focal length (EFL) of 7 mm. The resultant output beam diameter, calculated using Eq. (26), was 3.64 mm. This equated to the loss of approximately 70% of the signal collimated and directed toward the engine.

$$\emptyset = 2 \times NA_{Fiber} \times EFL \tag{26}$$

The optical setup at the SERB required a point source at a fiber terminal to be collimated, directed through a hole that was 16 mm deep and 1.5 mm in diameter, across a 30 mm wide chamber, through an identical hole on the opposite side, then focused to a point at another fiber terminal. Precision alignment of the optical components was critical to the success of the experiment. The solution had to take into account vibration of the test bench, forced airflow across the optical components, the need for frequent access to the engine, and spatial limitations presented by other hardware on the SERB.

In order to minimize the vibration of optical components, the framework for those items was isolated from that of the engine and exhaust. New framework, the optical tower, was anchored directly to the test bench (Figure 58 and Figure 59). A winch and pulley system was built into the tower to raise and lower a carriage with an optical breadboard and all the necessary optics components (Figure 60). The carriage had sliders on all four corners that ran through channels in the vertical posts holding up the tower. L-brackets were mounted on the posts to act as stops for the carriage, to ensure that it was always lowered back to the same position. Locks on all four sliders kept the carriage from shifting in any way during engine operation.

The optics tower's carriage allowed the delicate optical components to be lifted out of the way when adjustments had to be made to the engine or optical probes. When the carriage was lifted and lowered back into place, re-alignment of the optical components only required small adjustments. This setup saved time and provided flexibility when problems had to be addressed in the middle of an experiment.

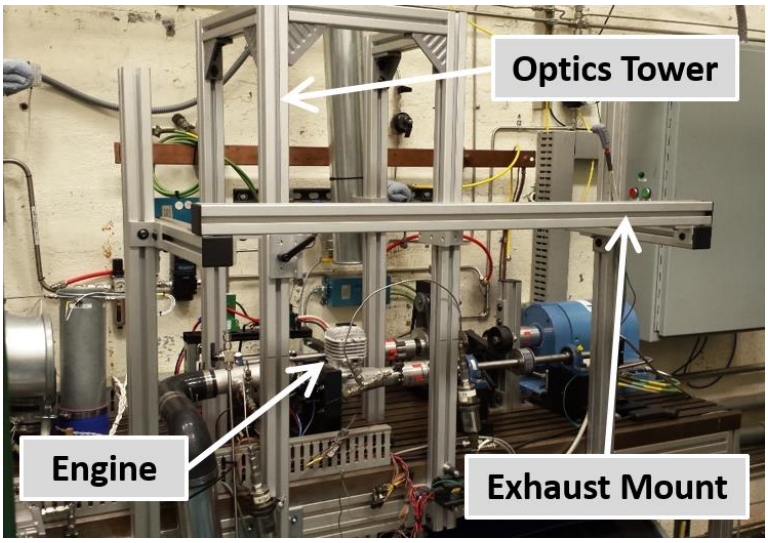

Figure 58. The partially-assembled optics tower. All four posts were bolted directly to the test bench and isolated from any moving or vibrating components.

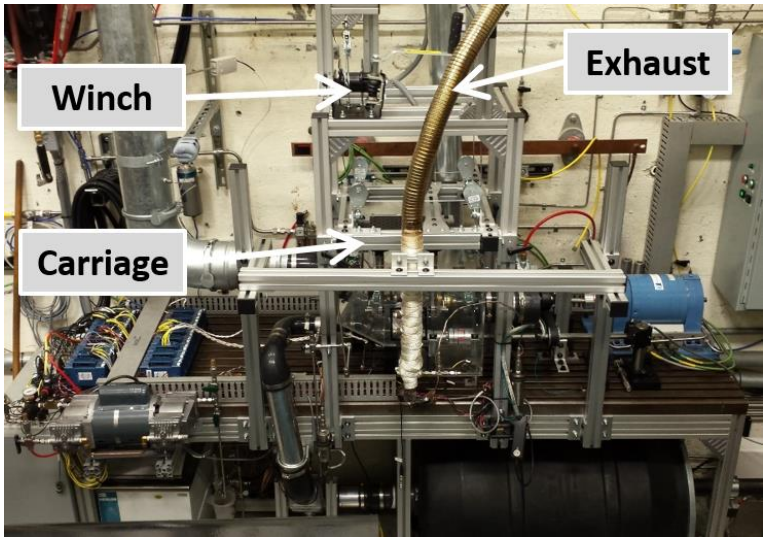

Figure 59. The fully-assembled optics tower. The exhaust line rises up in front of the tower, but is supported by a separate frame.

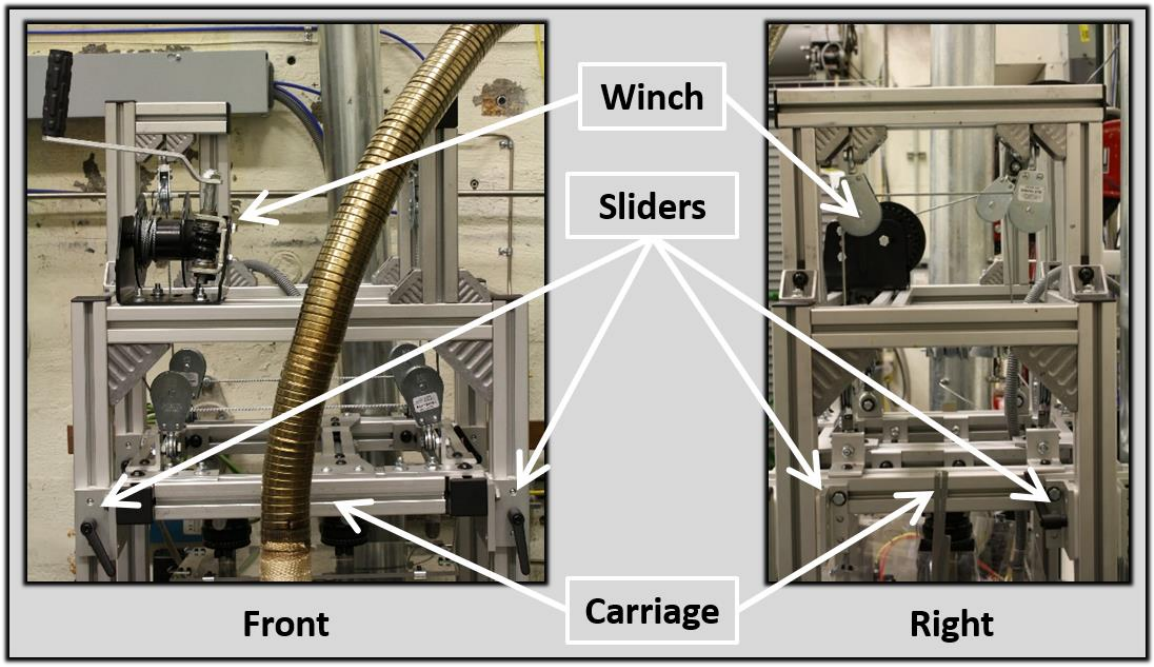

Figure 60. Close-ups of the optics tower featuring the carriage, winch, and pulley system. The sliders with locks can also be seen on the four corners of the carriage.

The optical components were suspended from the optical breadboard, which was attached to the carriage on the optics tower. The collimators needed four degrees of freedom – two translational and two rotational – each with the capability for micrometer precision. The required degrees of freedom were provided by horizontal and vertical translation stages and kinematic mounts, the combination of which are hereafter referred to as the collimator mounts. They are shown in Figure 61 and Figure 62. The long posts, while necessary, were difficult to work with. As the collimators were bumped and pushed around over time the translation stages that the posts were mounted to eventually sustained wear. The stages developed play and in some cases became difficult to adjust. They had to be removed periodically to tighten loose parts. Despite these challenges, the collimator mounts served their purpose. Figure 63 shows the modified engine (top) and the collimators lowered into place and aligned (bottom). The near collimator is removed (but the collimator mount is still in place) to show an alignment laser shining through the optical probes, far collimator, and 4 m of fiber.

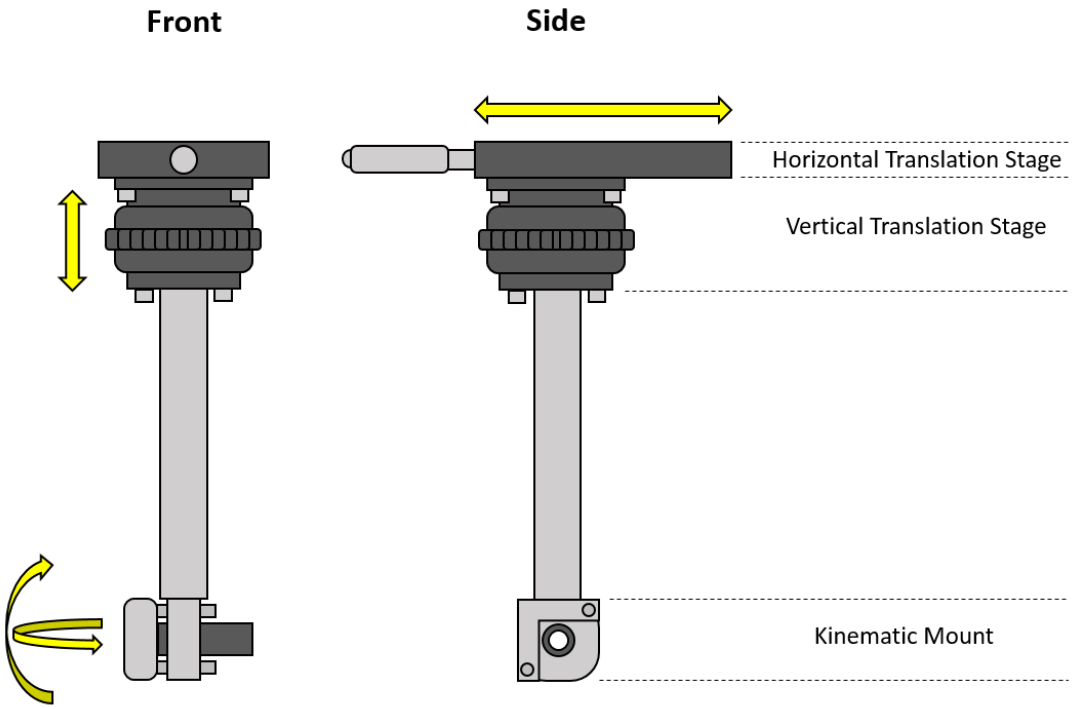

Figure 61. The collimator mounts. The combination of optical components provides four degrees of freedom in each mount.

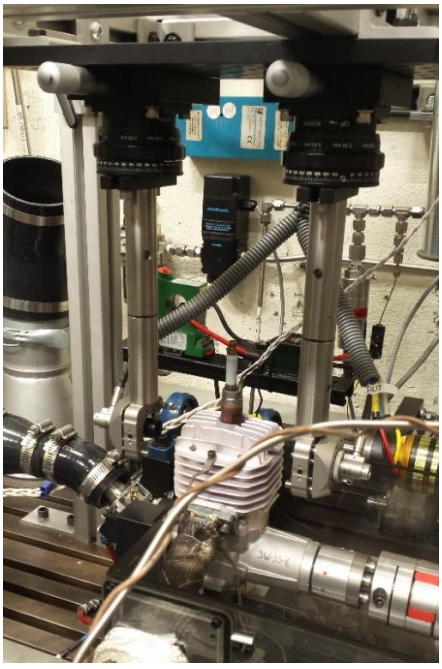

Figure 62. The collimator mounts, collimators, and fibers fully assembled and aligned with the windows in the modified engine.

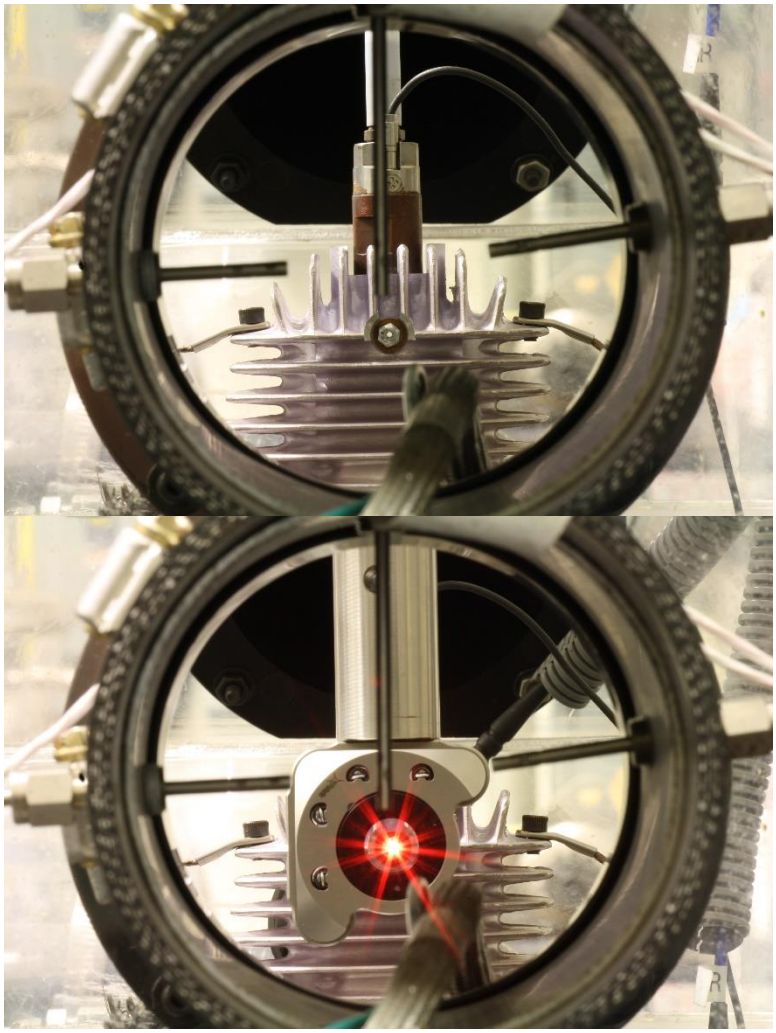

Figure 63. View through the windows on the modified engine with the collimators raised out of view (top), and with the collimator mounts in place and guiding an alignment laser through the windows (bottom). The near collimator is removed to show the laser.

2.5. Data Acquisition Setup

Figure 64 shows the data acquisition setup for the FTIR and SERB. It is organized such that the left column includes the measurement equipment from which signals originated, the center column includes the equipment that manipulated and/or digitizes the signal, and the right column includes the equipment that provided data storage and user interface. Blue indicates the original experimental setup and orange indicates equipment added later to improve signal quality, as will be described in detail in the subsequent paragraphs.

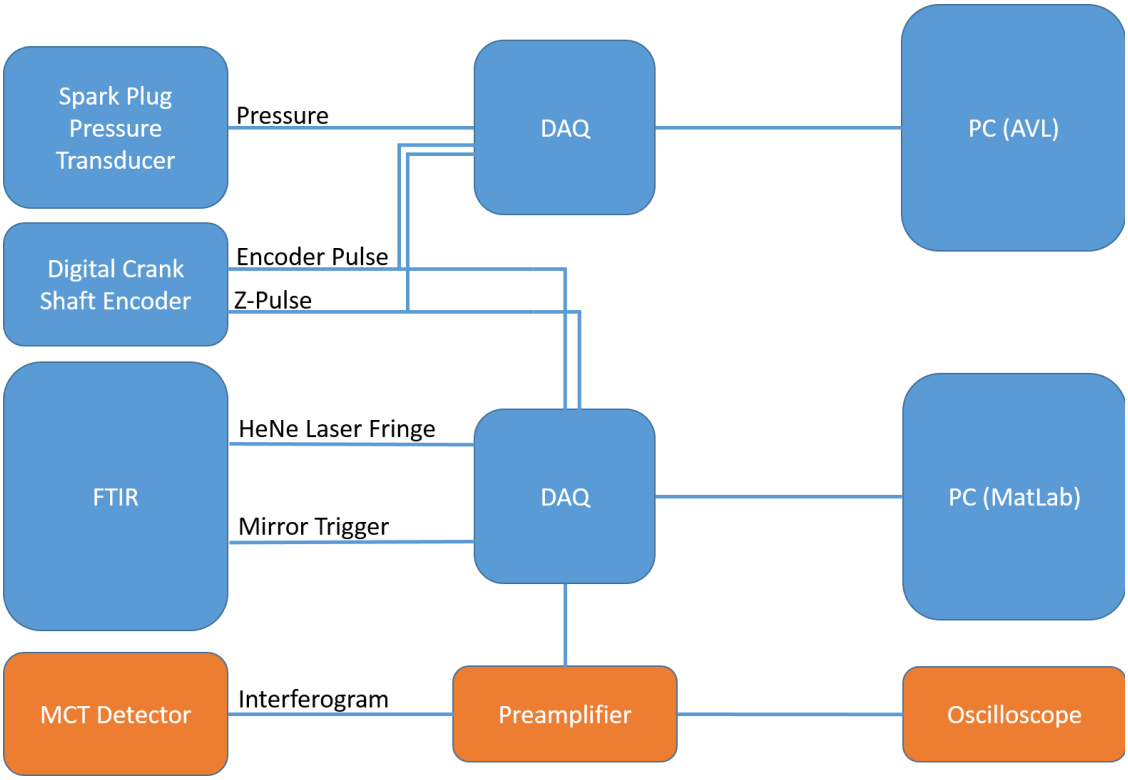

Figure 64. Data acquisition setup for the FTIR and SERB.

Early experiments used the MCT detector built into the FTIR to collect data. This detector had built-in signal processing that was optimized for measuring the static samples for which FTIR is typically employed. In particular, the signal was pre-filtered and actively adjusted to keep the baseline of the interferogram at 0 volts. When the SNR was identified as a problem in early datasets this detector was identified as a potential problem.

A new detector was set up and the signal out was coupled to a preamplifier. In Figure 64, the new equipment is indicated by orange fields. Figure 65 provides a photograph of all of the new hardware. The new detector (Figure 54) was an InfraRed™ Associates, Inc. MCT-5-0.5PV. It was DC-coupled. The detector signal was passed through a Stanford Research Systems™ SR560 low-noise preamplifier. The preamplifier applied a bandpass filter: a highpass filter to dampen the majority of low-frequency emission signal and a lowpass filter to dampen any noise at frequencies higher than the Nyquist frequency, 100 kHz. After filtering the signal, the preamplifier amplified and inverted the signal, then passed it to the Tektronix™ TDS 3034B oscilloscope and the data acquisition device (DAQ).

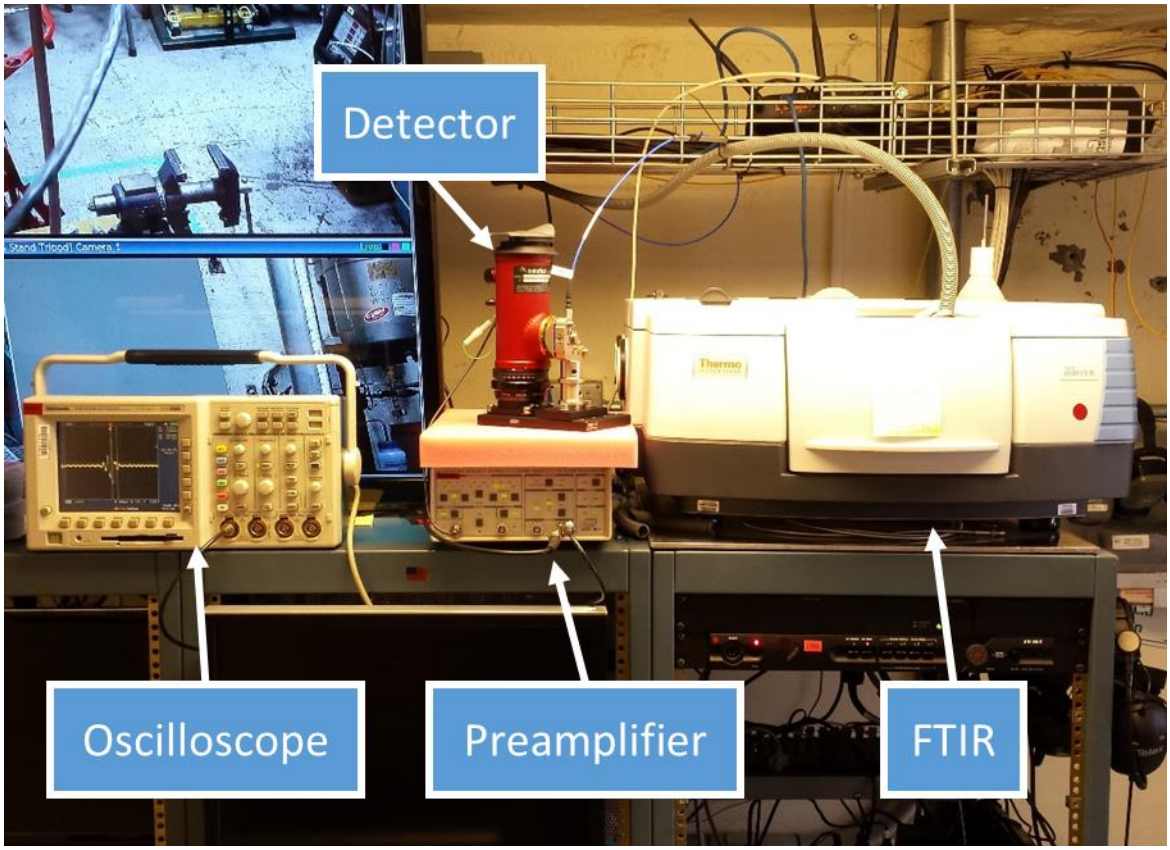

Figure 65. From left to right, the oscilloscope, the external MCT detector on top of the preamplifier, and the FTIR.

This setup provided much more control over how the interferogram was filtered and amplified prior to digitization. These corrections reduced the amplitude of the low-frequency emission signal in the interferogram with respect to the high-frequency FTIR signal to the point that, whereas previously the emission signal dominated, the two signals now had comparable amplitudes. This allowed the FTIR signal to be digitized with greater bit resolution.

The data for this study was collected at engine operating speeds as high as 7900 RPM. The desired resolution for the crank-angle-resolved temperature was 4 crank angle degrees, or 90 points per cycle. Therefore, considering only the engine, the sampling rate of the DAQ had to be at least 12 kHz. The sampling rate required for the FTIR, however, was much greater. In fact, the maximum sampling rate of the DAQ (200 kHz) became a limiting factor for the experimental setup.

The position of the mirror in the FTIR was known by tracking the interference pattern of a HeNe laser that ran parallel to the signal beam. The wavelength of a HeNe laser is 632.8 nm. The optical path difference in the Michelson interferometer increases by twice the displacement of the mirror, so every 316.4 nm the mirror moves completes another HeNe fringe. An FTIR commonly samples the interferogram at the zero-crossing of the HeNe fringe pattern, so twice per fringe, or once every 158.2 nm the mirror is displaced. In the case of this experiment it was more convenient to sample the interferogram using an external clock and ensure that the mirror speed and sampling frequency were set such that the HeNe laser fringe pattern was sampled at least twice per fringe so that counting sign changes in the HeNe laser signal is an accurate way to determine position (i.e. none of the fringes were missed/skipped). By tracking the number of times the HeNe laser fringe pattern turned from positive to negative or negative to positive and considering all of the data points after a sign change to be collected at one discrete mirror position, the position of the mirror was tracked independently of the FTIR.

The maximum sampling frequency of the DAQ was 200 kHz so the maximum possible mirror speed was 3.164 cm/s to ensure that the mirror position could be tracked by the HeNe laser fringe. The nearest mirror speed option available in the FTIR control settings that did not exceed the maximum was 2.848 cm/s. The fastest possible mirror speed was required because strong, cyclic engine emission saturated the lower frequencies of the signal. Unfortunately, all but the most recent data presented in this thesis were collected at a mirror speed of 1.898 cm/s. The emission signal was evident in frequencies as high as 20 kHz but mostly manifested itself in frequencies lower than 6 kHz. It was impossible to filter the emission out completely without losing information because the engine emission frequencies bled into the signal frequencies. Figure 66 shows the Fourier transform into frequency domain of an interferogram with engine emission signal. Here the engine was running at 6000 RPM so the primary feature due to emission is at 100 Hz. Complex cycle-to-cycle variation in the wave form of the emission signal result in major harmonics every 100 Hz that diminish exponentially with increasing frequency. Due to the mirror speed the IR absorption features for this scan would be visible between 7.5 and

15 kHz if the range of the x-axis were expanded. This is done in Figure 67. Notice that the baseline noise is elevated in frequencies as high as 60 kHz. This data has particularly weak (practically non-existent) absorption data, and the spectral features are completely lost in the baseline noise.

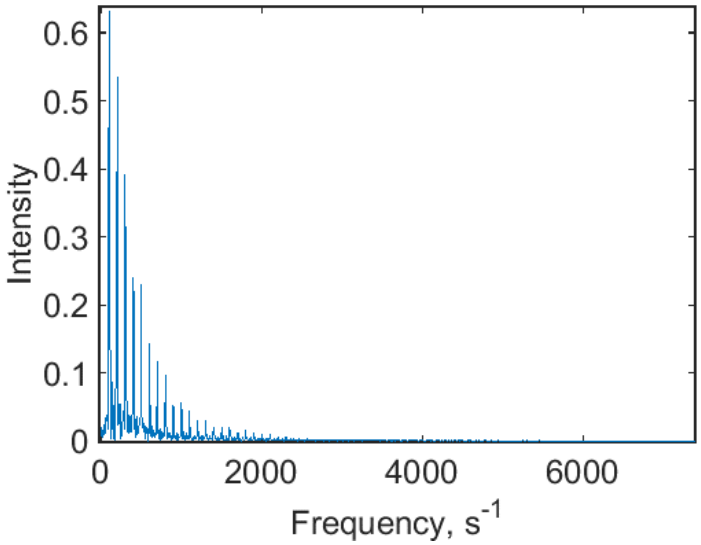

Figure 66. A Fourier transform of a typical interferogram collected in the cylinder of the engine running at a speed of 6000 RPM.

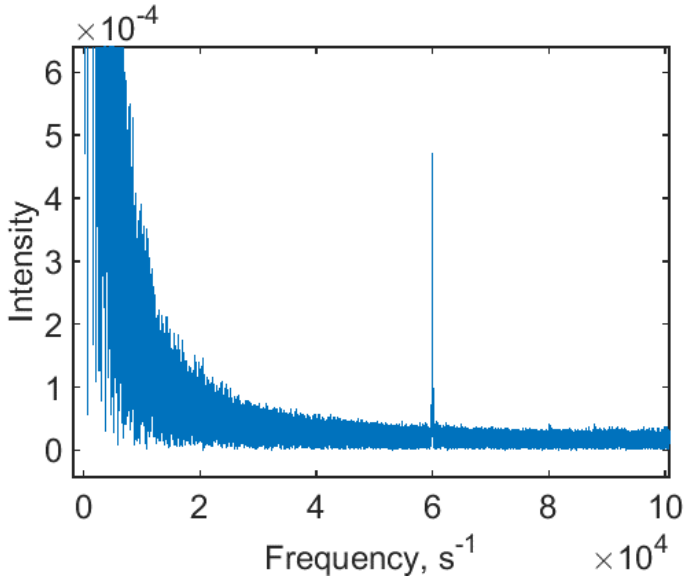

Figure 67. The same data as Figure 66, but with the baseline magnified and the limits of the x-axis extended.

The signals required to create crank-angle-resolved interferograms included the interferogram, the HeNe laser, the mirror trigger, the digital crank shaft encoder, and the z-pulse. The interferogram contained the signal data. The HeNe laser fringes were used to track mirror position. The mirror trigger was used to determine the first and last data point in each interferogram. The digital crank shaft encoder was used to track in which 4-crank-angle-degree division in the engine cycle each data point was collected. The z-pulse was used to determine which 4-crank-angle-degree division in each engine cycle fell at TDC. These 5 channels were fed to the DAQ, which was controlled by a GUI in MatLab that was written by Capt Joseph Ausserer.

The DC-coupled interferogram signal from the MCT detector was passed to a preamplifier where a bandpass filter was applied, then the signal was amplified and inverted, then sent to the DAQ. The HeNe laser and the mirror trigger signals were passed directly from the FTIR to the DAQ. The encoder and z-pulse signals were generated by a digital crank shaft encoder and passed directly to the DAQ.

A pressure signal was required for spectral fitting and was collected using a Kistler 6113BFD35Q02 integrated spark plug-and pressure transducer. The pressure trace had to be digitized by a separate DAQ from that used for the other signals to maintain the sample frequency of 200 kHz. Consequently, the pressure trace was sampled on a separate clock and there was not a one-for-one match between interferogram data and pressure data. Instead, a 400-cycle sample of independent pressure data was collected while the FTIR collected data and combined to produce a cycle-averaged pressure trace. An example pressure trace is shown in Figure 68 below.

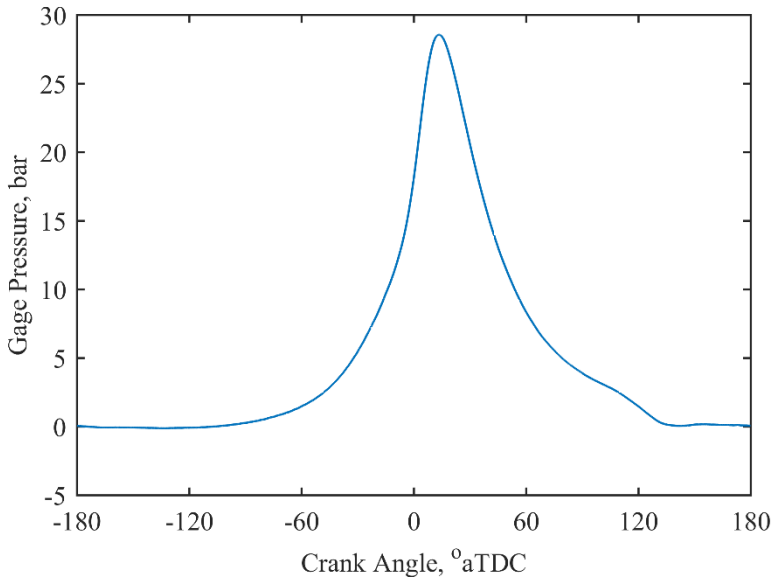

Figure 68. A typical cycle-averaged pressure trace from the spark plug mounted pressure transducer.

3. Data Processing

As explained previously, the purpose of this research was to determine the crank-angle-resolved bulk gas temperature inside the cylinder of a small ICE. FTIR spectroscopy is limited to analysis of samples in steady state because thousands of data points must be collected as a mirror traverses from one position to another over some finite period of time to re-construct information about any given wavenumber of light with a Fourier transform.

In this way an FTIR scan is similar to a long-exposure photograph. In photography, if the image changes while the shutter is open the result is a blurry picture. Similarly, in FTIR spectroscopy if the sample changes in the time it takes the mirror to traverse, the transformed data is distorted. It will be some blend of the changing states in the sample or pure noise if the changes in the sample are dramatic enough.

In order to perform FTIR spectroscopy on a dynamic process like engine combustion, the process must simply "look" static from the perspective of the FTIR. This can be achieved if the time scale of the mirror scan may be made sufficiently small in comparison to the time scale of the dynamic changes. If the process is cyclical or repeatable, the mirror may be parked at one position at a time while the process is repeated for all mirror positions, then data can be grouped

by time after the start of the process to create time-resolved interferograms. The same concept can be applied without parking the mirror so long as the position of the mirror is tracked and enough scans are taken at different moments throughout the process to do the same type of data grouping. For these experiments it was assumed that the cycle-to-cycle variation of gas composition across the path of the beam was negligible. This assumption allowed data points from many mirror scans that happened to fall in the same part of the engine cycle to be stitched together, creating crank-angle-resolved interferograms for as many divisions of the engine cycle as was desired.

Obtaining crank-angle-resolved interferograms, however, was only the first step in data processing. The full process, from raw interferograms to a crank-angle-resolved temperature profile, is summarized in Figure 69. The remainder of this section describes each step of the process in detail.

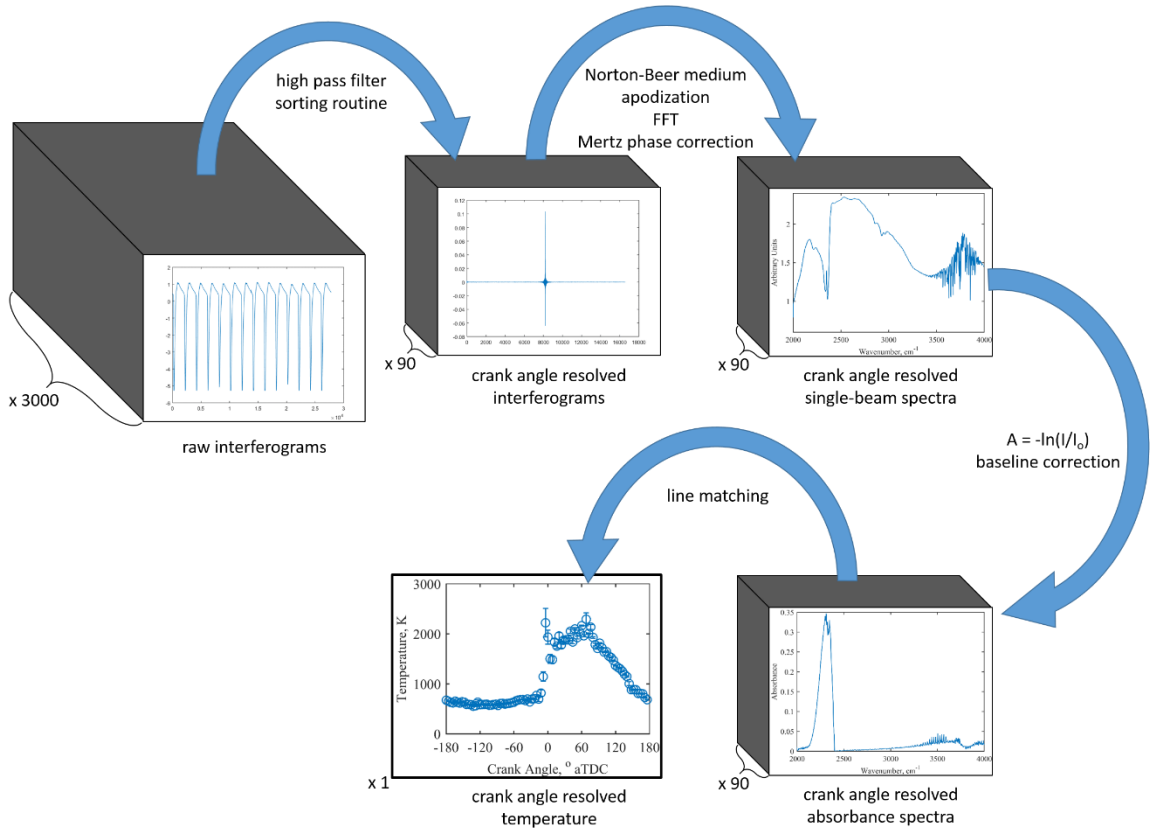

Figure 69. Graphical summary of the data processing procedure.

3.1. Data Distribution

This data collection scheme depended on the engine speed to be independent of the mirror scanning speed, such that over a long period of time data points would be distributed equally in every crank angle/mirror position bin. This could be checked by bringing the engine to condition and conducting about 300 scans, then plotting the portions of an interferogram from about 2000 engine cycles, one on top of another, as shown in Figure 70. This plot will be shown for several datasets and is hereafter called a "stack plot". Prior to plotting the interferograms they were filtered with a Butterworth bandpass filter to diminish the engine emission signal and eliminate any high-frequency sources of noise. Approximately 1 in 16 cycle-long interferogram portions contained a centerburst. The even distribution of the centerbursts indicates that the FTIR sample rate was independent of the engine cycle rate when this sample was taken. The distribution of scans never became an issue during this research.

After sorting data into bins, a second check was conducted. Each bin was checked to ensure that it had at least one data point. Data collection consisted of 3000 scans at any given operating condition, the interferograms were sampled approximately 1.65 times per mirror position, and the engine cycle was divided into 90 parts, so the average number of data points per bin was 55. The standard deviation of number of data points per bin for any given crank-angle-resolved interferogram was approximately 10.

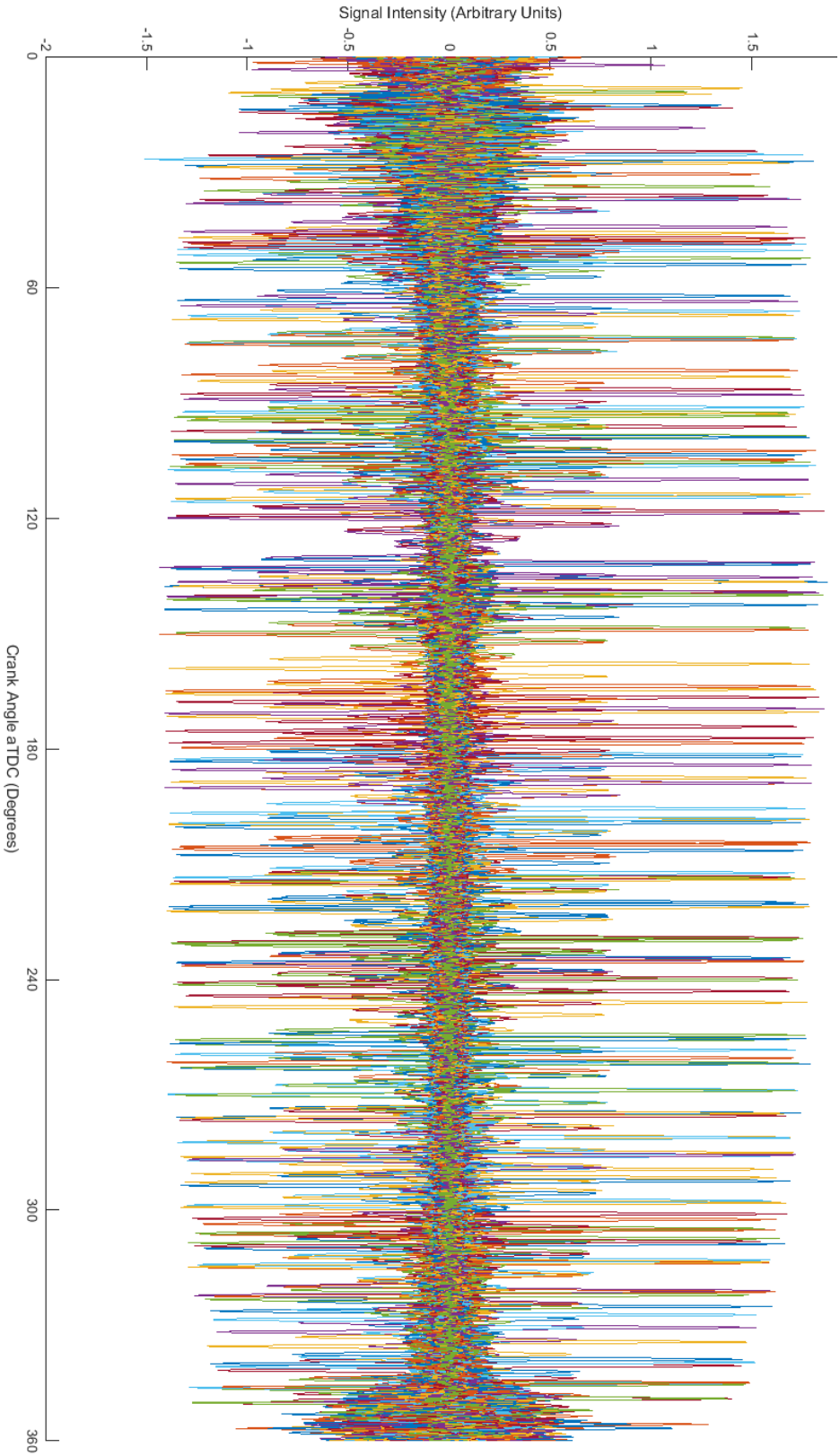

Figure 70. An example of a "stack plot": the continuously-overlaid interferogram signal in the crank angle domain. 2,000 consecutive engine cycles are presented here.

3.2. Sorting Data

Data was collected at a frequency of 200 Hz. Every data point consisted of an interferogram signal value, a HeNe laser signal value, a mirror trigger signal value, an engine encoder signal value, and a z-pulse signal value. The interferogram signal was the information to be re-organized and averaged, the rest of the values were used to sort the interferogram values correctly, like an address on a letter. Interferograms taken in the engine cylinder sampled a dynamic, cyclical process with strong emission. The raw interferograms looked like the one in Figure 71. This figure is representative of what raw interferograms looked like with the "new" experimental setup: a detector coupled directly to a preamplifier so that a high-pass filter could be applied and reduce the combustion emission signal before amplifying the interferogram for analog to digital conversion. These interferograms were improved further by the application of a digital bandpass filter that passed only the frequencies at which data signal was present (Figure 72).

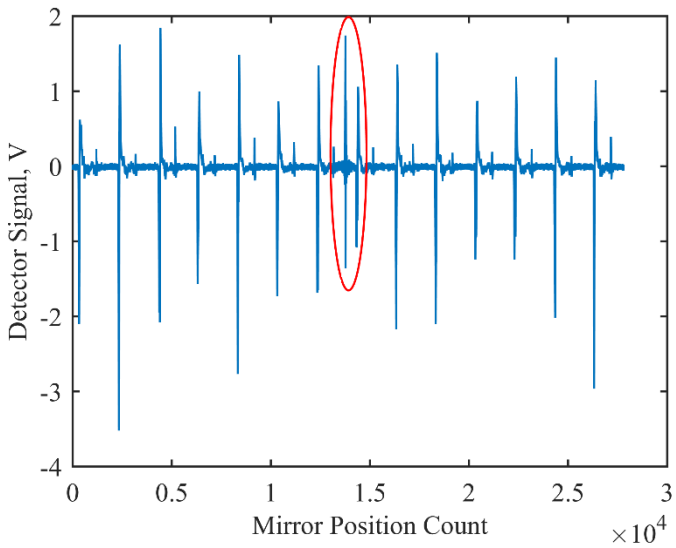

Figure 71. A typical interferogram from the engine cylinder. Centerburst circled in red.

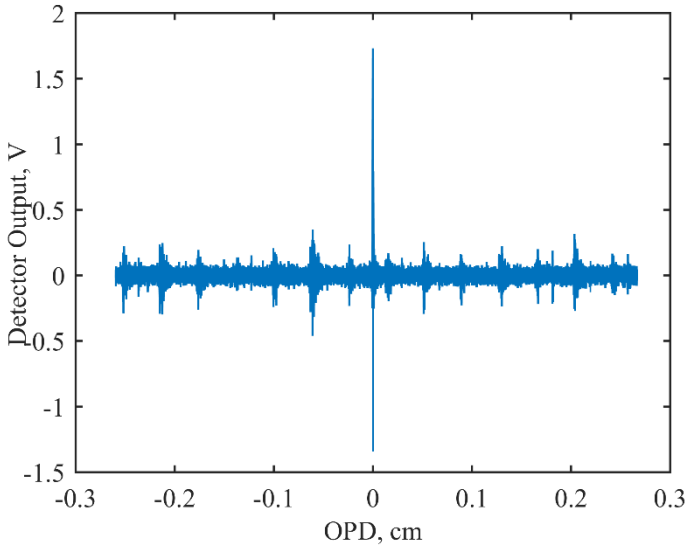

Figure 72. A typical interferogram from the engine cylinder after the digital application of a bandpass filter.

The HeNe laser signal was the analog interference pattern of a HeNe laser passed through the Michelson interferometer. It was a minimally sampled sinusoid with an amplitude of about 2.5 volts. Figure 73 is an example of a HeNe laser fringe pattern sampled at 200 kHz. The value of any given data point in this signal was insignificant, but the relative values of adjacent data points were used to determine the position of the mirror within ± 79.1 nm. This was achieved by recognizing that the HeNe laser fringe pattern changes sign every half HeNe fringe. A mirror position was assigned to every interferogram data point by incrementing the mirror position by 158.2 nm every time the HeNe fringe pattern changed sign.

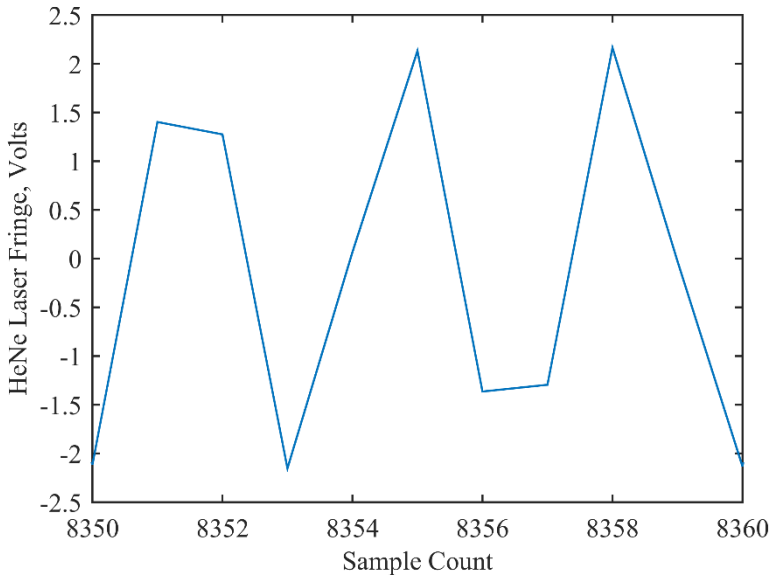

Figure 73. HeNe laser fringe pattern.

When averaging many data points with the same mirror position together, the true mirror position of each point in the averaged set was within 158.2 nm of every other point. An FTIR commonly samples the interferogram by triggering off the zero-crossing of the analog HeNe laser fringe pattern. This provides better repeatability from one scan to the next and consequently higher SNR in spectra generated from multiple scans. Improved SNR could be gained in the data collected from this research by weighting the value of each interferogram data point based on the intensity of the HeNe laser fringe associated with that point before taking an average. This is one recommended area for future work.

The mirror trigger signal was used to determine the start and stop times for each data collect. The z-pulse signal from the optical crankshaft encoder (Figure 74) for one interferogram is shown in Figure 75. The z-pulse was used to determine the start and stop times for each engine cycle. A sample of the encoder pulse signal is shown in Figure 76. The encoder signal was used to divide the engine cycle into 900 equal parts, each consisting of 0.4 crank angle degrees. Only 90 engine cycle divisions were required for this experiment, so every 10 crank angle positions were grouped together to create a single interferogram.

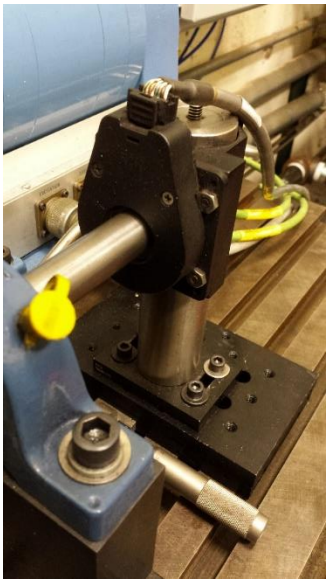

Figure 74. The optical crankshaft encoder from which the encoder pulse and z-pulse originate.

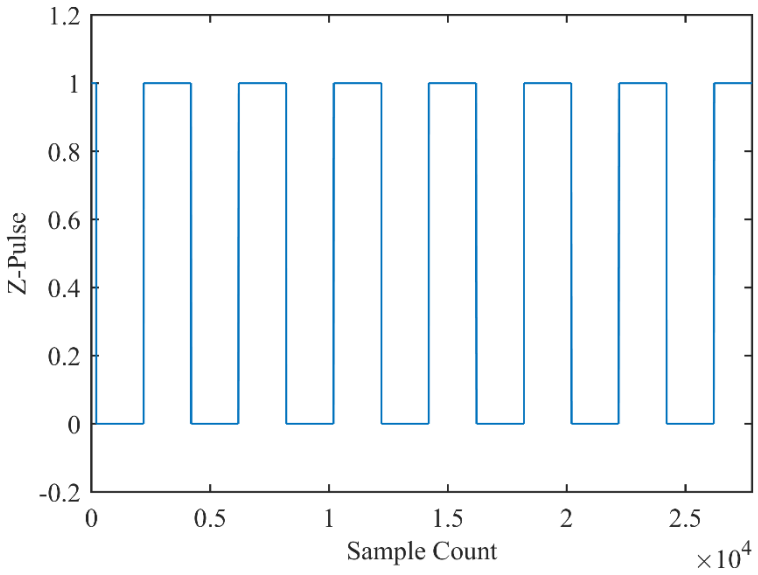

Figure 75. Digital signal with the z-pulse.

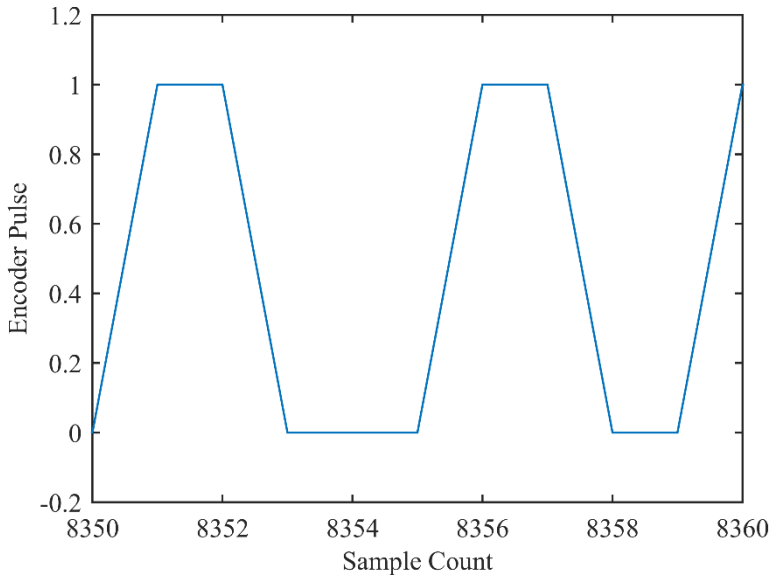

Figure 76. Digital signal with the 900-per-revolution encoder pulse.

The combination of these signals, along with the HeNe laser fringe signal, were used to determine the mirror position, $\Delta(t)$, and the crank angle, $\theta(t)$, associated with each interferogram data point, I(t). Figure 77 graphically describes the process of sorting the data. The data was "binned" such that every unique Δ and θ combination constituted a bin in a large matrix of bins. The data points that fell in each bin were averaged, and the standard deviation was calculated to determine how well the assumption of negligible cycle-to-cycle variation held true. The collection of averaged data points for all Δ at a given θ was the crank-angle-resolved interferogram for that crank angle θ.

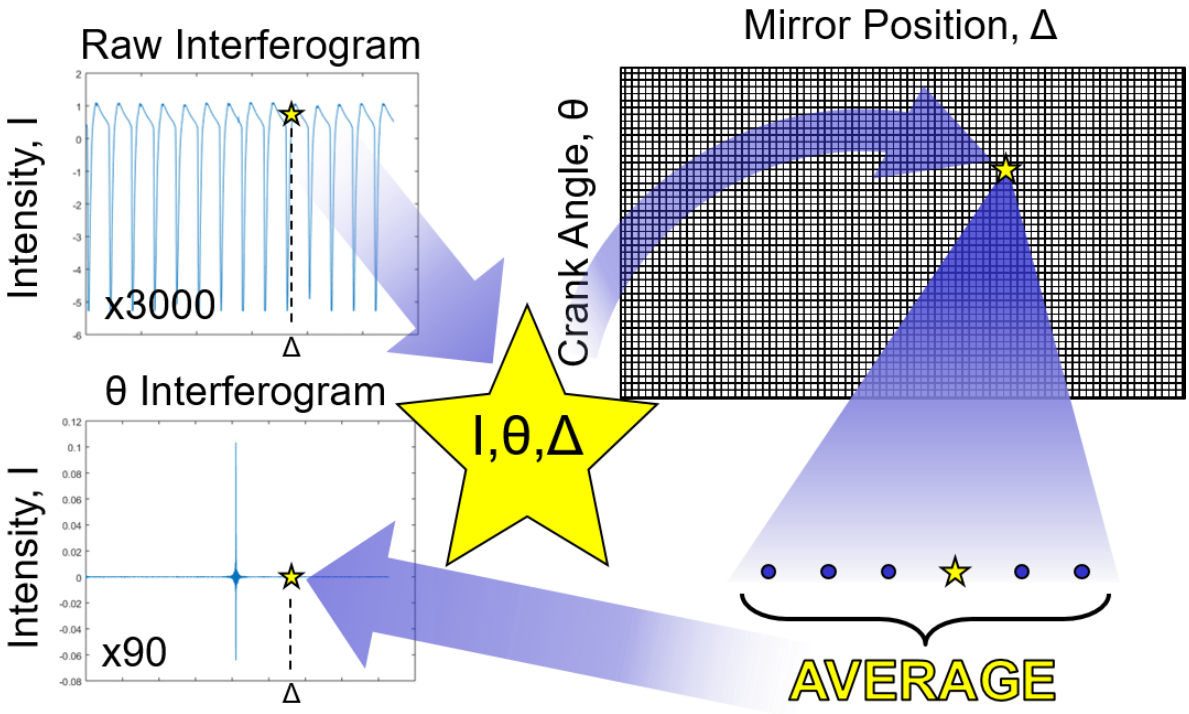

Figure 77. Graphical representation of the data sorting process.

Enough scans had to be collected to ensure that every Δ – θ bin had at least one data point, and ideally many. Exactly how many scans were required to fill every bin? The number varied due to the random manner in which bins were populated, so each data set was checked for empty bins. How many data points were required in each bin to get quality data? This was determined empirically and is discussed in Chapter IV, Results, in Section 4. Here it suffices to say that with 3,000 scans and a mirror speed of 1.898 cm/s the number of data points averaged to produce each data point in a crank-angle-resolved interferogram was an average of 56 with a standard deviation of 10.

Figure 78 shows an example interferogram collected in-cylinder that has been digitized and passed through a bandpass filter. The baseline noise level is very high, approximately 0.2 V peak-to-peak, and there are noticeable signal spikes other than the centerburst that remain from the imperfectly filtered emission signal.

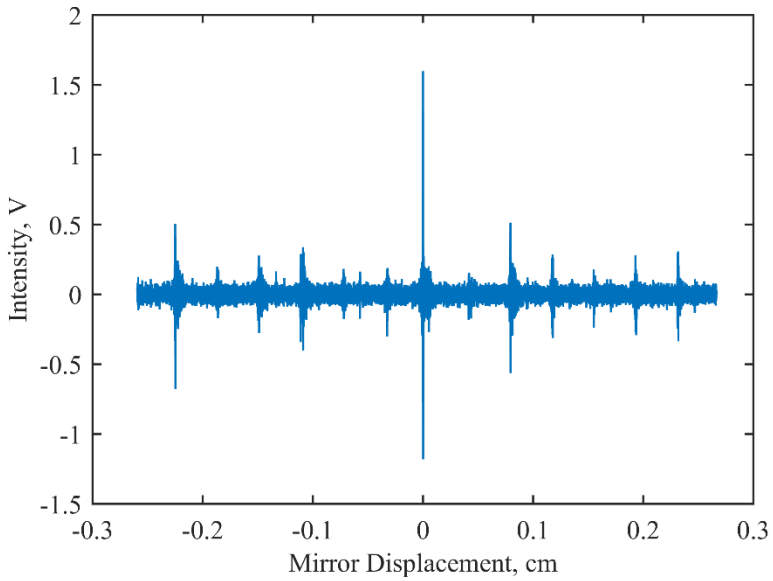

Figure 78. Raw interferogram with bandpass filter applied prior to digitization.

Figure 79 is an example of a crank-angle-resolved interferogram that results from the sorting algorithm. Figure 80 provides an even closer look at the centerburst. The baseline noise in these plots is indecipherable in relation to the centerburst, which instills confidence that both the sorting algorithm is working and the number of samples taken in the cylinder is sufficient.

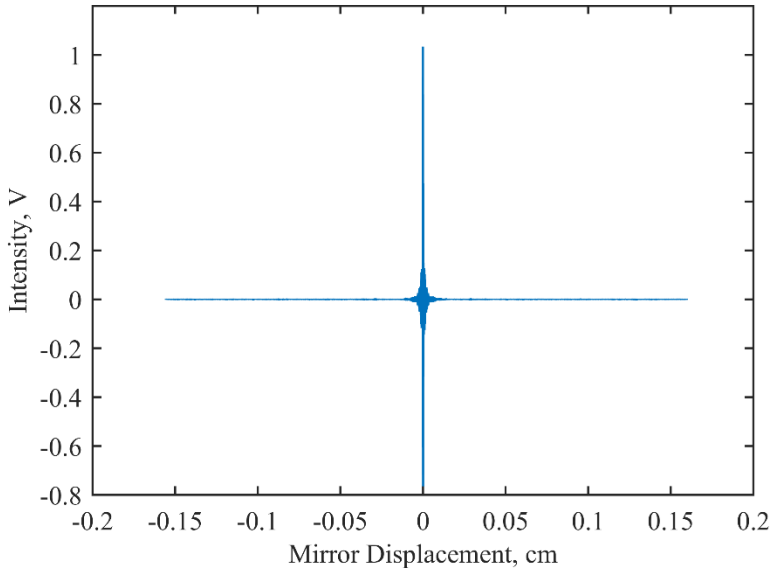

Figure 79. Crank-angle-resolved interferogram demonstrating the success of the sorting algorithm.

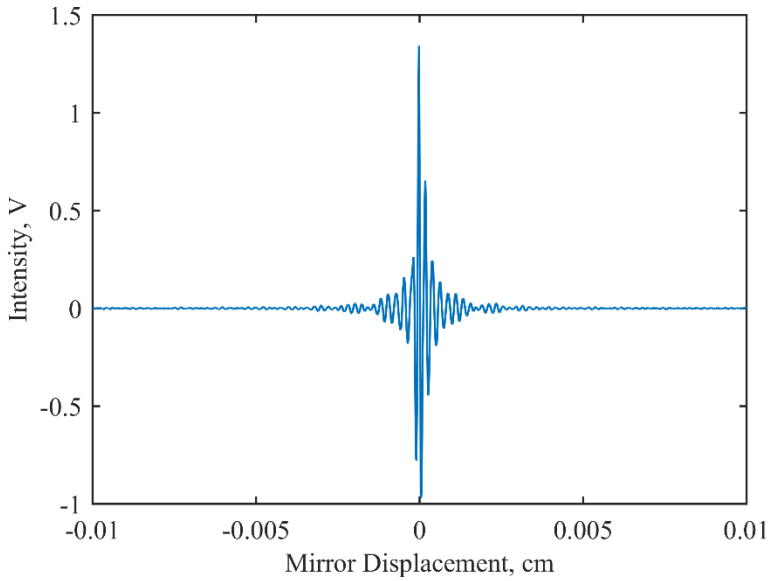

Figure 80. Close-up of the centerburst for a crank-angle-resolved interferogram.

The examples above are provided from regions of the engine cycle that are highly repeatable from one cycle to the next. The sorting algorithm combines data points from many engine cycles to create a single data point in a single crank-angle-resolved interferogram. Therefore, the effect of one particularly poor raw interferogram (which may come about because, say, a window was obstructed temporarily by a build-up of soot that eventually burned off) would be distributed randomly across all of the crank-angle-resolved interferograms in the dataset. One could imagine that if high cycle-to-cycle variation were associated with any given part of the engine cycle, the crank-angle-resolved interferograms for that part of the engine cycle would have a particularly high baseline noise threshold. This was observed at the parts of the engine cycle where combustion and gas exchange occurred. Figure 81 shows an example of a crank-angle-resolved interferogram taken near TDC, where high cycle-to-cycle variation due to combustion is evident. The impact of this variation on temperature analysis is discussed at length in Chapter IV, Results.

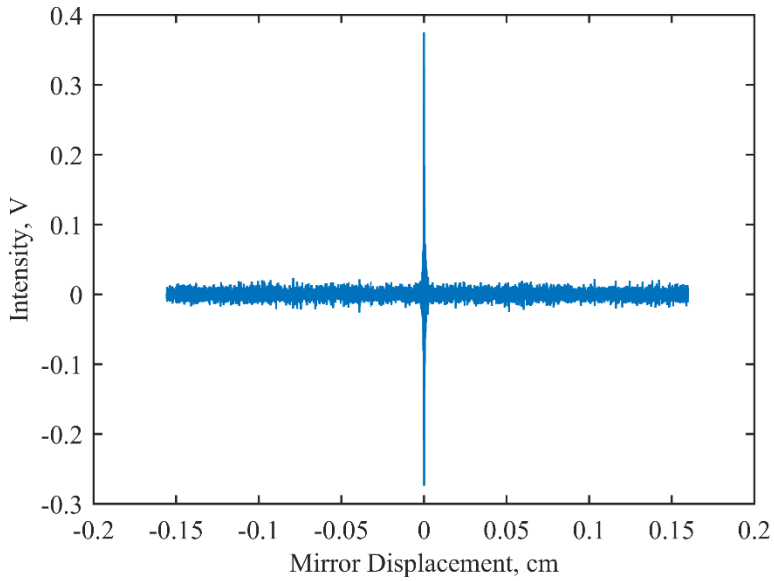

Figure 81. Crank-angle-resolved interferogram near the region of high cycle-to-cycle variation due to combustion.

3.3. Crank-angle-resolved Interferograms

A few steps were necessary to prepare the crank-angle-resolved interferograms for the Fourier transform. The DC components were removed by subtracting the mean value from every interferogram. This prevented the distortion that can effect a spectrum due to a strong feature with a sharp cutoff at a wavenumber of zero.

A moderate apodization function was applied to each interferogram to minimize ringing in spectral features. The Norton-Beer Medium function was found to give the best results.

The end of each interferogram was padded with zeros. Enough zeros were added to each interferogram to make the number of data points a power of two. Doing this improved the processing time required to perform the Fourier transform, as will be explained in greater detail in the next section. Zero-padding the interferogram also has the effect of increasing the data point density in the spectrum. It is, in effect, a method of interpolation for the spectrum [29]. With these steps completed the crank-angle-resolved interferograms were ready for the Fourier transform.

3.4. From Interferograms to Absorbance Spectra

The Fast Fourier Transform (FFT) algorithm was used to perform the Fourier transform in MATLAB®. This algorithm was proposed by Cooley and Tukey as a way to reduce the

computation time required to perform a Fourier transform [30]. The algorithm is most computationally efficient when the number of data points being transformed is a power of two. Efficiency was important for this study due to the quantity of data being manipulated for each sample. Adjusting the number of data points to meet this requirement can be accomplished by padding the wings of the interferogram with zeros, as explained in detail in the previous section.

The transform resulted in complex spectra due to the asymmetry of the interferograms, a common issue in FTIR spectroscopy. The true single-beam spectra were restored from the real and imaginary parts of the complex spectra using Mertz phase correction [31, 32]. Background interferograms were processed in the exact same way as sample interferograms up to this point to make available background spectra. The crank-angle-resolved transmittance spectra were calculated by taking the ratio of each single-beam spectrum to the appropriate background spectrum. The crank-angle-resolved absorbance spectra were calculated by taking the negative of the natural log of transmittance spectra. Absorbance spectra were used for quantitative analysis using Beer's Law.

Griffiths and de Haseth include a section in their book, Fourier Transform Infrared Spectrometry, titled "Fourier Transform: Pictorial Essay", to summarize the process by which a raw interferogram is transformed into a spectrum using Mertz phase correction. The discussion here follows the same procedure presented in Griffiths and de Haseth, illustrated using data collected on the SERB. Commercial FTIRs generally come with software that manages the procedure described here. The unique requirements of the data acquisition for this study, especially the high rate of data collection and data sorting could not be handled by the available commercial software.

A typical interferogram is shown in Figure 82. It is characterized by an intense centerburst at the ZPD mirror position that quickly tapers off into the wings on either side. An ideal double-sided interferogram is symmetric about zero because the interference pattern should be identical regardless of the sign of the phase shift of the two beam paths. Optical, electrical, or sampling effects can lead to frequency-dependent phase shifting of the interference pattern,

which manifests itself as asymmetry in the interferogram [7]. This phenomenon is also called chirping. Mertz phase correction is used to account for chirping after taking the Fourier transform of the interferogram.

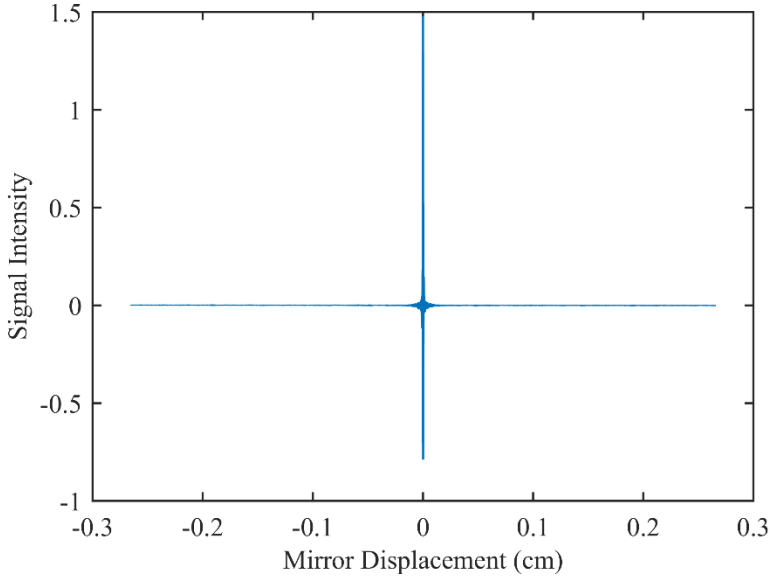

Figure 82. A raw interferogram sampled from atmosphere.

It is useful to take the zero-phase shifted interferogram prior to the Fourier transform. To do this, the interferogram is split at the maximum, then the left half is added to the wing of the right half with zero-padding in between. This procedure does not change the resulting data, but it does change the order in which the resulting data is presented, in such a way that is

computationally advantageous to do so. The zero-phase shifted interferogram is shown in Figure 83.

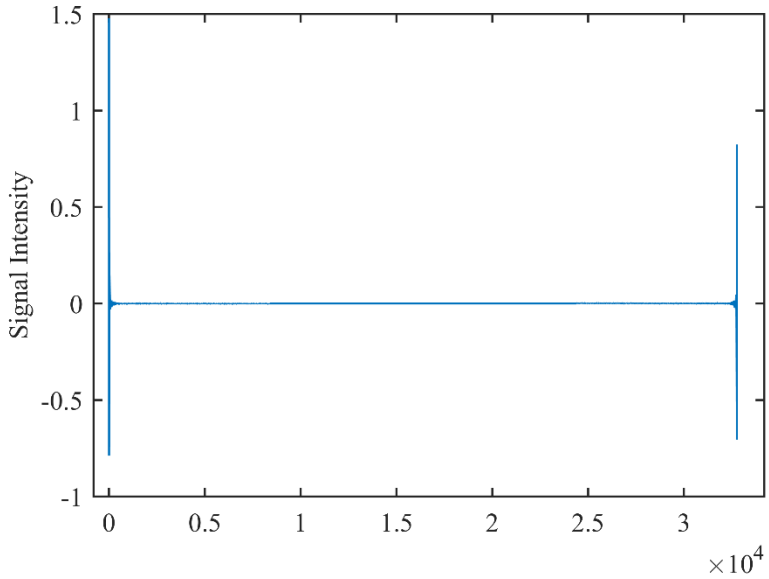

Figure 83. The zero-phase shifted interferogram.

When the interferogram being transformed is asymmetric, or chirped, the result of a Fourier transform is a complex spectrum. The real and imaginary portions of an example spectrum are presented in Figure 84 and Figure 85, respectively. The true spectrum cannot be recovered by simply determining the magnitude of the real and imaginary parts. Rather, the real

and imaginary portions of the complex spectrum are related to the true spectrum by a number of trigonometric functions.

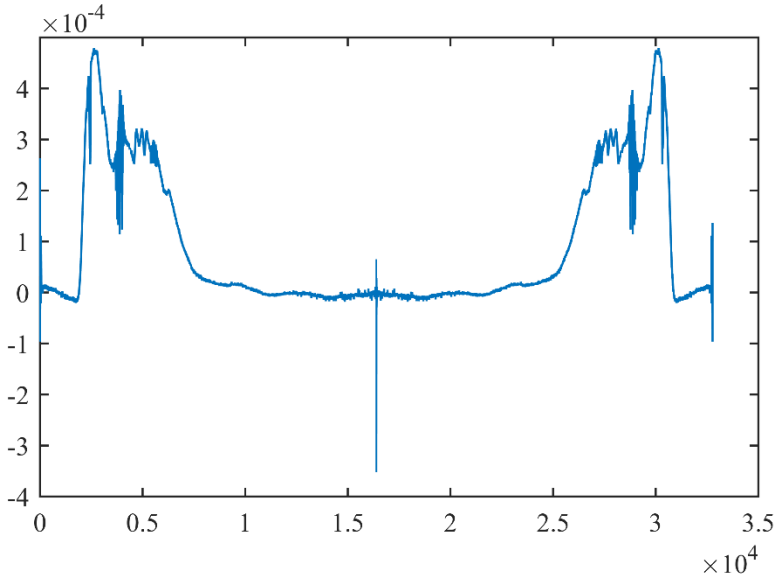

Figure 84. The real portion of the complex spectrum, an even function.

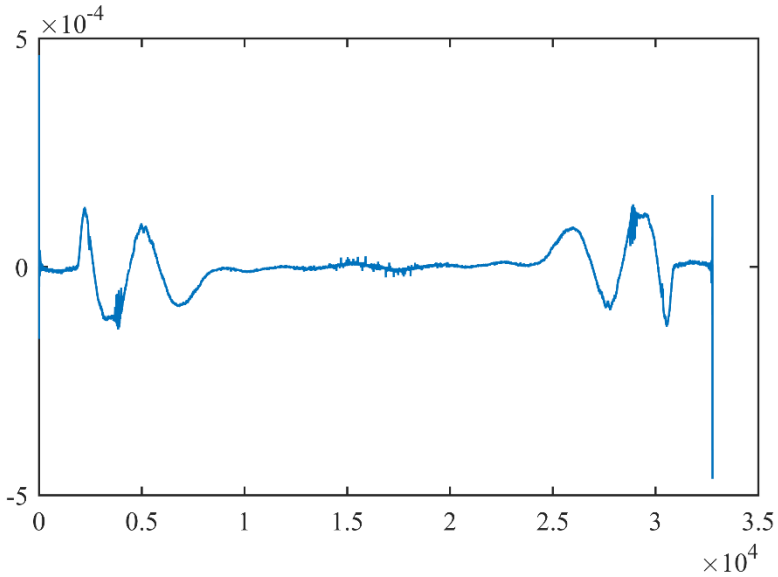

Figure 85. The imaginary portion of the complex spectrum, an odd function.

The first step required to recover the true spectrum from the complex parts is to calculate the phase curve (Figure 86). It is related to the real and imaginary parts of the complex spectrum

by Eq. (27). The phase curve indicates the phase shift of the interference pattern as a function of wavenumber, and can be used to re-construct the true spectrum.

$$\theta_{\tilde{v}} = arctan\frac{Im(\tilde{v})}{Re(\tilde{v})} \tag{27}$$

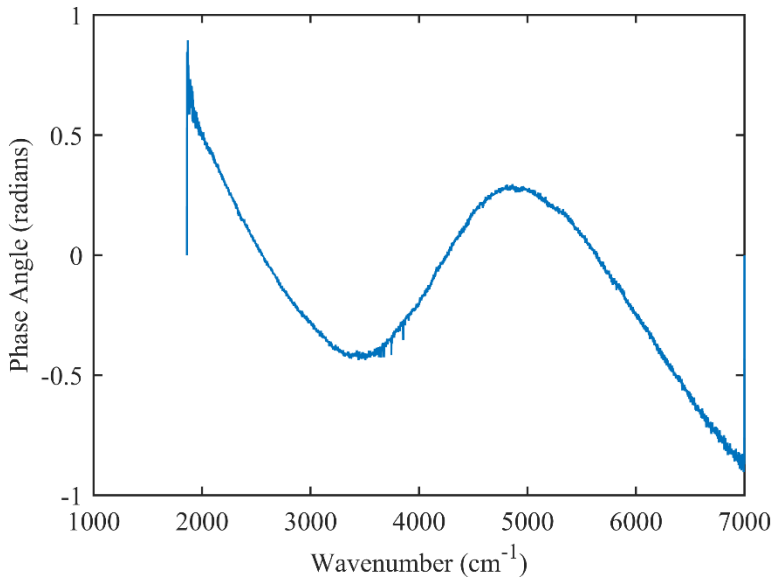

Figure 86. The phase curve.

The cosine and sine functions of the phase curve were calculated as intermediate steps to re-construct the true spectrum. They are shown in Figure 87 and Figure 88, respectively.

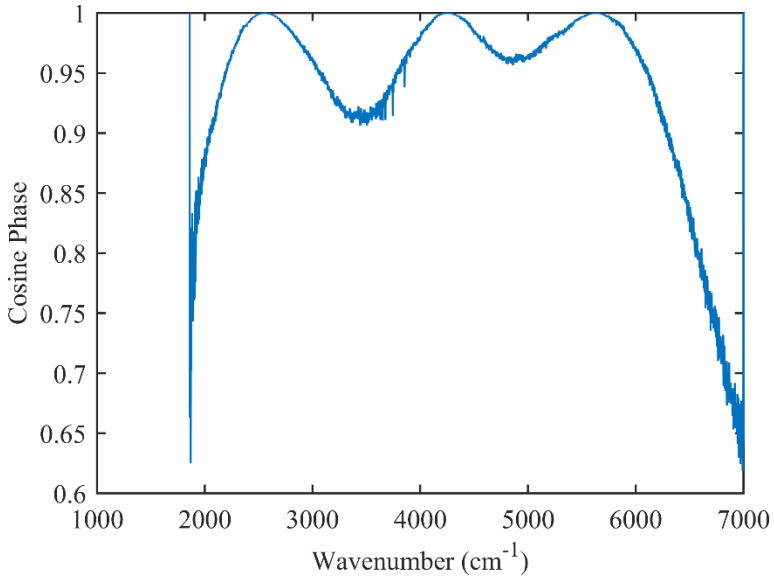

Figure 87. The cosine function of the phase curve.

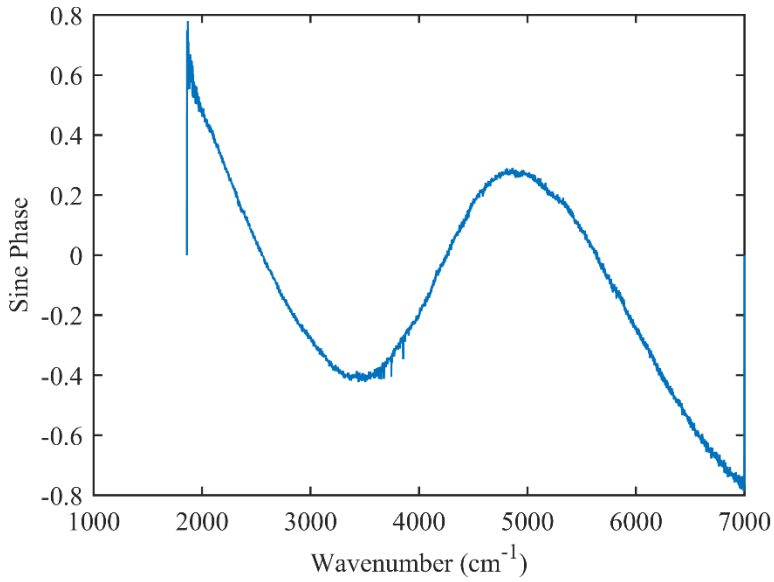

Figure 88. The sine function of the phase curve.

The next step in the process is to multiply the real portion of the complex spectrum by the cosine function of the phase curve, as shown in Figure 89, and multiply the imaginary portion of the complex spectrum by the sine function of the phase curve, as shown in Figure 90. The sum of these two products is the true spectrum, shown in Figure 91. This process is summarized by:

$$I(\tilde{v}) = Re(\tilde{v}) \cos \theta_{\tilde{v}} + Im(\tilde{v}) \sin \theta_{\tilde{v}} \quad (28)$$

The spectrum in Figure 91 is called a single-beam spectrum because the spectra used for analysis are typically the ratio of two such spectra: one sample spectrum and one background spectrum. A single-beam spectrum is the truest representation of the intensity of light as a function of wavenumber that is incident on the detector when the measurement is taken. The general shape of the curve is called the instrument line shape (ILS) because its shape is

determined by the emission properties of the IR source and the transmission limitations of the various optical components. The sharp lines that fall from the ILS are absorption features.

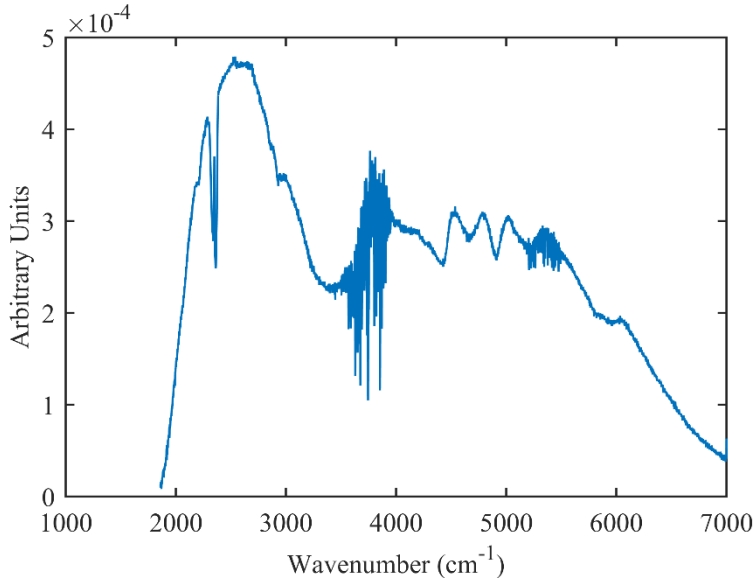

Figure 89. The real portion of the complex spectrum multiplied by the cosine function of the phase curve.

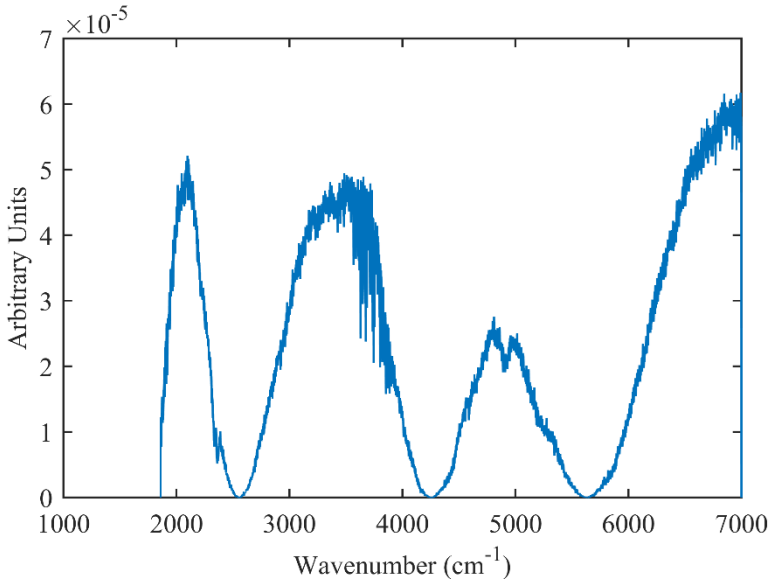

Figure 90. The imaginary portion of the complex spectrum multiplied by the sine funciton of the phase curve.

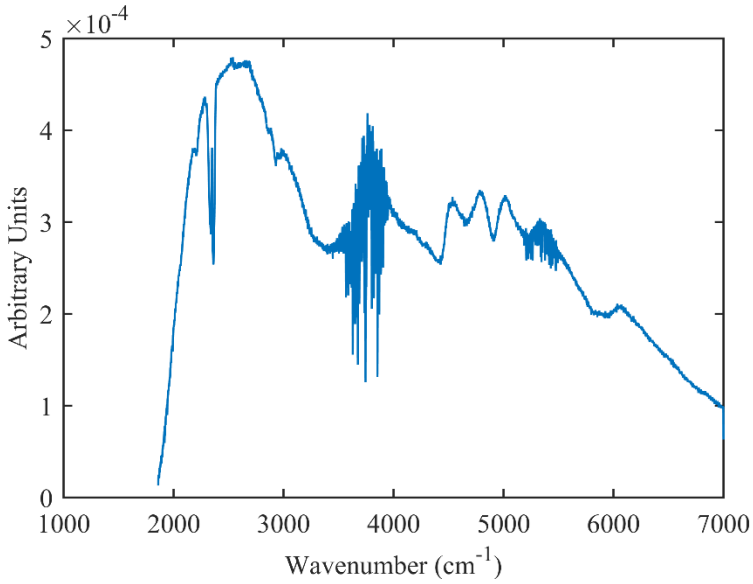

Figure 91. The true spectrum: the sum of the functions in Figure 89 and Figure 90.

While valuable insight concerning the experimental setup can be gained by looking at the ILS in the single-beam spectra, it does not provide any information about the gas under examination in the test cell. This information is isolated by calculating the transmittance spectrum. The transmittance spectrum is the ratio of a single-beam sample spectrum to a single-beam background spectrum, as shown in Eq. (22). The background spectrum can be taken by removing the gas sample from the test cell and replacing it with a vacuum or a nitrogen gas purge.

When analyzing spectra it is desired that, as much as possible, the absorption features in the single-beam sample spectra are caused by the gas in the test cell and not by additional absorbers in the experimental setup (e.g. humid air in the FTIR body) because the additional absorbers are often difficult to control and reduce the signal available for transmission through the test cell. This is why the FTIR and any other region in the beam path are purged with non-absorbing nitrogen gas when possible. The ideal experimental setup would be capable of producing single-beam background spectra that have no absorption features at all, but are pure

representations of the ILS. In reality some absorption features will always be present and it is not practical to maintain a nitrogen purge in certain parts of some experimental setups.

Figure 92 is an example of a single-beam background spectrum taken on the SERB. In this case there are strong absorption features because a purge was not maintained through the beam path. The features near 2300 cm^{-1} are due to CO_2 absorption. The resolution of this spectrum is 4 cm^{-1} so what looks like two large features is really the combined effect of many absorption lines. The features from about 3500 cm^{-1} to 4000 cm^{-1} are due to H_2O absorption.

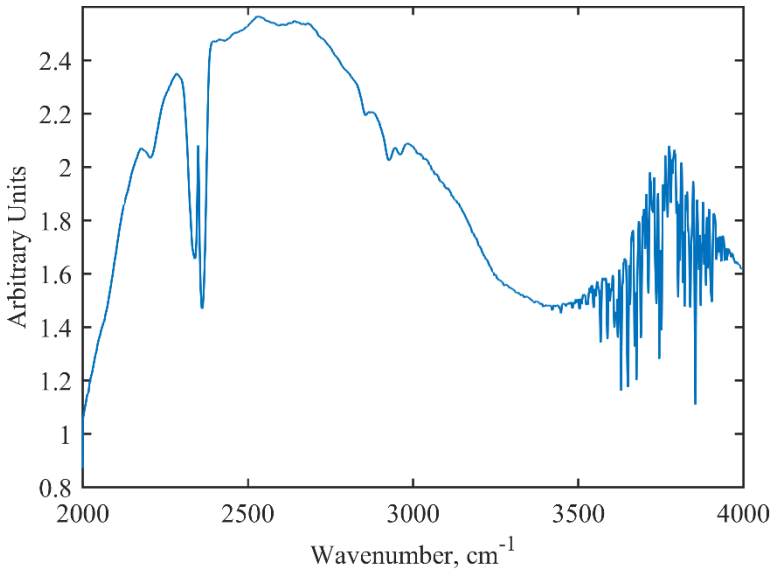

Figure 92. A single-beam background spectrum with some undesirable absorption features.

Figure 93 is a sample spectrum from the same dataset. In this case, the sample is a candle flame that has been introduced to the beam path. The absorption due to CO_2 is clearly stronger

with the flame in the path of the beam. The increase in absorption due to H_2O is less obvious. Calculating the transmittance will bring out these features.

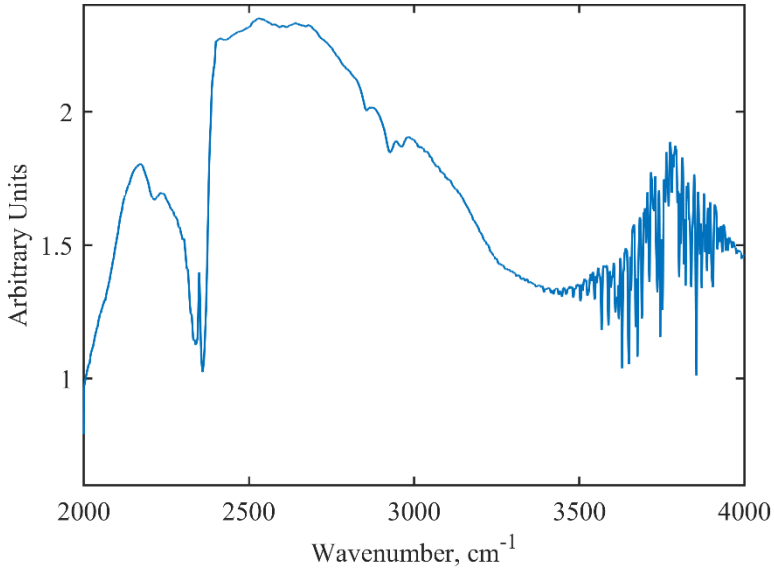

Figure 93. A single-beam sample spectrum with stronger absorption than was observed in the background spectrum.

Figure 94 shows the transmittance spectrum. Because the background spectrum is divided out of the sample spectrum to calculate transmittance, it is reasonable to interpret the transmittance to be the percentage of signal (as a function of wavenumber) that is transmitted through the width of the flame, a path length of approximately 1 cm. While it was not possible

to purge the entire beam path in this instance (or else the flame would have been quenched), calculating the transmittance isolated the physical phenomenon of interest.

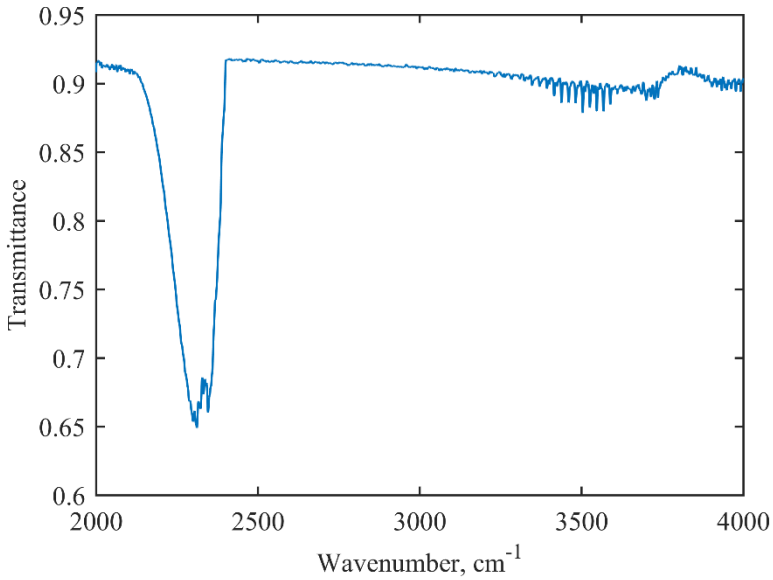

Figure 94. The transmittance through the candle flame.

Quantitative analysis is made possible by Beer's Law, Eq. (24), which states that absorbance is proportional to absorptivity, species concentration, and path length. Absorbance is

related to transmittance by Eq. (23). Figure 95 is the absorbance for the candle flame example above.

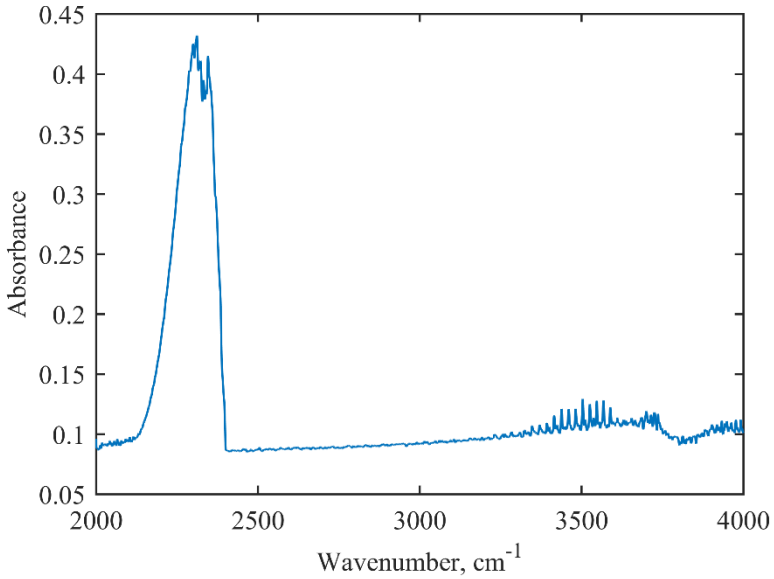

Figure 95. The absorbance through the candle flame.

3.5. Baseline Correction

An ideal transmittance spectrum would look like a straight horizontal line at a transmittance of one (i.e. 100%), with features suspended down at various wavenumbers. Transformed into an absorbance spectrum, this would look like a straight horizontal line at an absorbance of zero, with features rising up. In both cases the straight horizontal line is called the baseline of the spectrum. There are many reasons why the baseline might stray from the ideal, to include the effects of scattering, reflection, temperature, concentration, or instrument anomalies when the sample is introduced to the beam path [7]. If the baseline of a measured spectrum is found to be offset from 100% in the case of transmittance or zero in the case of absorbance, or the baseline is not a horizontal line, then baseline correction is required prior to quantitative analysis.

The simplest scenario is when the baseline is still horizontal, but offset from where it should be. This means that the source of the anomaly has affected every wavenumber equally. This can be corrected by subtracting the minimum value from the absorbance spectrum or by dividing the transmittance spectrum by its maximum value. These operations are equivalent due

to the relationship between absorbance and transmittance expressed by Eq. (23). Baseline corrections that require a more complex shift can only be done with the spectrum linear in absorbance [7].

A slightly more complex correction can be made when the baseline looks like a sloped line. Two points that fall on the baseline are selected and the line that passes through them is subtracted from the absorbance spectrum. Even more complex baseline corrections can take the form of polynomial fits or higher-order functions if the offset is nonlinear [7]. The important rule to remember is that whatever curve fit is used for the baseline correction, it must be generated for and subtracted from the absorbance spectrum – not the transmittance spectrum. This mistake was made during the course of this research. Some of the impacted results were off by more than 30% but the effect varied greatly from experiment to experiment.

The spectra in Figure 94 and Figure 95 look like they may require a sloped-line-type baseline correction from 2400 cm^{-1} to 3700 cm^{-1}, but they actually serve to illustrate a word of caution about baseline correction: sometime features are broad and give the impression of a shifted baseline, but an attempted correction would result in a loss of information. In the case of the examples above, what looks like a sloped baseline is more likely the broad features of the O-H stretching region, which spans from 3000 cm^{-1} to 3800 cm^{-1} [7]. Similar local minima on both

ends of the absorbance spectrum in Figure 95 suggest that a simple baseline shift is all that is required. The result is shown in Figure 96.

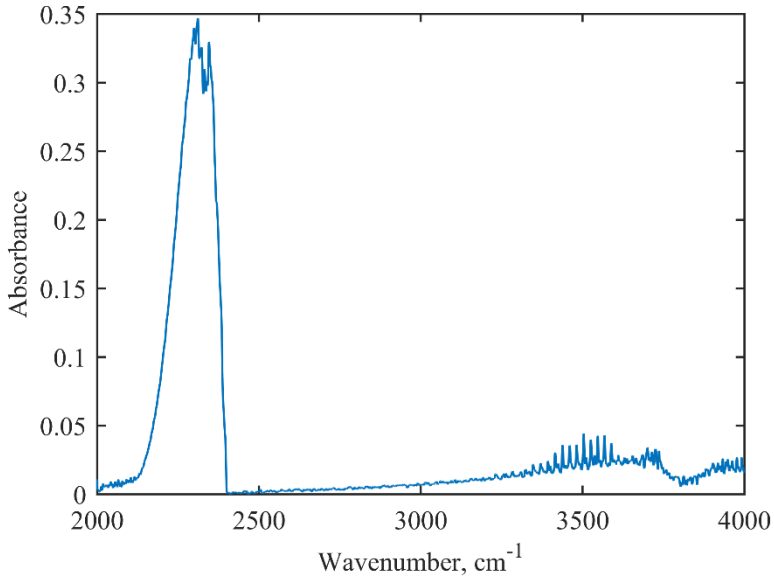

Figure 96. The baseline-corrected absorbance through the candle flame.

3.6. Spectral fitting

With crank-angle-resolved absorbance spectra and pressure traces for the associated operating conditions available it was possible to determine the temperature by matching measured absorbance features, or lines, to simulated absorbance features. Measured absorbance plots were compared to plots generated via these spectroscopic databases and the known crank-angle-resolved pressure to determine species concentration and temperature for the sample, using a spectral fitting algorithm similar to that presented by Kranendonk et al. [33].

The High Temperature (HITEMP) spectroscopic database contains line lists and line shape functions for many species, including the primary species that result from combustion in an ICE: carbon dioxide, carbon monoxide, and water [27]. CDSD-4000 is another high temperature spectroscopic database that only includes CO_2, but incorporates more empirical data than does HITEMP [34]. This study used HITEMP for H_2O analysis and CDSD for CO_2 analysis. A program written by members of the Department of Engineering Physics at the Air Force Institute of Technology was used to compare data to HITEMP simulations and determine

the curve of best fit, using the process described by Rhoby, et al. [35]. The temperature used to generate the curve of best fit was thus determined to be the temperature of the sample. Error bars were generated to indicate the goodness of fit associated with the selected temperature and resultant simulated line.

4. Proper Interpretation of Temperature Measurements

The method laid out in this chapter provided an optical path through the combustion dome of a small ICE. The scans collected with this setup therefore provided spectra that represented the spatially-averaged effect of gas absorption across the full optical path. The Beer's Law analysis conducted based on these absorbance spectra assumed that species concentration, pressure, and temperature were uniform across the entire path. In reality these parameters are subject to strong gradients, especially during combustion. The values of temperature and species concentration inferred from spectral fitting therefore fall between the minima and the maxima for their respective gradients within the engine. This study labels temperature values inferred in this way as "bulk temperature" for the combustion dome, which implies that the "hot" regions of the optical path are weighted equally with the "cold" regions in the absorption spectra. This may or may not be the case.

Regardless of these complexities, the minimum and maximum temperature values in the temperature profiles resulting from this research are representative of the true minimum and maximum bulk temperatures in the combustion dome. The profile shapes may be biased by the hot or cold regions of the optical path, but this should not prevent the profiles from being used for crank-angle-resolved thermal loss models with much greater success than what is commonly used: a temperature profile produced from the thermodynamic analysis of the cylinder gas.

IV. Results

This chapter provides a discussion of the results taken to accomplish the objectives of this research. The primary objective was to obtain crank-angle-resolved, in-cylinder, bulk gas temperature measurements in the cylinder of a Modellmotoren 3W-55i ICE. Simple experiments were conducted to prove the effectiveness of the code and experimental setup, then experiments of increasing complexity were conducted as the test capabilities were perfected. Section 1 presents the results of an experiment where FTIR was used to analyze atmosphere at room temperature, which validated the method of spectral fitting for a low-temperature case. The sorting routine explained in Chapter 5 Section 3.2 was also validated by applying a simulated engine encoder signal to this steady-state measurement. Section 2 presents results from scans through a steady, laminar flame. This experiment validated the method of spectral fitting for a high-temperature case. In a less successful validation experiment, scans were taken while motoring the engine (i.e. no combustion). The results are discussed in Appendix B.

The remaining sections present data collected while firing the engine. Section 3 compares performance data from the modified engine to data from an unmodified engine of the same model to demonstrate that the data collected in the modified engine is valid. Section 4 compares datasets compiled from varying numbers of scans to explain how the final number of scans was determined. Finally, Section 5 presents in-cylinder temperature measurements at various operating conditions.

1. Temperature of Atmosphere in Steady-State

A simple experiment was conducted to determine the temperature of atmosphere in an isolated column, or tube. The purpose of this experiment was to validate the data sorting and spectral fitting methods discussed in Chapter II.5 Section 2. The experimental setup and method replicated those used for in-cylinder measurements with one exception: the collimators at the SERB were coupled together with lens tubes instead of used to direct light through the engine. Figure 97 shows the experimental setup. The lens tubes used to isolate the column of atmosphere examined by the FTIR were modified to allow the column to be purged with

nitrogen gas. Scans collected while the lens tube was purged were used to create a background scan. The temperature was measured immediately adjacent to the lens tube with resistance temperature detectors (RTDs) while the scans were collected. 3000 scans were collected to mimic an in-cylinder scan. After the scans were collected, the crank shaft encoder signal from a previous dataset collected in-cylinder was applied to the scans of atmosphere and the same data sorting routine was executed.

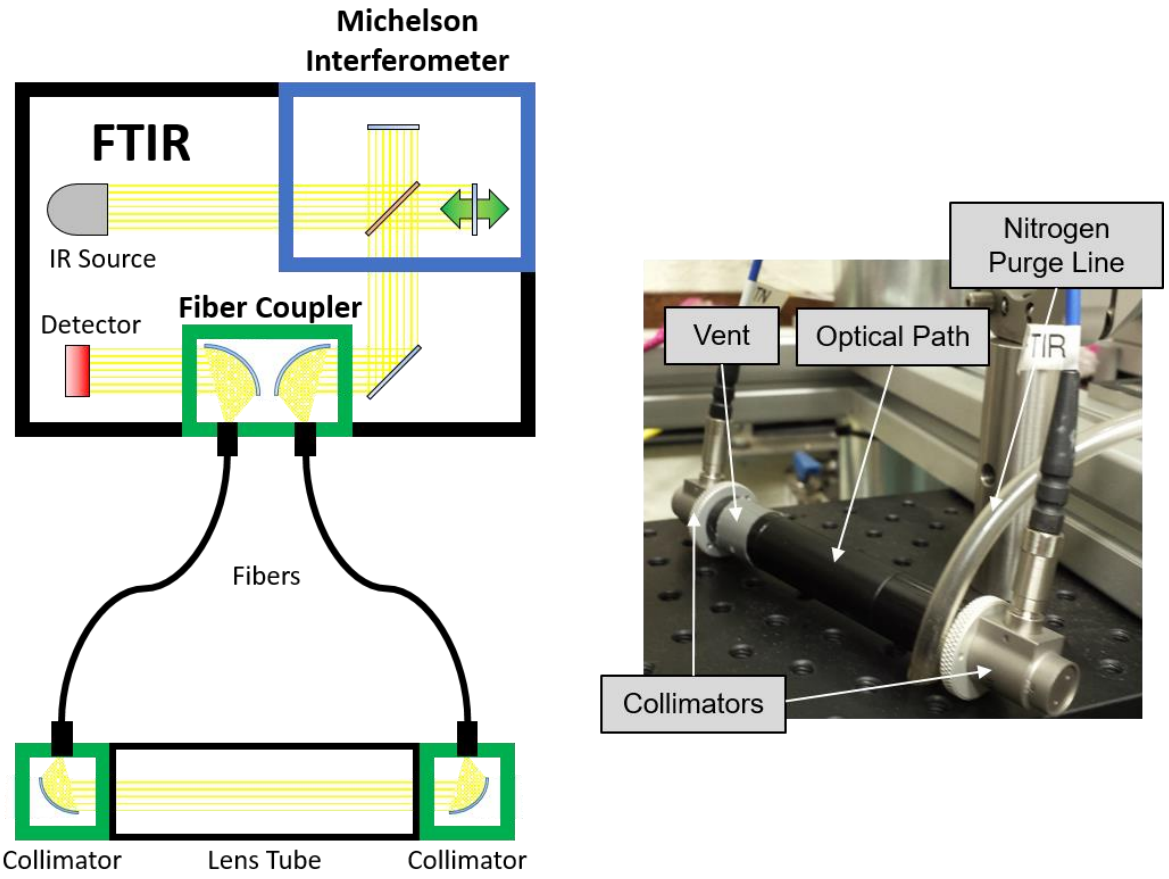

Figure 97. Experimental setup for scans of atmosphere in steady-state.

Figure 98 shows that the temperature determined by analyzing all 3000 scans as a single spectrum was 300 K. This compared well with the temperature measured by the RTDs of 297 K. The 90 temperatures determined by sorting the 3000 scans to create 90 "crank-angle-resolved" spectra had a standard deviation of 5 K and a maximum deviation of 15 K from the mean. These results demonstrate that the methods used were accurate within ± 5 %, at least for a low-temperature measurement.

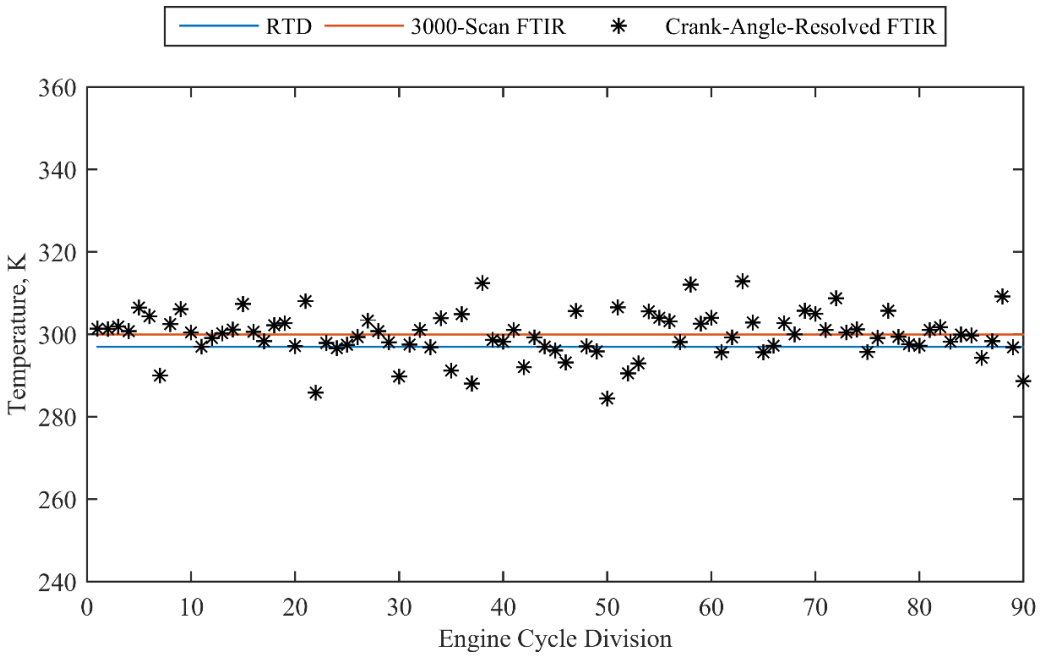

Figure 98. Comparison of temperature measured by an RTD to temperature inferred from a spectral fitting algorithm, processed as a single 3000-scan measurement and divided into 90 "crank-angle-resolved" groups.

2. Temperature of a Steady Laminar Flame

A simple experiment was conducted to determine the temperature in the hottest part of a paraffin wax candle flame, as a way to validate the method of spectral fitting described in Chapter III, Section 3.6 for an application with species and temperatures comparable to those expected in the combustion dome of an ICE. Paraffin wax candle flames can be as hot as 1,400 °C in the hottest part of the flame [36]. This temperature range corresponded well with the temperatures expected within the cylinder of the 3W-55i.

The experimental setup is shown in Figure 99. The yellow enclosure surrounding the candle prevented disturbances in the test cell from affecting the flame. The same fiber coupler, fibers, and collimators that would eventually direct a beam through an ICE were used to direct a beam through a candle flame. Scans were collected to be used for background spectra before the candle was lit. The relevant path length was assumed to be the thickness of the flame, approximately 1 cm. This implied that any changes in temperature or chemical composition to the surrounding atmosphere were negligible in comparison with the changes within the flame.

Several parts of the flame were sampled by allowing the candle to burn down on its own while scanning periodically and manually centering the flame in the beam path when necessary. The atmospheric pressure was assumed to be 1 atm. Every interferogram generated during this experiment, whether for a background spectrum or a single-beam spectrum, was created by averaging 100 individual scans.

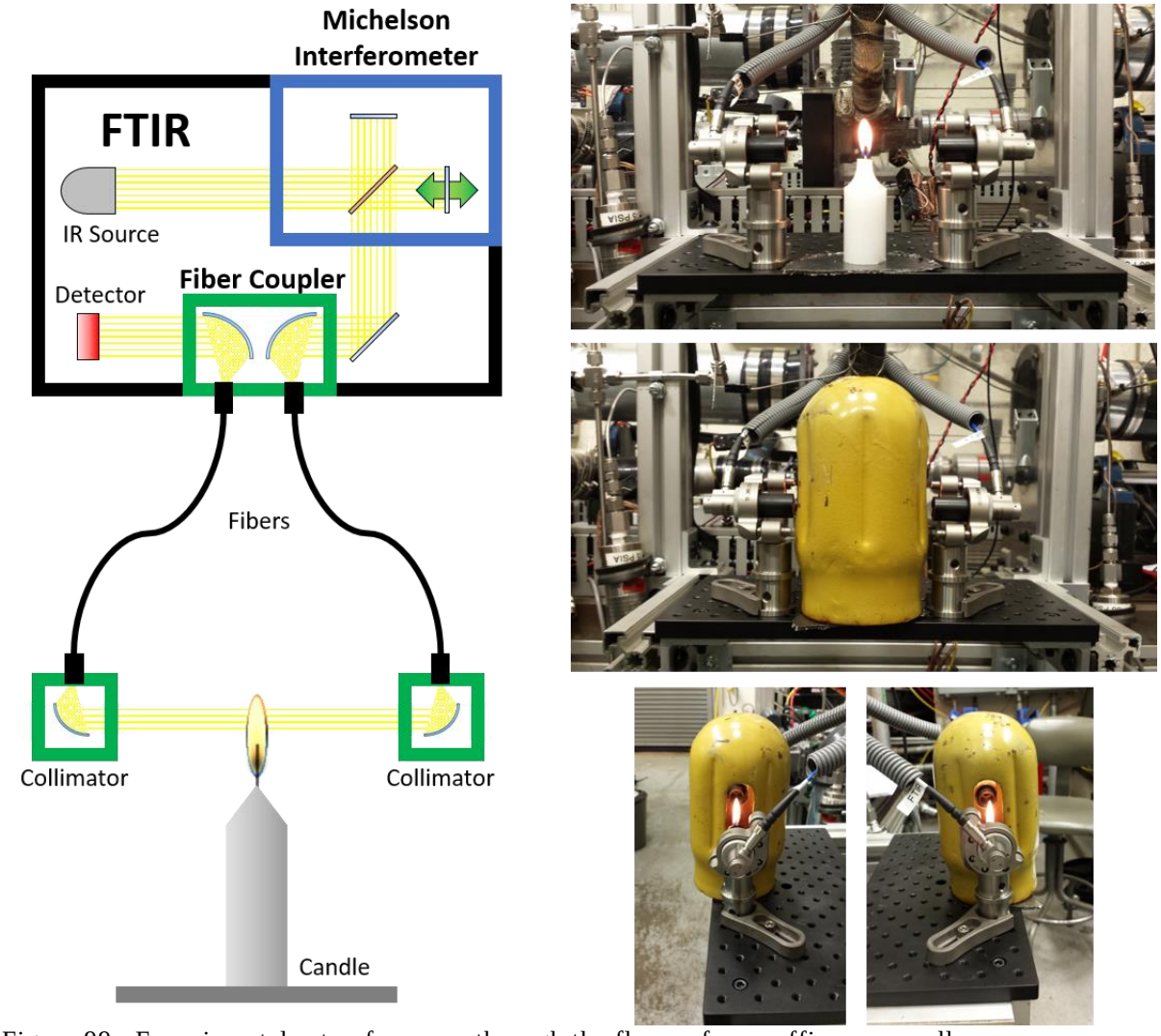

Figure 99. Experimental setup for scans through the flame of a paraffin wax candle.

The absorbance plot resulting from the scan through the hottest part of the flame is shown in Figure 100. When the spectral fitting code was run with these absorbance features the indicated temperature was 1340 °C. These results agree with the maximum temperature of 1400 °C indicated by the literature and suggest that the spectral fitting code is accurate within at

least 100 °C when analyzing gas with conditions that are more representative of the environment within an ICE, assuming the peak temperature actually present in the flame was similar to the peak temperature sited in the literature.

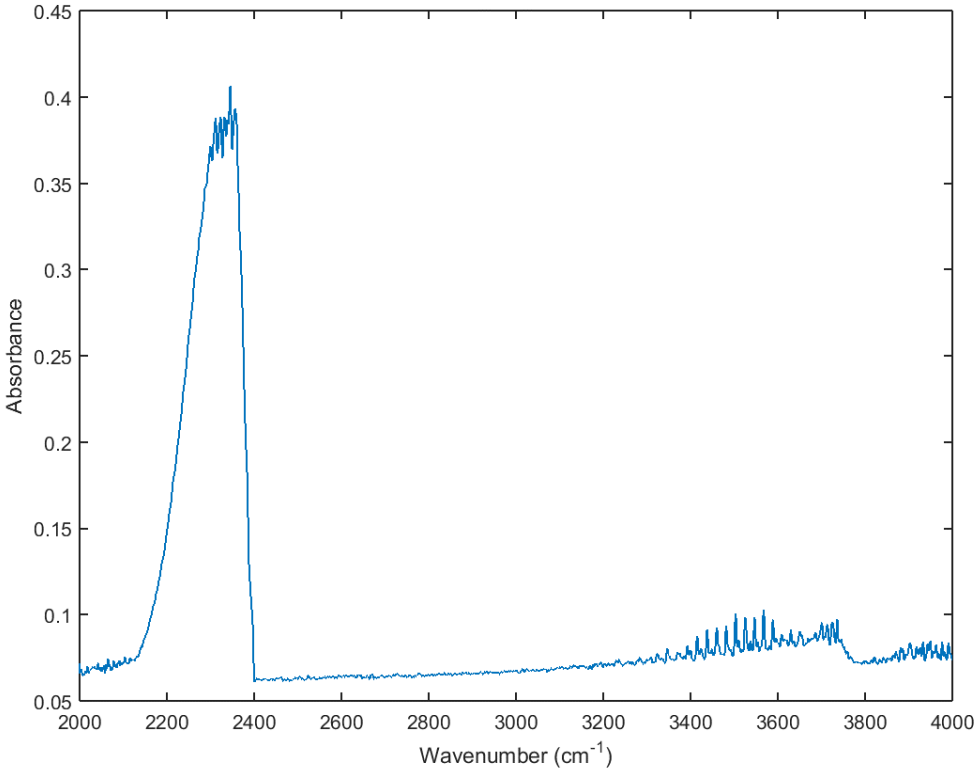

Figure 100. Absorbance plot collected in the hottest part of a paraffin wax candle flame.

3. Modified Engine Performance

Engine performance data were collected on the modified Modellmotoren 3W-55i ICE at speeds of 4000, 5000, 6000, 6500, 7000, and 7900 RPM at WOT. Each sample consisted of 400 engine cycles. These data were compared to data taken with an unmodified engine. Figure 101 compares the IMEP for a range of speeds measured on the modified engine and on an unmodified engine. The error bars represent the cycle-to-cycle coefficient of variance (CoV) of IMEP, which is also plotted independently in Figure 102. The data show tight agreement between the IMEP measured in the two engines. What differences do exist are within the range of normal engine to engine variation, or even run to run variation, which can be 5 % variation for each factor. CoV is higher in the modified engine than in the unmodified engine, but still below

2% at speeds of 7000 RPM or less. While this may be an effect of the engine modification, it is not severe enough to warrant concern.

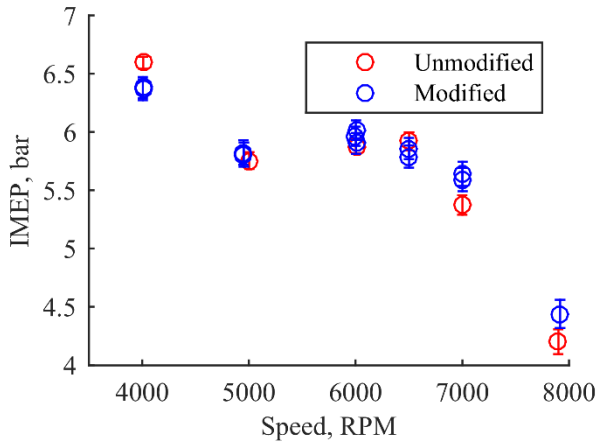

Figure 101. Comparison of IMEP between a modified and unmodified engine, with error bars generated using CoV of IMEP.

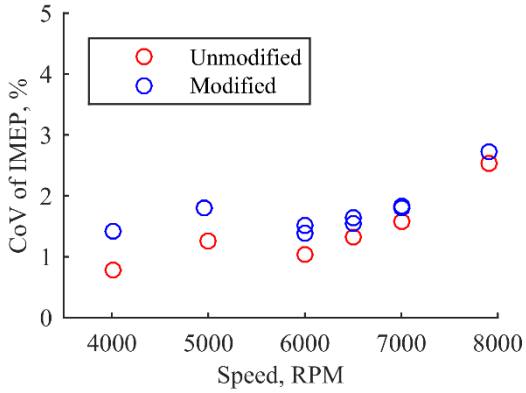

Figure 102. Comparison of CoV of IMEP between a modified and unmodified engine.

Figure 103 compares combustion phasing between the modified and unmodified engines with error bars to capture cycle-to-cycle variation in each measurement. The burned mass fraction used for these parameters was approximated using pressure and volume data, as described in Heywood and Sher [22]. CA10, CA50, and CA90 are the crank angles at which 10%, 50%, and 90% of the mass inside the cylinder, respectively, have combusted. CA50 was held between 7.5 and 8.5 °aTDC for both datasets. The data show tight agreement for CA10. CA90 was more retarded in the modified engine than in the unmodified engine, but still within statistical confidence except at 7000 RPM. This difference may also be the result of normal engine to engine or run to run variation. These data provide confidence that the modifications had a negligible impact on engine performance.

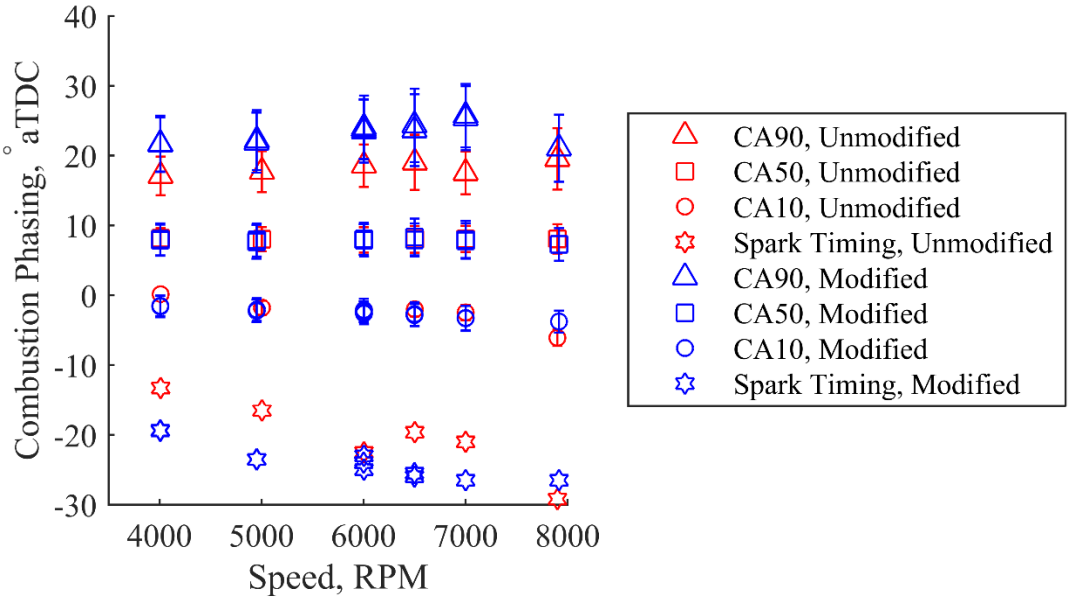

Figure 103. Comparison of combustion phasing between a modified and unmodified engine, with error bars representing cycle-to-cycle CoV of the calculated parameter.

4. Sensitivity of the Results to the Number of Scans Collected

The aforementioned experiments analyzed spectra from gas in steady state, not the dynamic environment inside the engine. It was therefore necessary to verify how many scans would be required to optimize SNR with analysis of scans collected in the cylinder of the modified engine.

Three thousand scans were obtained consecutively at a baseline operating condition: 6000 RPM, WOT. This dataset was subdivided into smaller datasets of 500 scans each. Crank-angle-resolved spectra were calculated for each 500-scan dataset. These spectra were compared to spectra calculated from the full 3000-scan dataset by calculating the root mean square (RMS) error. Similarly, the dataset was broken down into every possible combination of 1000, 1500, 2000, and 2500 consecutive scans.

The relative error in the spectrum observed for each quantity of scans is plotted in Figure 104. The error bars indicate the standard deviation of the RMS error among the various samples taken. For example, six 500-scan samples were extracted from the 3000-scan dataset. From these samples, six sets of 90 crank-angle-resolved spectra were created. The spectra looked

similar to what is shown in Figure 93. Each of these six sets of spectra were compared to spectra generated from the full 3000-scan dataset. The RMS error from all of these comparisons was 11.1% on average with a standard deviation of 1.1% among the various comparisons. This process was repeated as shown in Figure 104. From this figure it seems that the accuracy of the data could be improved by collecting more than 3000 scans. Unfortunately the time required to collect more than 3000 scans and the processing power required to sort more than 3000 scans were limiting factors for this study. It was decided to maintain 3000 scans as the standard data set and pursue other strategies to improve SNR.

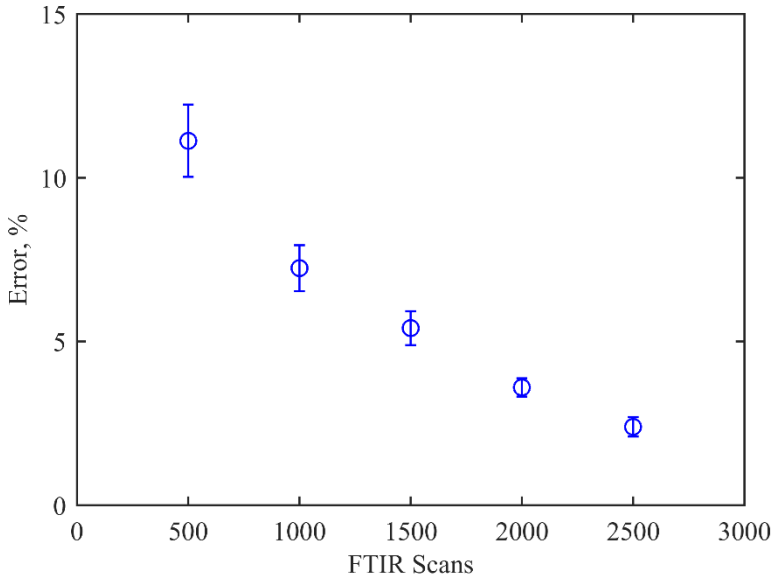

Figure 104. The error in the spectrum incurred by using less than 3000 scans

5. Crank-angle-resolved Temperature of In-Cylinder Gas at Various Operating Conditions

This section presents the results from spectra collected through the combustion chamber of the modified ICE. The experimental setup is as described in Chapter 5 Section 2.4, but the schematic is replicated in Figure 105 for convenience. The crank-angle-resolved temperature was determined at various operating conditions to determine the relative effects of piston speed, CA50 timing, and (to a limited extent) fuel octane number (ON) rating on the bulk temperature of the gas in the combustion chamber. A baseline was selected and parameters were varied independently about the baseline.

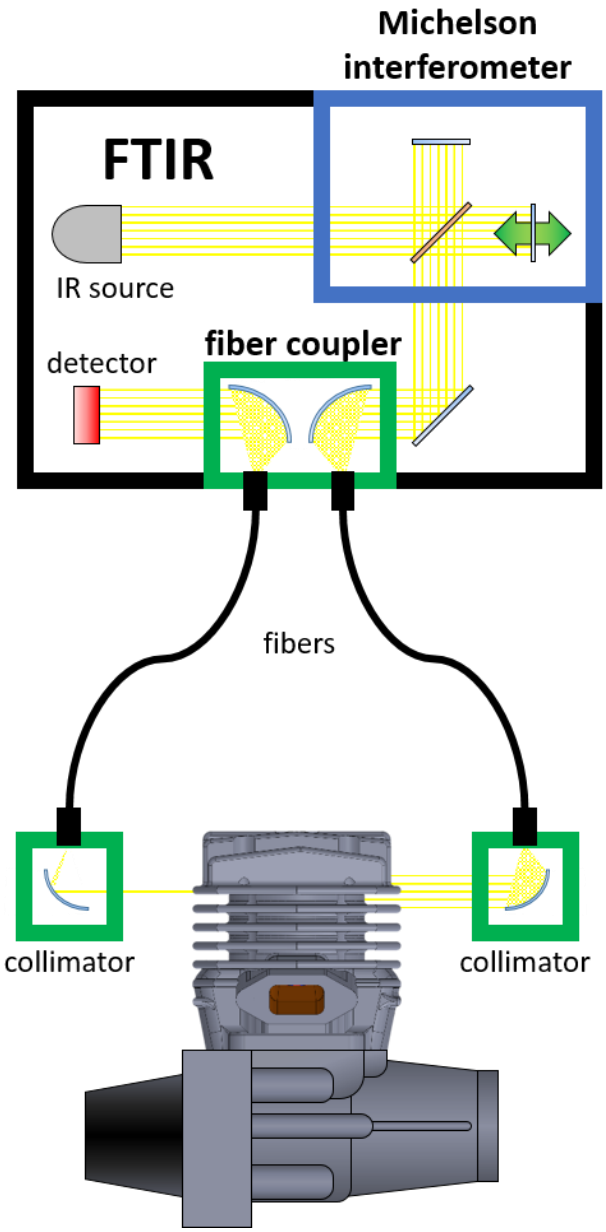

Figure 105. Optical setup for data collection in the modified engine

5.1. Baseline Engine Operating Condition

The baseline condition of 6000 RPM, WOT, with an equivalence ratio of 1.1 was selected and parameters were varied independently about the baseline. A complete description of the baseline operating parameters is provided in Table 1. The baseline operating condition was selected because a large body of data had already been collected there and engine performance was known to be stable at and around that condition. Subsequent sections will

discuss the effect on the temperature profile of changing speed and fuel octane number. The effects of other factors like throttle setting, engine head temperature, and equivalence ratio remain to be analyzed in future research. This section compares baseline measurements from several experiments spanning almost three months to highlight key lessons learned and the development of the final methodology.

Table 1. Baseline Engine Operating Conditions

Speed	6000 RPM
Throttle Setting	WOT
Equivalence Ratio (Ø)	1.1
Combustion Phasing (CA50)	8° aTDC
Head Temperature	400 K
Fuel Octane Number	98

The temperature profile in Figure 106 was the first crank-angle-resolved temperature profile generated from this research at the baseline condition collected on 25 Nov 15. All of the temperature profiles to follow have the same scale on the y-axis and follow the same conventions for the location and quantity of data points, and the meaning of error bars. Data points are spaced evenly across the cycle. Each represents four degrees of the engine cycle, thus bringing the count to 90. The error bars indicate the goodness of fit achieved by the spectral fitting code for the associated temperature values. In this dataset the trend is clearly interrupted at and following TDC and at about 150° aTDC to a lesser extent. At the time this data was collected it was not known whether these issues were caused by greater cycle-to-cycle variation in conjunction with combustion and gas exchange, or issues with the AC-coupled detector, or due to the weak signal through the engine, or some combination of the three. Less obvious but equally troubling was that the temperature trend seemed to be incorrect. The minimum temperature seemed high because the fresh charge should have entered at close to ambient

temperature, around 300 K, and the melting point of aluminum is 934 K. The maximum temperature, on the other hand, seemed low based on examples found in the literature [4, 11], which report peak temperatures as high as 3000 K.

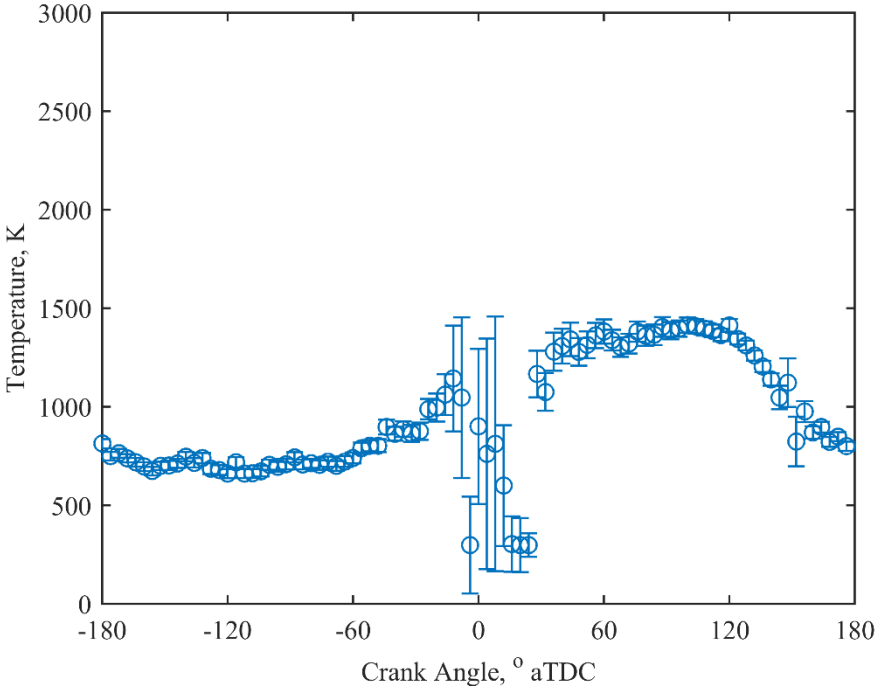

Figure 106. Temperature profile for the baseline operating condition. Data collected on 25 Nov 15.

To attempt to resolve these issues, the data was further investigated. Much insight was gained by looking at the raw interferograms that were used to generate this crank-angle-resolved temperature profile. The stack plot in Figure 107 corresponds to the temperature profile in Figure 106 and serves to condense and illuminate the features of the raw interferograms that are significant for in-cylinder measurements. The construction of the stack plot is explained in Chapter III, Methodology, in Section 3.1. The crank-angle-dependent SNR can be estimated by taking the ratio of the peak-to-peak magnitude of the centerburst to twice the amplitude of the baseline noise. Cyclical patterns of loss in SNR can be identified and diagnosed based on the stack plot. A decrease in global SNR from one day to the next would be an indication that, for whatever reason, the IR beam is not being transmitted through the engine as well as before, and the setup should be checked for poor alignment, soot on windows, ineffective nitrogen purge,

etc. A decrease in global signal with no decrease in SNR (i.e. the emission signal and noise threshold decrease proportionally to the IR signal) would indicate poor alignment at the "catch" side of the engine or at the detector. This would be less of an issue because the preamplifier provided ready control of the signal gain prior to digitization and SNR does not suffer, but the alignment issues could be addressed if desired. The data can also be checked for poor distribution across all crank angles by looking for large gaps between centerbursts. If this were the case, the problem could be solved by changing the speed of either the engine or the mirror in the interferometer.

In the dataset in Figure 107 shows a gap in the data between 30° and 40° aTDC. This gap closes in later scans – the stack plot only represents about 4% of the data collected. The SNR tapers off slightly when approaching TDC, drops off severely at about TDC, and gradually builds again after TDC. The gradual, cyclic rise and fall in SNR is most likely due to the changes in pressure within the cylinder: the greater the pressure, the greater the absorption. The rapid drop in SNR immediately after TDC manifests itself in the stack plot as a "neck" at approximately 15° aTDC. It is difficult to see in this particular stack plot because the residual emission signal overpowers the IR signal in that region, but it is more prominent in stack plots from later datasets. The neck may be caused by one of many things: engine vibration at TDC may have caused the windows to shift out of alignment with the beam, which was isolated from the vibrating components on the bench; the punctuated gradients in thermodynamic properties throughout the combustion chamber that are caused by the propagation of the flame front may have caused the beam to refract in the cylinder to the point where alignment suffered; the combustion products may have been heavy-laden with soot, blocking signal through the combustion chamber.

It is the author's current opinion that the neck was caused by alignment issues. Figure 108 through Figure 110 show the stack plots from the other two datasets at the baseline operating condition, and one that was taken while running 20 ON fuel at what was otherwise the baseline operating condition. Notice that the neck varies in prominence from one run to the next. The

experiment with the most prominent neck occurred on 2 Feb 16, as shown in Figure 110. It was while looking at this stack plot that the neck was recognized for the first time. A thorough investigation was made into the cause because a dataset that had very little neck was collected just five days earlier, 28 Jan 16, as shown in Figure 109. The optical probes were inspected and found to be coated with a translucent film of oil on the outer surface. This coat of oil was either residue left over from the gluing process or a slow leak of motor oil from the combustion chamber caused by a small gap in the glue between the window and the bolt. Either way, it is hypothesized that the irregular interface at the surface of the oil made the signal strength hyper-sensitive to engine vibration.

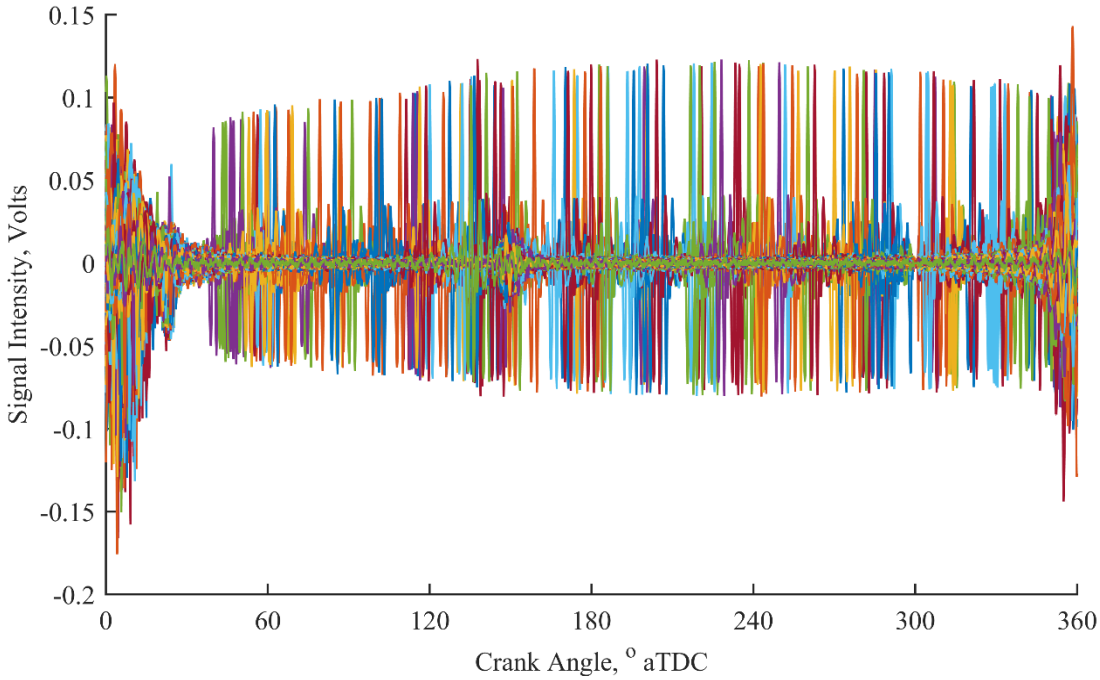

Figure 107. Stack plot for the baseline operating condition. Data collected on 25 Nov 15.

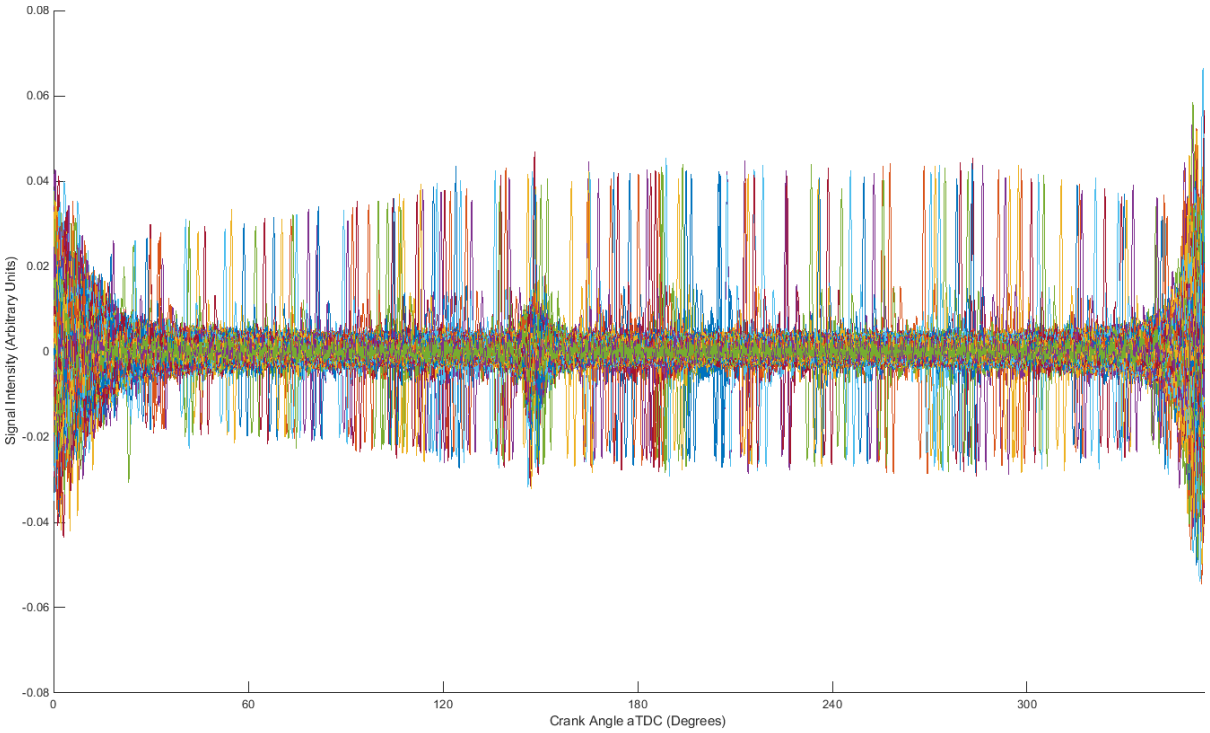

Figure 108. Stack plot for the baseline operating condition. Data collected on 8 Dec 15.

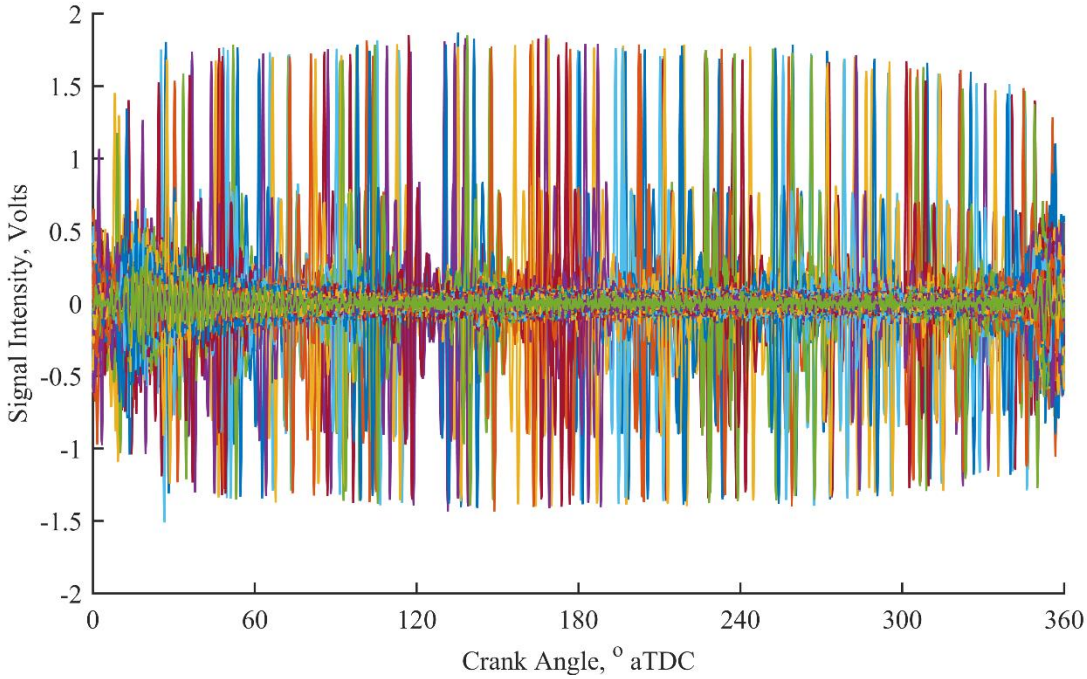

Figure 109. Stack plot for an experiment with 20 ON fuel, but otherwise the baseline operating condition. Data collected on 28 Jan 16.

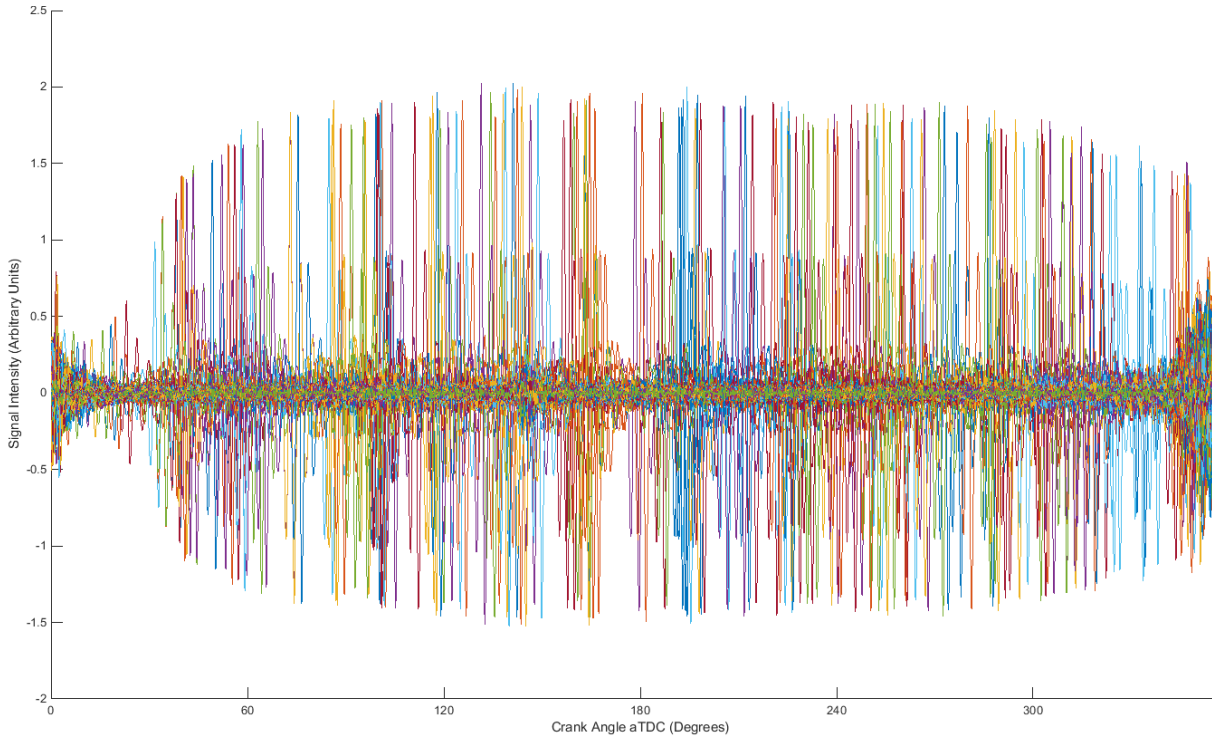

Figure 110. Stack plot for the baseline operating condition. Data collected on 2 Feb 16.

Figure 111 and Figure 112 re-visit the dataset collected on 25 Nov 15. They show crank-angle-resolved interferograms and the resulting single-beam spectra from two locations in the engine cycle. Figure 111 is the data for 200° aTDC. The single-beam spectrum shows strong absorption by CO_2 from approximately 2300 to 2400 cm^{-1} and by hydrocarbons from approximately 2750 to 3000 cm^{-1}. There are also small absorption features by H_2O from 3000 to 4000 cm^{-1} but these are almost indistinguishable from the baseline noise. Figure 112 serves to illustrate how much impact the neck region in the engine cycle has on the crank-angle-resolved results. The interferogram and spectrum correspond to TDC. The interferogram has a noticeably smaller peak-to-peak amplitude than the 200° aTDC case and the baseline noise level is higher. When the Fourier transform is taken the spectrum is found to be almost pure noise. Quantitative analysis was possible with the spectrum in Figure 111, but not the spectrum in Figure 112, and these are just two examples of ninety from the engine cycle.

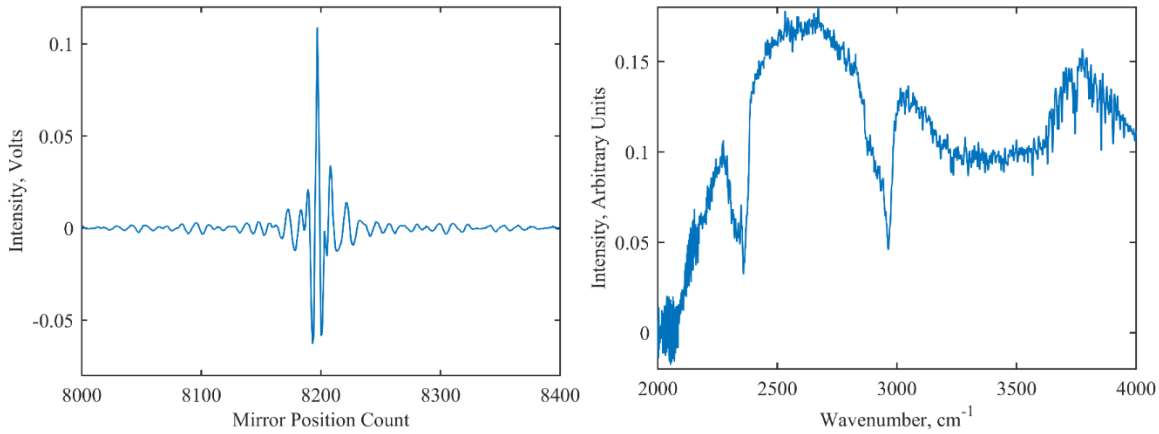

Figure 111. The crank-angle-resolved interferogram at 200° aTDC (left) and the resulting single-beam interferogram (right). The x-axis of the interferogram is limited to show the detail of the centerburst. Data collected on 25 Nov 15.

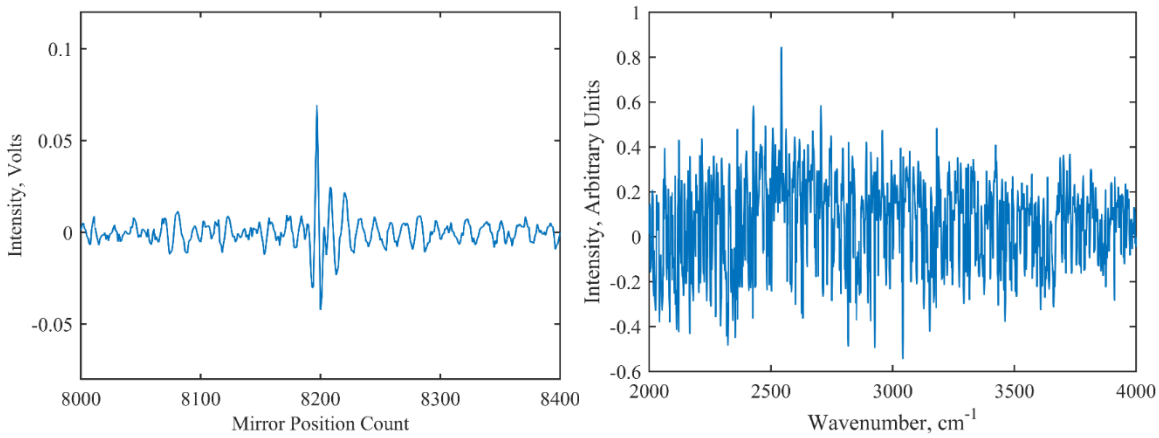

Figure 112. The crank-angle-resolved interferogram at TDC (left) and the resulting interferogram (right). The x-axis of the interferogram is limited to show the detail of the centerburst. Data collected on 25 Nov 15.

Figure 113 is two graphical representations of the single-beam spectrum "waterfall" plot, a 3D (top) and 2D (bottom) version. These provide a way to view all of the crank-angle-resolved, single-beam spectra for the baseline condition in one image. There is much to be said about the waterfall plots, but for the moment they shall be discussed in the context of what was just said about Figure 111 and Figure 112. Note the width and intensity of the noise bands at TDC and 150° aTDC. All of the changes to the experimental method moving forward after 25 Nov 15 were focused on improving SNR across the entire engine cycle and reducing portion of the engine cycle affected by emission signal. This was achieved with three general strategies executed simultaneously: sample the engine for longer periods of time, force more IR light

through the engine, and filter out more of the emission noise before digitization of the interferogram. The following discussion provides the specific actions taken to implement these strategies.

The SNR of an interferogram is proportional to the amount of time taken to collect the sample and to the number of samples taken [23]. This experimental setup placed an emphasis on fast mirror speeds for data processing reasons, so the decrease in sampling time was compensated for by increasing the number of samples collected. The dataset taken on 25 Nov 15 consisted of 1500 scans. That number was doubled for all following experiments. 3000 scans took approximately 24 minutes to collect, which became a challenge for planning experiments when data was desired at 11 operating conditions. 3000 scans was therefore determined to be a practical limit until other strategies for improving the data were pursued.

Several actions were taken to improve the IR signal through the engine. All of the fiber terminals were inspected and polished to ensure peak performance. The Harrick FiberMate2 that was originally used to route the IR beam from the FTIR test cell to the fibers and back was eventually exchanged for stand-alone mirrors mounted to an optical breadboard because the new setup provided greater control over the position of the fiber terminal with respect to the focal point of the off-axis parabolic mirror. This change improved signal through the engine by 40%, but it was not implemented until the dataset taken on 2 Feb 16.

The greatest emphasis was placed on the optical probes. The original design did not allow the probes to seat flush with the wall of the combustion chamber. The slight recess made the windows cooler than the rest of the surfaces in the combustion chamber and therefore a collection point for soot and oil. The recesses themselves tended to clog up with soot over time. The problem was solved by extending the threads all the way through the cylinder wall and designing longer probes so they could seat flush. After these modifications the only signal degradation problems that remained were those caused by coking that slowly built up throughout the entire combustion chamber and had to be cleaned out periodically.

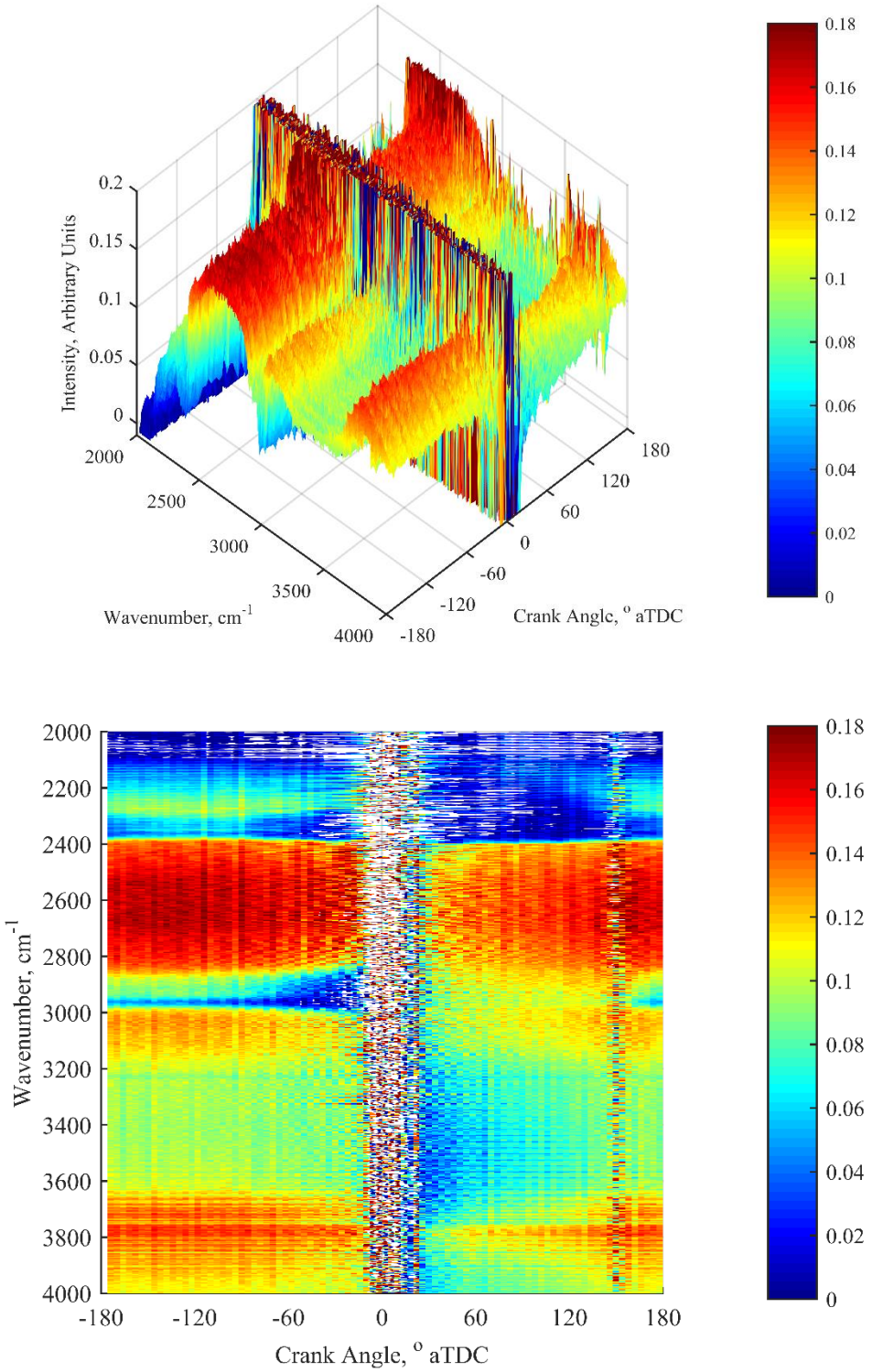

Figure 113. Waterfall plots for the baseline operating condition. The upper plot is a 3D representation of the lower plot with the identical color scale. The intense spikes at TDC and ~ 150° aTDC are cut off to enlarge the features where SNR was favorable. Data collected on 25 Nov 15.

Another problem with the optical probes was the diameter of the windows with respect to the diameter of the beam. As was explained in Chapter III, Methodology, 2.3.2, roughly 70% of the signal available to send through the engine was lost due (for the most part) to the diameter of the windows. This issue was made worse by the tendency of the sapphire rods to break loose from the threaded casing. The only options available were to reduce the diameter of the hole on the outside-half of the bolts such that the sapphire rods could not back out of the assembly, or add sapphire windows in lens tubes between the collimators and the engine as protection from projectile sapphire rods. Both of these options resulted in reduction to signal through the engine, but after destroying expensive optical components on multiple occasions it became clear that the protective measures were necessary.

The final strategy was implemented by bringing in a new MCT detector. One of the primary concerns with the datasets from 25 Nov 15 and 8 Dec 15 was the shape of the emission signal observed via the interferogram. The circuitry built into the MCT detector performed a broad bandpass filter, amplification, and active baseline correction that provided very little control to the user. The signal from the original MCT detector could have been passed through a preamplifier to improve control of filtering and amplification, but the issue of baseline correction could not be solved in this way. It was hypothesized that the auto baseline correction was over-compensating for the strong emission signal at TDC and causing the loss of IR signal at that crank angle position. For the static samples typically examined by an FTIR this would not be an issue so the electronics were not designed for an application with cyclical signal spikes due to emission. The new detector did not automatically adjust the baseline of the interferogram. Its output signal was passed through a stand-alone preamplifier prior to digitization. This setup provided much more control over how the interferogram was filtered and amplified.

Figure 114 through Figure 116 provide a chronology of the baseline datasets taken after 25 Nov 15. Figure 114 shows data collected on 8 Dec 15. The primary difference between this dataset and the one collected on 25 Nov 15 is that the number of scans collected was doubled from 1500 to 3000. The SNR of the crank-angle-resolved spectra was actually not improved

from what was seen on 25 Nov 15, probably because a buildup of soot in front of the optical probes negated any gains seen from the additional scans. Comparing the stack plots for the two datasets, Figure 107 and Figure 108, it is readily apparent that the IR signal was not transmitted as well on 8 Dec 15 as it was on 25 Nov 15. The issue was not discovered until much later because the stack plots were not yet being used to perform a quality check on the experimental setup prior to collecting data. Consequently the true physical reason for the loss in signal was never determined.

Figure 115 shows data collected with 20 ON fuel, but otherwise at the baseline operating condition, on 28 Jan 16. Flush-mount optical probes were used for the first time with this dataset. The optical probes used at the time did not have a lip to retain the sapphire windows in an attempt to improve signal through the engine. While the setup succeeded in improving SNR, the risk of a sapphire rod being ejected was realized after about 940 scans had been collected. Despite being a partial dataset, and not even a true baseline condition, it is worth showing because it was the best global SNR achieved of any of the data up until that date and the SNR neck that plagued other experimental setups, before and after, was not present on that day (see Figure 109). Another change that helped improve SNR for this dataset was the installation of the new detector.

Figure 116 shows the data collected on 2 Feb 16. This data has the best SNR local to most crank angles that was achieved during this research. The exception is the neck at 15° aTDC that looks like a thick blue vertical column on the 2D waterfall plot and is clearly seen on the stack plot (Figure 110). The experimental setup differed from 28 Jan 15 in that sapphire windows were installed to protect the collimators at the engine, some unnecessary windows were removed from the FTIR test cell walls, and the fiber coupler was adjusted to improve signal transmission to the fibers.

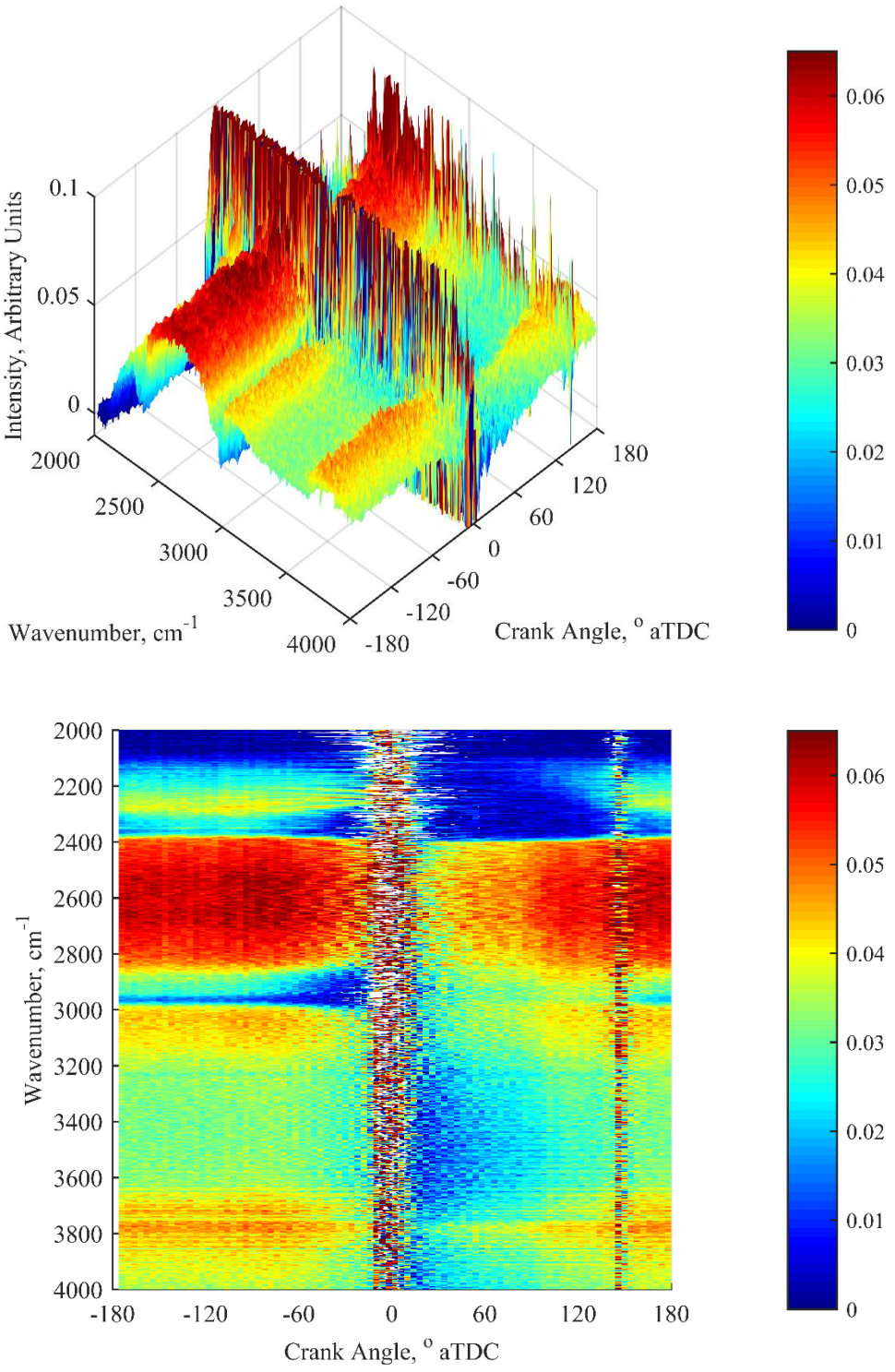

Figure 114. Waterfall plots for the baseline operating condition. The upper plot is a 3D representation of the lower plot with the identical color scale. The intense spikes at TDC and ~ 150° aTDC are cut off to enlarge the features where SNR was favorable. Data collected on 8 Dec 15.

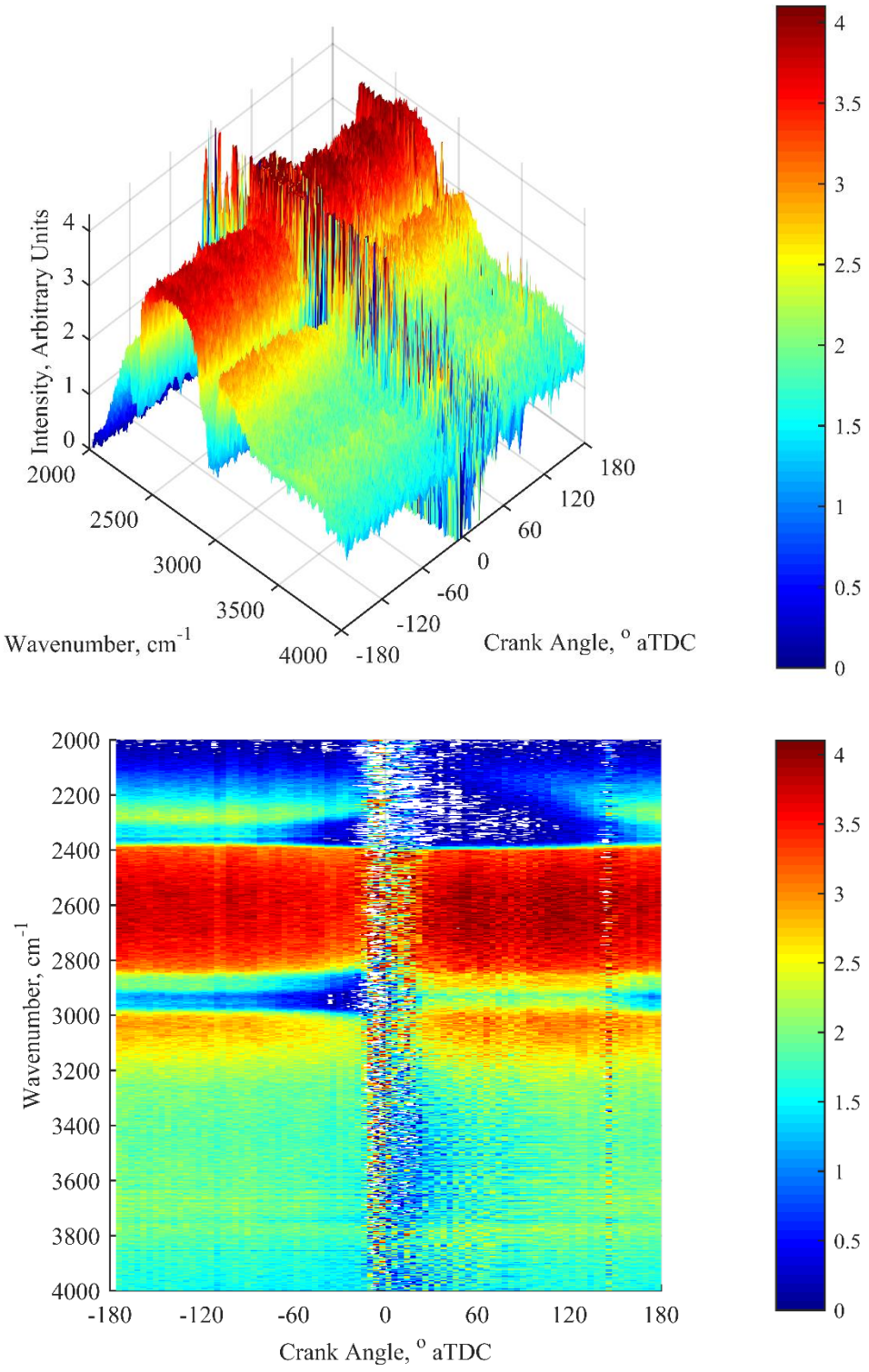

Figure 115. Waterfall plots for and experiment conducted with 20 ON fuel, but otherwise the baseline operating condition. The intense spikes at TDC and ~ 150° aTDC are cut off to enlarge the features where SNR was favorable. Data collected on 28 Jan 16.

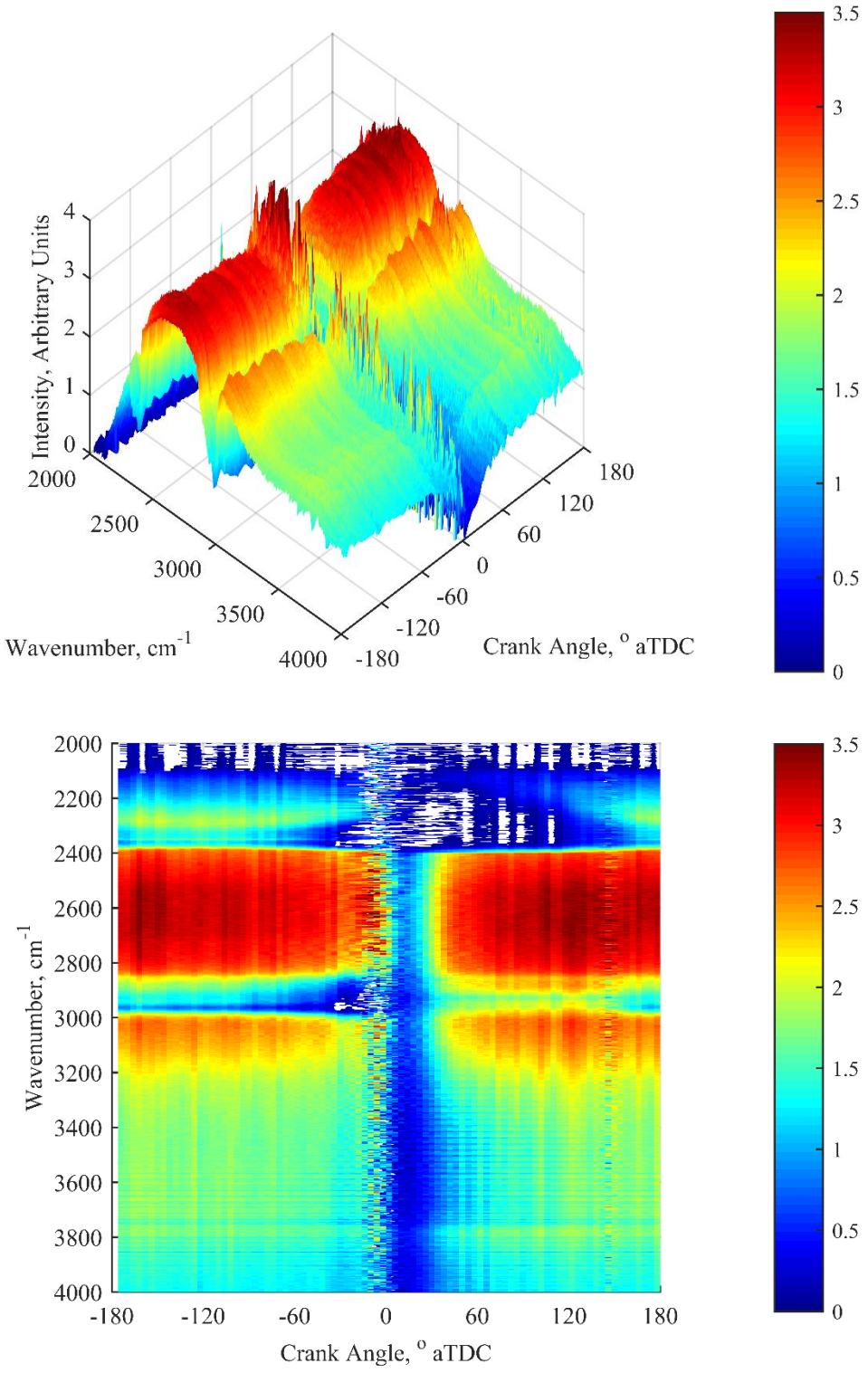

Figure 116. Waterfall plots for the baseline operating condition. The intense spikes at TDC and ~ 150° aTDC are cut off to enlarge the features where SNR was favorable. Data collected on 2 Feb 16.

Some common trends can be seen in the data in Figure 113 through Figure 116. Prior to combustion (to the left of TDC in the 2D waterfall plots) the in-cylinder gas is primarily the air-fuel mixture, with some residual exhaust gases. The CO_2 in this mixture absorbs moderately between 2300 and 2400 cm^{-1}. The hydrocarbons in the fuel absorb strongly between 2850 and 3000 cm^{-1}. The piston begins compressing the mixture after the exhaust port closes at 103° bTDC. Absorption by both the hydrocarbons and CO_2 increase as the pressure and temperature rise in the cylinder. After combustion the hydrocarbons are gone for the most part, so absorption is greatly reduced between 2850 and 3000 cm^{-1}. CO_2, on the other hand, has become more concentrated and therefore absorbs even more. Deep blue and white on the waterfall plots indicate that no light was detected at the associated wavenumbers. CO_2 absorption is therefore saturated from about 40° bTDC to 100° aTDC. This has implications for spectral fitting that will be discussed later. One of the products of combustion is H_2O, which absorbs from 3000 to 4000 cm^{-1}. Immediately after combustion there is strong absorption due to H_2O, but it is greatly reduced as the gas expands until there are only small absorption features between 3500 and 4000 cm^{-1}. The narrow, weak noise band at approximately 150° aTDC is probably caused by high cycle-to-cycle variation associated with gas exchange. The gas exchange would be expected to cause a dramatic decrease in absorption due to CO_2 and increase in absorption due to hydrocarbons in conjunction with the CO_2-rich exhaust being replaced by hydrocarbon-rich air-fuel mixture. These changes are observed in correlation with the noise band, even though the exhaust port opened at 103° aTDC and the scavenge ports were all open by 118° aTDC. There must therefore be a 30 crank-angle-degree delay between the opening of the scavenging ports and the exchange of exhaust for air-fuel mixture in the combustion dome, where the line of sight for the optical probes is located. The length of the delay in crank angle degrees was observed to be a function of engine speed, and this is discussed in Section 5.2.

Figure 117 gives a comparison between the first baseline condition data collected on 25 Nov 15 (top) and the last baseline condition data collected on 2 Feb 16 (bottom). The first thing to notice is the background spectra to the left. The one from 25 Nov 15 has strong absorption

features due to the atmospheric gas in the engine cylinder and the buildup of oil in the cavities for the recessed optical probes. These features were divided out of the crank-angle-resolved single-beam spectra collected that day but, as can be seen by comparison to the example spectrum to the right, the features in the background were roughly of the same size as the features in the sample. This means that when the ratio was taken the remaining features were weak and distorted, which led to questionable results. The background scan from 2 Feb 16, on the other hand, was taken through the engine cylinder purged with nitrogen gas, which does not absorb in the mid-IR. Consequently, the absorption features are very weak and probably due to absorption in other parts of the experimental setup that should be eliminated from the results anyway. So when the ratio is taken with the crank-angle-resolved, single-beam spectra, strong and undistorted features remain. The other thing to note from these examples is the difference in baseline noise between the crank-angle-resolved, single-beam spectrum from 25 Nov 15 on the top right, and the one from 2 Feb 16 on the bottom right. The improvement in SNR caused many of the weaker H_2O absorption lines to finally stand out from the noise. This led to greater flexibility when spectral fitting and greater confidence in the final results.

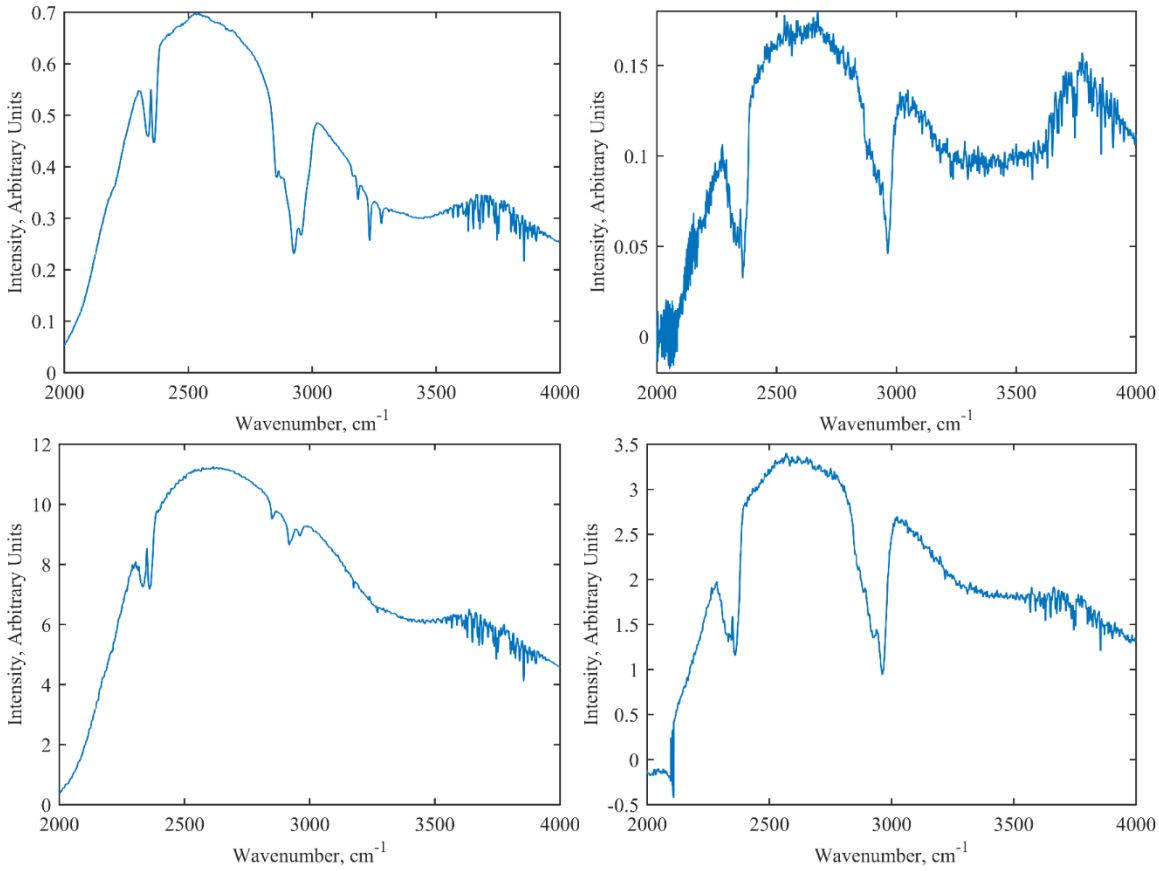

Figure 117. Comparison of single-beam spectra from data collected on 25 Nov 15 (top) and 2 Feb 16 (bottom). The background spectra (left) are side-by-side with single-beam spectra for 200° aTDC.

Two examples of crank-angle-resolved absorbance spectra collected on 2 Feb 16 are shown in Figure 118, side-by-side with their parent single-beam spectra. The single-beam spectrum in the top-left quadrant is the same one that was shown in the bottom-right quadrant of Figure 117, from 200° aTDC. Notice that the corresponding absorbance spectrum in the top-right quadrant of Figure 118 is devoid of H_2O absorption lines, which would typically be seen between 3000 and 4000 cm^{-1}. CO_2 absorption, on the other hand, causes a prominent feature between 2300 and 2400 cm^{-1}. The single-beam spectrum in the bottom-left quadrant is from another part of the engine cycle, at 56° aTDC. At this crank angle, CO_2 absorption is saturated (as indicated by the lack of signal from approximately 2200 to 2400 cm^{-1}) but H_2O absorption lines are much stronger. In the corresponding absorbance spectrum the feature due to CO_2 absorption is distorted so matching CO_2 absorption lines would lead to bad results. Luckily the

H_2O absorption lines rise above the noise. The CO_2 and H_2O absorption lines tended to balance each other in this way throughout the engine cycle except in some small transition regions, which are evident in the associated temperature profiles. For this reason spectral fitting depended on different absorption features throughout the engine cycle: many matched lines to both CO_2 and H_2O simultaneously, but some relied on one species independently of the other to avoid errors caused by saturated features or by features that fell below the noise threshold.

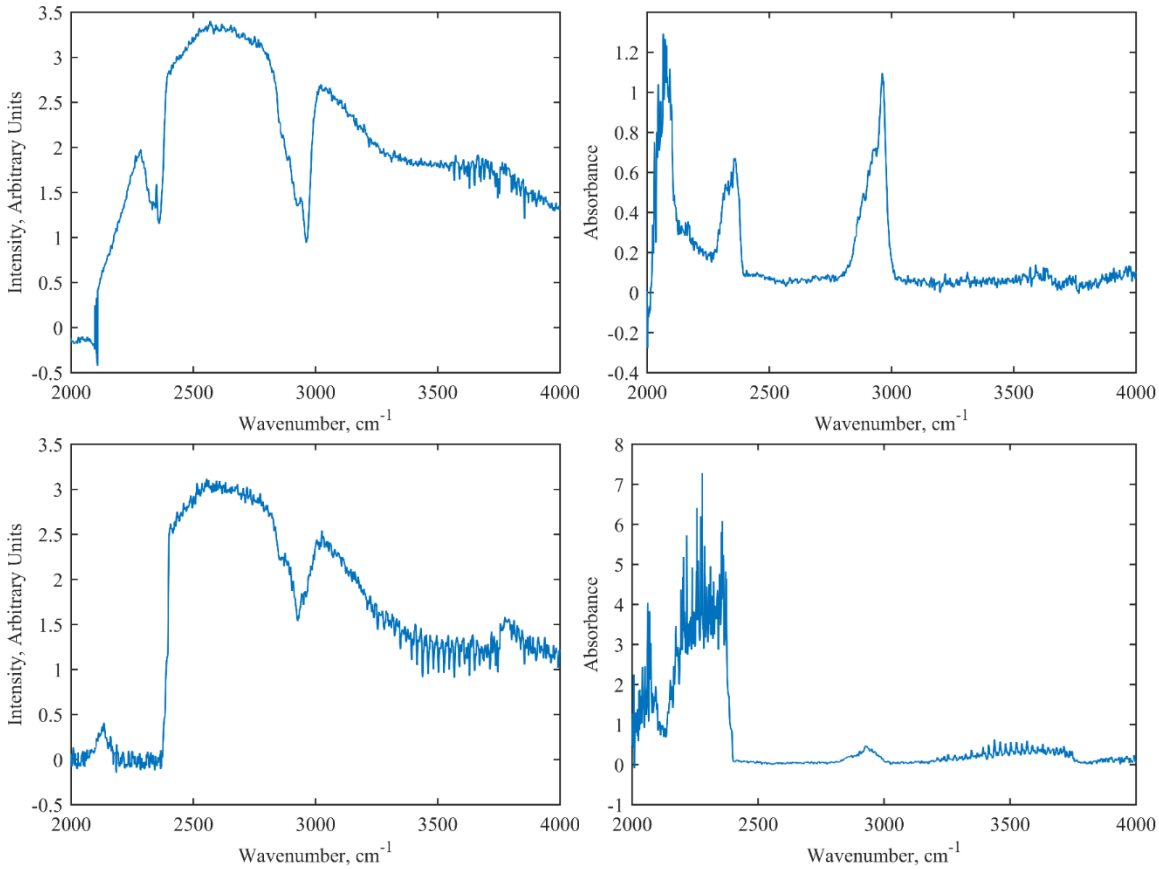

Figure 118. Data collected on 2 Feb 16. Crank-angle-resolved single-beam spectra (left) and absorbance plots (right) for 200° aTDC (top) and 56° aTDC (bottom).

Figure 119 shows the results of attempting spectral fitting with each of these three strategies across the entire engine cycle. Again, the error bars in the temperature profile plots indicate the goodness of fit achieved by the spectral fitting code. The final temperature profile was determined by making a composite of values from each of the three cases. The correct values were chosen for the most part by comparing the goodness of fit for each of the three cases, but decisions had to be made in some regions based on knowledge of the absorbance

spectra, as illustrated by Figure 118. The transition regions discussed in the last paragraph occur immediately after combustion and at approximately 70° aTDC. The error in these transition regions may be as much as 400 K, whereas from TDC to 70° aTDC the error is about 200 K, and about 50 K during gas exchange.

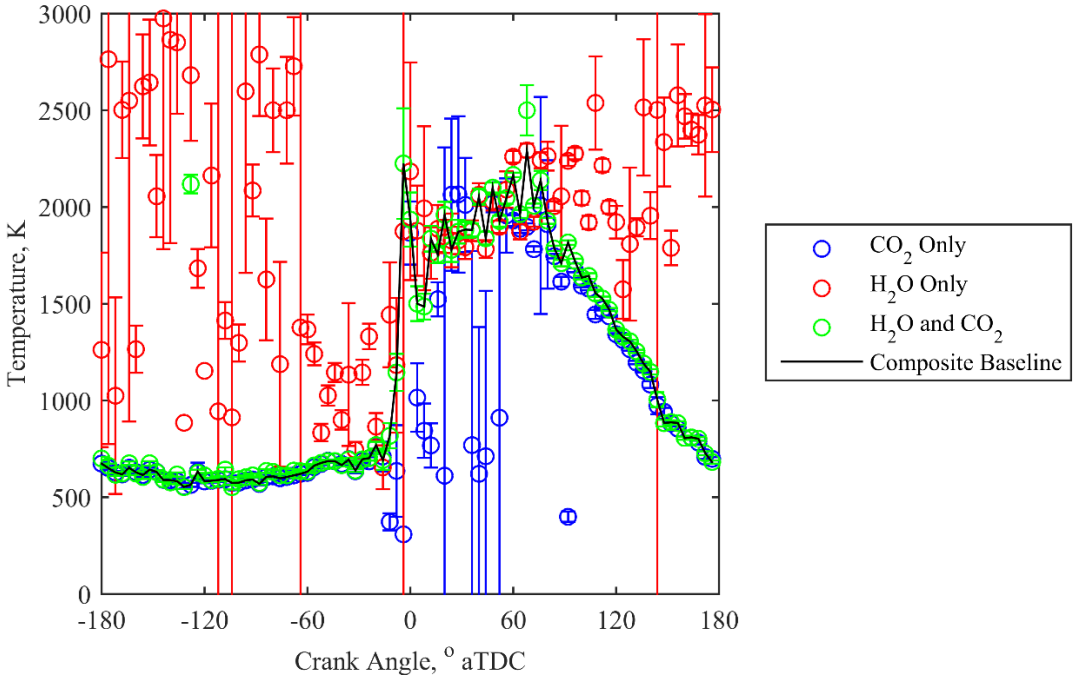

Figure 119. Temperature profile for the baseline condition using data collected on 2 Feb 16. The legend indicates the strategy used to match lines for each data set. The composite baseline indicates which points were selected from each of the three data sets for the final temperature profile.

The discussion has finally come full circle. The temperature profile that was first presented in Figure 106 is produced again in Figure 120, this time with temperature profiles based on data from 8 Dec 15 and 2 Feb 16 for comparison. The balance between CO_2 and H_2O features was not possible with the dataset from 8 Dec 15 because the SNR was so low that none of the H_2O features exceeded the noise. It was postulated before that the dataset from 25 Nov 15 reported the minimum temperature high and the maximum temperature low, and these could be corrected by re-running the spectral fitting code with an appropriate baseline correction methodology. The data from the other two experiments seem to support this theory.

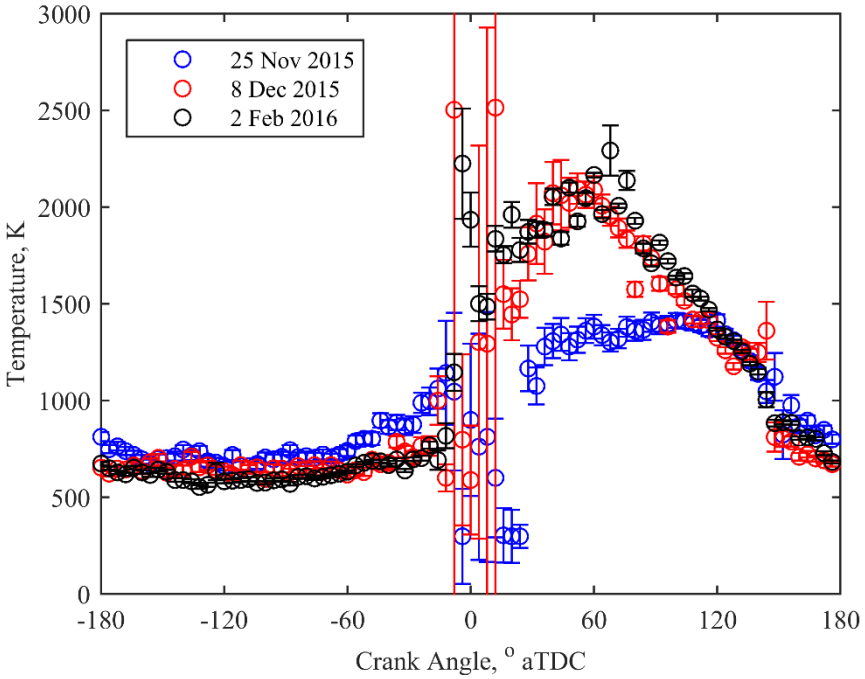

Figure 120. Comparison of temperature profiles for the baseline condition from all three datasets.

5.2. Effect of Variable Speed

The datasets collected on 8 Dec 15 were a baseline at 6000 RPM, and two other operating conditions with speeds of 4300 RPM and 7500 RPM. Had the operating condition at 4500 RPM not been unstable the lower-speed data would have been collected there instead of 4300 RPM. For the reasons explained in Section 5.1 the SNR was not sufficient to determine the temperature with confidence in certain regions of the engine cycle, especially when there is high cycle-to-cycle variation at combustion and gas exchange. These data provide some insight into the effect of engine speed on the crank-angle-resolved temperature trace but mostly serve to illustrate how the combination insufficient SNR and saturation of the CO_2 absorption band impact the results.

Figure 121 shows the crank-angle-resolved temperature traces for all three operating speeds. Overall, speed seems to have little impact on the temperature profile because the agreement between the three cases is very tight. While little can be said about the region of the engine cycle immediately before and after combustion, temperature does seem to reach a local maximum between 20° and 60° aTDC, and the data suggest that the higher the engine speed, the

later the peak temperature. Similarly, the higher the engine speed, the later the minimum temperature after gas exchange. The decreased SNR associated with gas exchange causes the uncertainty at the effected crank angles to increase and it can be seen in this figure that the higher the speed, the later this region of uncertainty occurs. The effects of gas exchange are consequently seen at 136° aTDC for 4300 RPM, at 144° aTDC for 6000 RPM, and at 152° aTDC for 7500 RPM. This make sense because it takes time for the gas dynamics at the ports to effect the gas in the combustion dome where the line of sight of the optical probes is. The amount of time required for the effect to propagate into the combustion dome should be relatively constant, so as the engine speed is increased the effect will be observed later in the cycle.

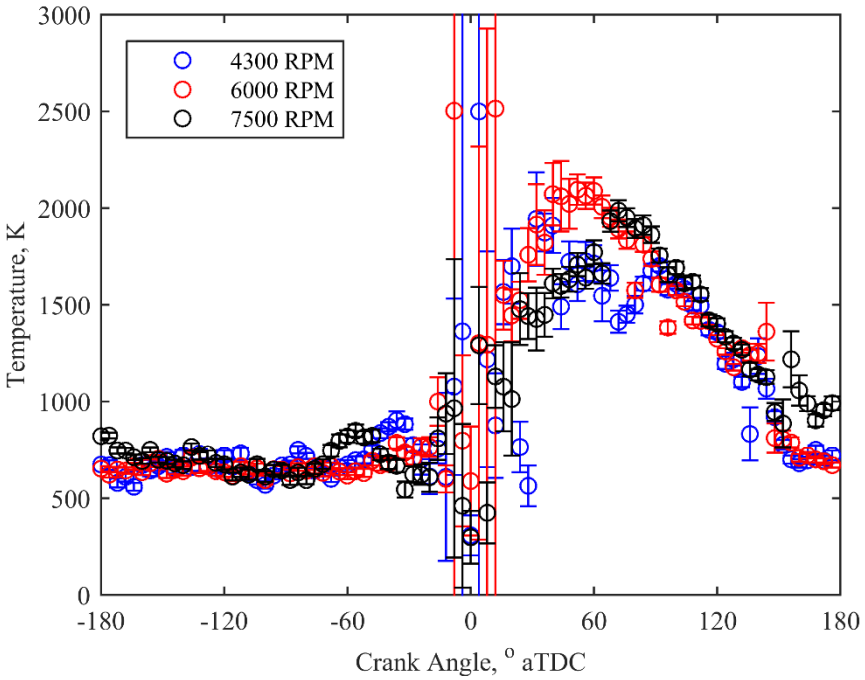

Figure 121. Comparison of temperature profiles when operating speed is varied.

Figure 122 shows the qualitative absorption trends associated with each operating condition and species, as functions of crank angle. These trends were generated by calculating the area under the curve of the absorbance spectrum with the following ranges for each species: 2260 to 2400 cm^{-1} for CO_2, 2840 to 3000 cm^{-1} for hydrocarbons, and 3640 to 4000 cm^{-1} for H_2O. Each species-specific, crank-angle-resolved absorption profile was then normalized by its

corresponding minimum and maximum values, excluding points near TDC due to the high fluctuations in this regime and consequent inaccuracy of the absorbance data. Absorption is proportional to temperature, so absorption of all gases tended to rise with compression and combustion before TDC, and fall with expansion after TDC, as is observed. Absorption is also proportional to species concentration, so the hydrocarbons absorbed primarily before TDC and the combustion products (CO2 and H2O) absorb primarily after TDC. These trends demonstrate that the combustion process is similar from one operating condition to the next.

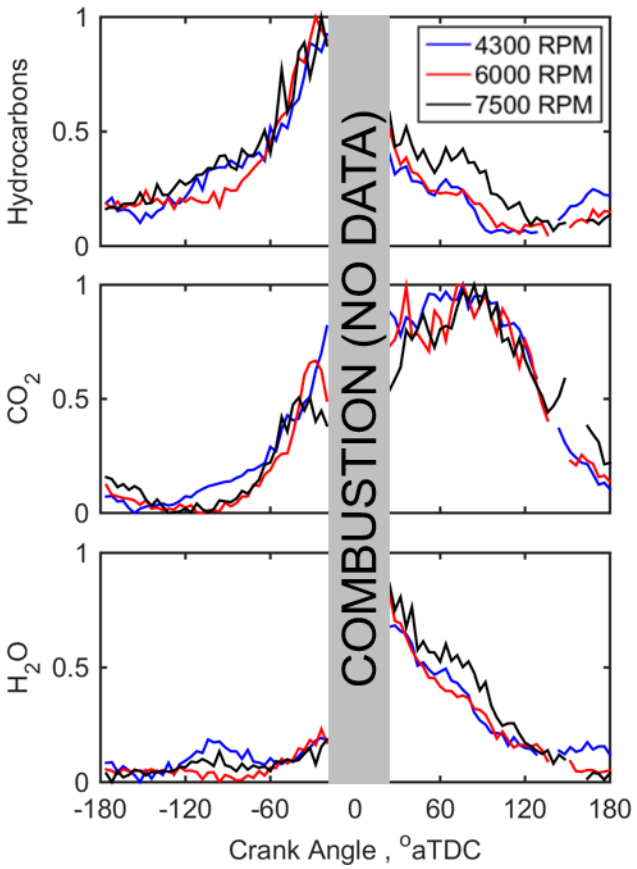

Figure 122. Qualitative species-specific absorption analysis.

5.3. Effect of Variable CA50

The dataset collected on 2 Feb 16 achieved the best SNR of any case in this research. The resulting temperature profiles are presented together in Figure 123. The results affirm what was suggested in Section 5.2: local maxima occur at approximately 60° aTDC. This region of the engine cycle is perhaps a tipping point between the effects of hot combustion gas being re-

circulated back into the combustion dome, thus driving the temperature in the line of sight of the optical probes to increase, and gas expansion driving the global temperature down. When advancing the combustion phasing one would expect to see the initial temperature rise to occur earlier and earlier in the engine cycle. This trend is observed in the data, and is highlighted in Figure 124. There is tight agreement among the three cases throughout the remainder of the engine cycle.

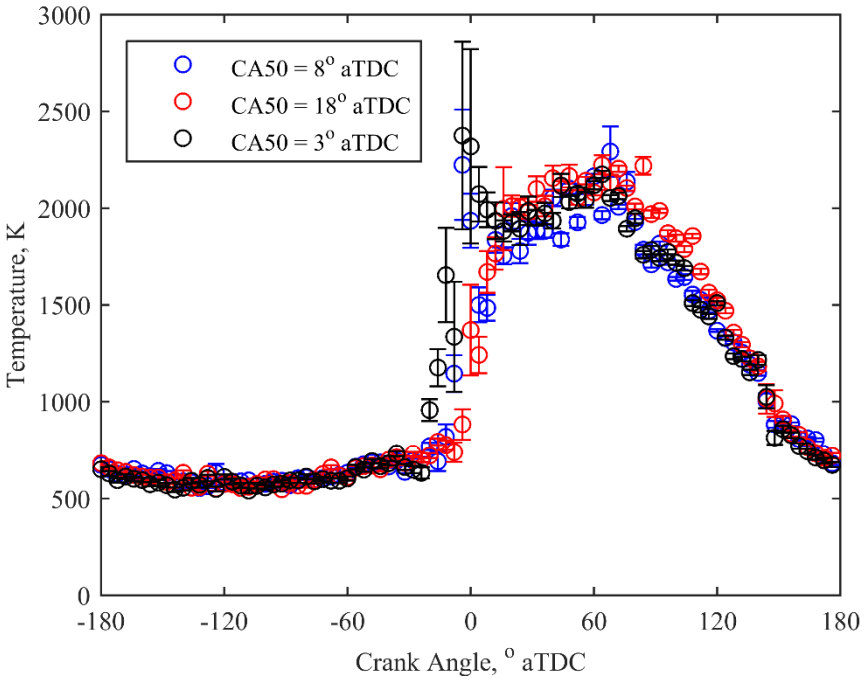

Figure 123. Comparison of temperature profiles when combustion phasing is varied.

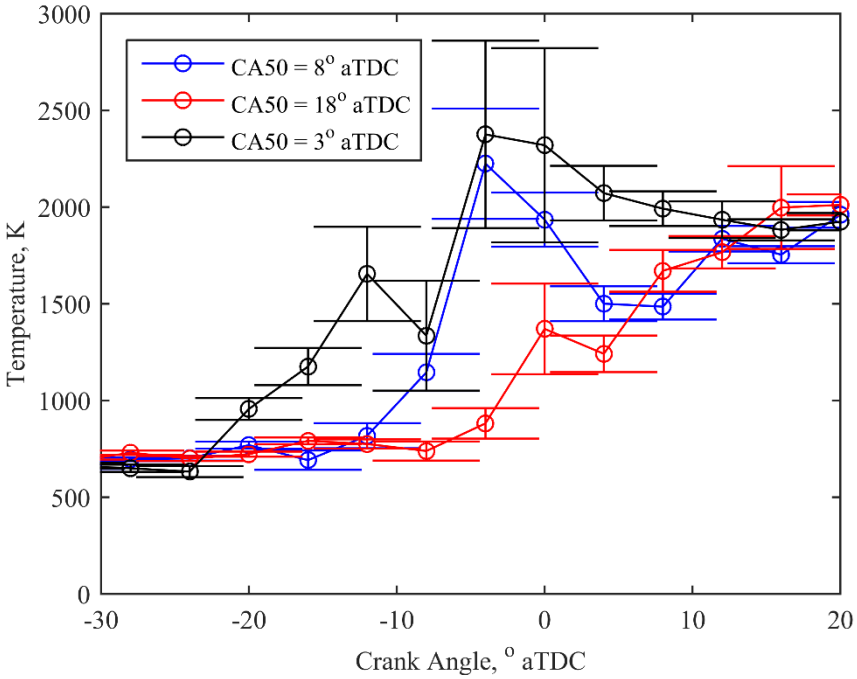

Figure 124. Comparison of temperature profiles when combustion phasing is varied. Close-up view of the portion of the engine cycle near TDC showing the phase shift of the temperature rise.

5.4. Effect of Fuel ON

A limited amount of data was collected running 20 ON fuel at what was otherwise the baseline condition on 28 Jan 16 before one of the optical probes failed and the experiment was terminated. Whereas a standard dataset consists of 3000 scans, this experiment was terminated after 940 scans. The limited number of scans resulted in a reduction in SNR, especially at and around TDC, but improvements in the experimental setup prior to that date resulted in this data having the best SNR observed up until that time. Figure 125 compares this 20 ON fuel dataset to the 98 ON fuel baseline collected on 2 Feb 16. The most noticeable difference between the two temperature profiles is that the 20 ON temperature profile does not have the same local maximum at 60° aTDC as does the 98 ON temperature profile. It is possible that such a maximum occurs earlier in the cycle but is lost in the noisy region between TDC and 60° aTDC. This would make sense because the more volatile 20 ON fuel would be expected to have a faster burn rate so the tipping point discussed in Section 5.3 would necessarily occur earlier in the

engine cycle. The two cases are essentially the same after the exhaust port opens at 103° aTDC and the pressure in the cylinder equalizes with atmospheric pressure.

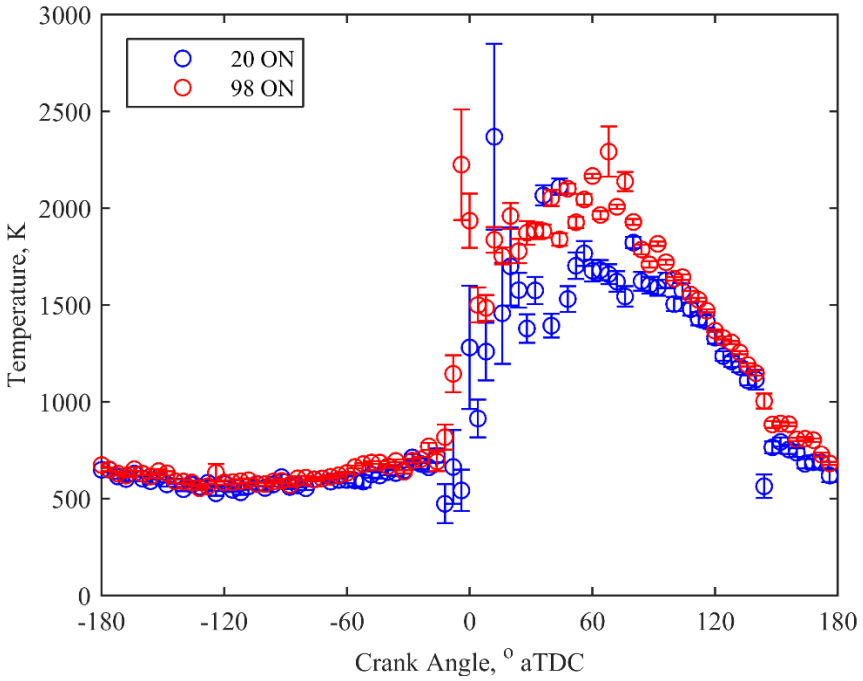

Figure 125. Comparison of temperature profiles when fuel ON is varied.

V. Conclusions

The primary objective of this research was accomplished. Crank-angle-resolved, in-cylinder, bulk gas temperature profiles were collected for several operating conditions and compared to gain insight into the combustion process, and how it is affected by operating speed, combustion phasing, and fuel octane number. Poor signal-to-noise ratio was the primary stumbling stone in the execution of this research. Were this research to be repeated, sapphire windows with greater diameters would be used for the optical access to the engine. The gains to be had in SNR far outweigh the risks of changing engine performance, ruining an engine head, or having to deal with the spark plug in the line of sight of the optical probes.

Suggested future work includes investigations into the effects of throttle setting, head temperature, equivalence ratio, and engine size. With the lessons learned from the present research effort, these investigations should be well within reach. FTIR absorption spectroscopy could also be applied to other cyclically repeatable combustion events. For example, FTIR could be used to determine species concentrations in the combustion wave that cycles through a rotary detonation engine.

Appendix A: Early Window Designs

The design of the combustion chamber windows required careful consideration of physical constraints. The choice of material had to satisfy stringent demands, including appropriate optical properties, material strength, and hardness. The shape of the windows had to be carefully designed to successfully direct the IR beam across the combustion chamber to the receiving fiber without losing an unacceptable level of signal, or corrupting the signal. Finally the engine had to be modified, and a probe designed to complement the window design, ensuring that the material strength of the engine was not compromised, the windows were secured, the geometry of the combustion chamber was preserved as best as possible, and the windows were relatively easy to install and remove.

Sapphire was chosen early-on to be the window material due to its material strength, hardness, favorable thermal expansion coefficient, and transmissivity in the IR. The shape of the windows would depend on the strategies adopted for securing and sealing the windows and managing interference of reflected beam paths with the primary beam path.

Ultimately, two window designs were selected: one for IR measurement techniques and one for tuned laser measurement techniques. Tuned laser measurement techniques require the windows to be as thin as possible. As windows become thinner, the effect of the absorption of the window material becomes less significant. However, the thinner a window becomes, the more the window must be wedged. Without a wedge, reflected beams are coincident with the primary beam. The beams interfere and cause distortion of the signal and resulting data.

A wedged window had to be designed to be thick enough that the pressure inside the combustion chamber and the stress of the clamping force that holds the window in place were not going to break the window, but also as thin as possible to minimize the absorption of the material. The window had to have a wedge with a great enough angle that the reflected beam would diverge from the incident beam with as little interference as possible, but small enough

that the beam was not refracted such that it was impossible to aim the beam at the window on the opposite side of the combustion dome.

The refraction required to minimize interference could conceivably be accomplished with a wedge on the inside of the window or the outside, or with a window with complementary wedges to create parallel planes. Each of these possibilities was explored to determine the most reasonable solution. The optimum wedge angle was determined for each variant. The final designs are shown in Figure 126 through Figure 128.

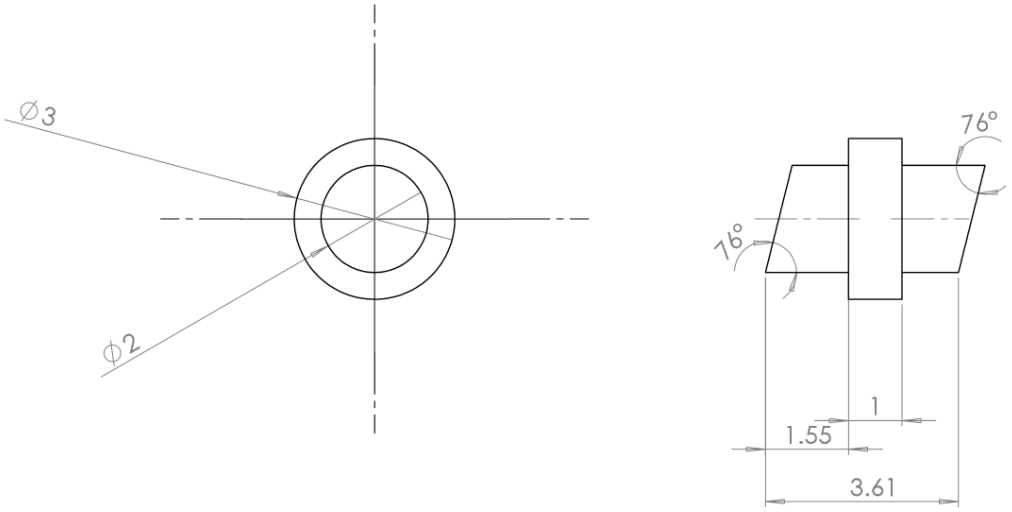

Figure 126. The design for the parallel-planes wedged window. All dimensions are in millimeters unless otherwise specified.

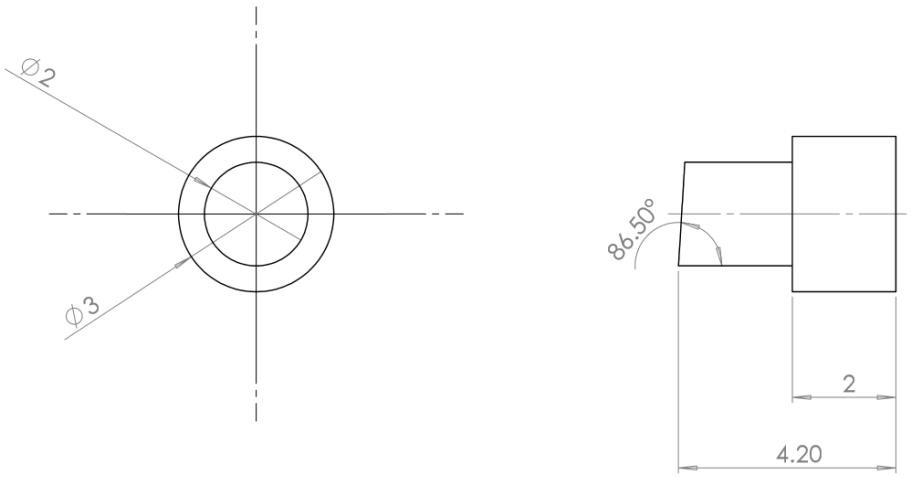

Figure 127. The design for the outer-wedge window. All dimensions are in millimeters unless otherwise specified.

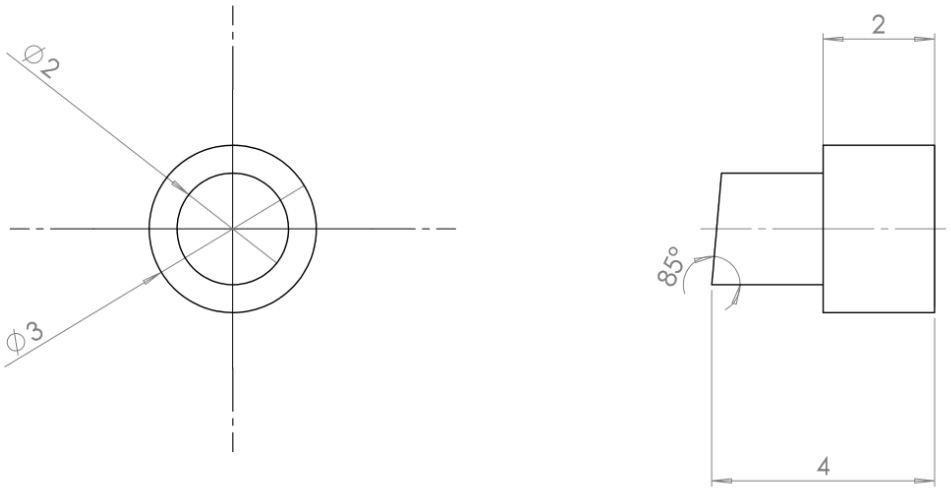

Figure 128. The design for the inner-wedge window. All dimensions are in millimeters unless otherwise specified.

Appendix B: Motored Operation

Crank-angle-resolved temperature for the motored condition was desired as a way to validate the data sorting and absorption spectral fitting processes. This experiment was complicated by several factors. First, the cycle speed was so much lower than what is observed at fired conditions that some of the data processing code had to be modified to handle the resulting data. Second, fuel-oil mixture had to be cycled through the engine in order to lubricate the piston ring and crank case, but the lower temperatures caused the oil to build up on optical surfaces and reduce signal through the engine. Third, motoring the engine can cause damage over time, so motored time was limited to 5 minutes even though 20 minutes were desired to collect an amount of data comparable to the fired conditions. Fourth, at the time this data set was taken, there was no way to purge the engine cylinder with nitrogen gas to collect an appropriate background sample so low-temperature data was all but lost when the background spectrum was divided out of the single-beam spectrum (see Figure 117). The experiment was further complicated by a failure to collect a pressure trace to complement the data, or note the atmospheric temperature and pressure. Finally, an error was made when performing the baseline correction of the absorbance spectra that led to errors in the results of the spectral fitting process. Some of these errors could be corrected retroactively, but the most important ones would require a new dataset. While it was not possible to re-visit this experiment to correct errors, it is discussed here as a learning experience.

The results of the motored test experiment are shown in Figure 129. The background spectrum used to calculate transmittance was almost identical to the spectra taken at low pressure because, at the time, the engine cylinder could not be purged with nitrogen gas. This meant that any of the features that might have been visible at low pressure and temperature were wiped out by the background, and little remained but noise to compare with simulated lines. This is why so many of the temperature estimations far away from 0° aTDC are scattered and unrealistic. Near 0° aTDC there is a recognizable trend that peaks at approximately 700 K. This trend appears

when the increased pressure and temperature in the compressed cylinder causes absorption features that are significantly stronger than those seen at atmospheric temperature and pressure, and are therefore not completely eliminated by dividing out the background. Assuming ideal gas, isentropic compression, and standard atmospheric conditions the peak temperature was estimated to be 560 K. The unreasonably high peak temperature found by spectral fitting may be attributed to the poor background scan and the error in baseline correction.

Much could be done to improve this dataset. A motored pressure trace could be collected now to replace the one generated by assuming an isentropic compression process. The error in baseline correction could be fixed. The optical setup from this experiment could be replicated to collect a background with a nitrogen purge through the cylinder. A background spectrum could even be approximated by manually removing features from the instrument line shape on the existing background spectrum. Any and all of these steps would improve the results shown below, but the purpose of this experiment was to check the data processing method against another temperature calculation, in this case an ideal gas approximation. To do this properly the experiment would have to be repeated entirely and this was unfortunately not possible due to time constraints. Despite being a “failure”, the experience gained from collecting this dataset was instrumental in bringing future success with experiments that were more aligned with the objectives of the research.

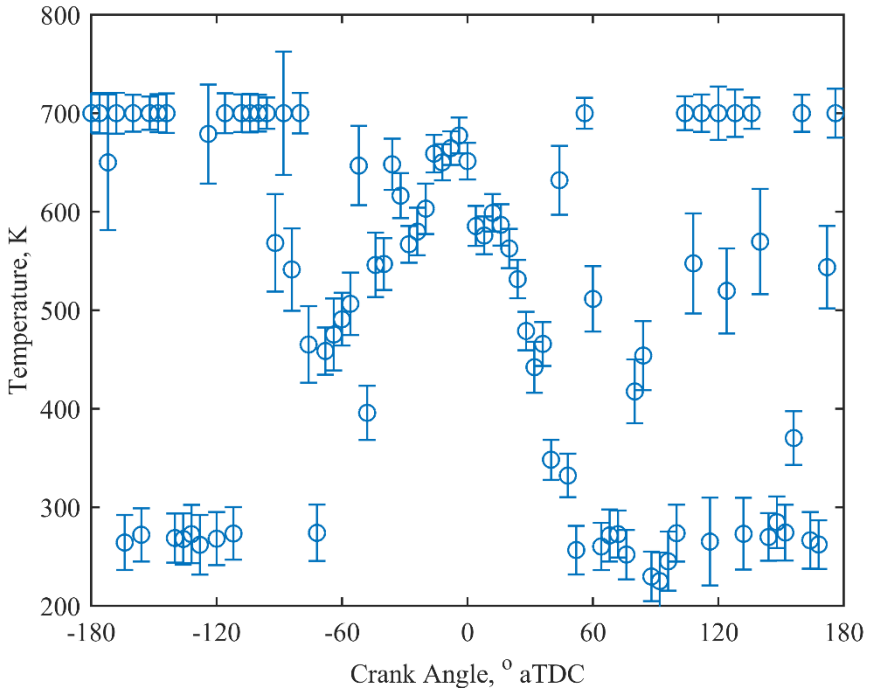

Figure 129. Attempt to generate a temperature profile for the motored engine.

Bibliography

[1] K. D. Rein and S. T. Sanders, "Fourier-transform absorption spectroscopy in reciprocating engines," *Applied Optics*, vol. 49, 2010.

[2] H. D. Young and R. A. Freedman, *University Physics*, 11th ed. San Francisco, CA: Pearson Education, Inc. Publishing as Addison Wesley, 2004.

[3] T. Gegg, A. Kölmel, and K. W. Beck, "Combustion Analysis on Small Two-Stroke SI-Engines for Handheld Power Tools," presented at the 2010 Small Engine Technology Conference, Linz, Austria, SAE Technical Paper 2010-32-0062, 2010, doi: 10.4271/2010-32-0062.

[4] A. W. Caswell, "Water Vapor Absorption Thermometry for Practical Combustion Applications," Doctor of Philosophy in Mechanical Engineering Ph D Dissertation, Department of Mechanical Engineering, University of Wisconsin - Madison, 2009.

[5] J. K. Ausserer, K. P. Horn, D. M. Polanka, P. J. Litke, and K. D. Grinstead, "Quantification of Short-Circuiting and Trapping Efficiency in a Small Internal Combustion Engine by GC-MS and GC-TCD," presented at the Small Engine Technology Conference, Osaka, Japan, 2015.

[6] S. Menon and C. Cadou, "Scaling of Miniature Piston-Engine Performance Part 1: Overall Engine Performance," *Journal of Propulsion and Power*, vol. 29, pp. 774-787, July-August 2013, doi: 10.2514/1.B34638.

[7] P. R. Griffiths and J. A. de Haseth, *Fourier Transform Infrared Spectrometry*, Second ed. Hoboken, New Jersey: John Wiley & Sons, Inc., 2007.

[8] K. D. Rein, S. T. Sanders, S. R. Lowry, E. Y. Jiang, and J. J. Workman, "In-cylinder Fourier-transform infrared spectroscopy," *Measurement Science and Technology*, vol. 19, p. 043001, 2008, doi: 10.1088/0957-0233/19/4/043001.

[9] D. Jenkins and B. Vasigh, "The Economic Impact of Unmanned Aircraft Systems Integration in the United States," Association for Unmanned Vehicle Systems International, Arlington, VirginiaMarch 2013.

[10] W. W. Pulkrabek, *Engineering Fundamentals of the Internal Combustion Engine*, Second Edition ed. Upper Saddle River, New Jersey 07458: Pearson Prentice-Hall, 2004.

[11] J. B. Heywood, *Internal Combustion Engine Fundamentals*. New York: McGraw-Hill, 1988.

[12] C. F. Taylor and T.-Y. Toong, "Heat Transfer in Internal Combustion Engines," presented at the ASME-AIChE Heat Transfer Conference, University Park, Pennsylvania, 57-HT--17, 1957.

[13] W. J. D. Annand, "Heat Transfer in the Cylinders of Reciprocating Internal Combustion Engines," *Thermodynamics and Fluids Group*, vol. 177, pp. 973-991, 1963, doi: 10.1243/PIME_PROC_1963_177_069_02799.

[14] T. LeFeuvre, P. S. Myers, and O. A. Uyehara, "Experimental Instantaneous Heat Fluxes in a Diesel Engine and Their Correlation," presented at the Mid-Year Meeting, Chicago, Illinois, SAE Technical Paper 690464, 1969, doi: 10.4271/690464.

[15] J. Dent and S. Sulaiman, "Convective and Radiative Heat Transfer in a High Swirl Direct Injection Diesel Engine," presented at the International Automotive Engineering Congress and Exposition, Detroit, Michigan, SAE Technical Paper 770407, 1977, doi: 10.4271/770407.

[16] J. K. Ausserer, P. J. Litke, J.-R. Groenewegen, A. Rowton, M. Polanka, and K. Grinstead, "Development of Test Bench and Characterization of Performance in Small Internal Combustion Engines," presented at the 19th Small Engine Technology Conference, Taipei, Taiwan, SAE Technical Paper 2013-32-9036, 2013, doi: 10.4271/2013-32-9036.

[17] J. K. Ausserer, M. Polanka, J. Rittenhouse, A. Rowton, P. Litke, and K. Grinstead, "Comparison of In-Cylinder Pressure Measurement Methods in a Small Spark Ignition Engine," presented at the 2014 SAE Small Engine Technology Conference, Pisa, Italy, SAE Technical Paper 2014-32-0007, 2014, doi: 10.4271/2014-32-0007.

[18] K. P. Horn, J. K. Ausserer, M. D. Polanka, P. J. Litke, and K. D. Grinstead, "Dynamic Friction Measurements on a Small Engine Test Bench," presented at the SciTech 2015, Kissimmee, Florida, AIAA 2015-1473, 2015.

[19] J. A. Rittenhouse, A. K. Rowton, J. K. Ausserer, and M. D. Polanka, "Preliminary Thermal Loss Measurements for a Small Internal Combustion Engine," presented at the SciTech 2014, National Harbor, MD, AIAA 2014-0529, 2014, doi: 10.2514/6.2014-0529.

[20] A. K. Rowton, J. K. Ausserer, K. D. Grinstead, P. J. Litke, and M. D. Polanka, "Measuring Scaling Effects in Small Two-Stroke Internal Combustion Engines," presented at the 2014 Small Engine Technology Conference & Exposition, Pisa, Italy, SAE Technical Paper 2014-32-0010, 2014, doi: 20.4271/2014-32-0010.

[21] H. Zhao, *Laser Diagnostics and Optical Measurement Techniques in Internal Combustion Engines*. Warrendale, PA: SAE International, 2012.

[22] K. D. Rein, "High-Resoltuion Spectroscopic Measurement of Small Molecules in Combustion," Ph.D. in Mechanical Engineering, Department of Mechanical Engineering, University of Wisconsin - Madison, Madison, Wisconsin, 2014.

[23] B. C. Smith, *Fundamentals of Fourier Transform Infrared Spectroscopy*. Boca Raton, Fl: CRC Press, 1996.

[24] S. P. Davis, M. C. Abrams, and J. W. Brault, *Fourier Transform Spectrometry*, First Edition ed. San Diego, CA: Academics Press, 2001.

[25] M. L. Boas, *Mathematical Methods in the Physical Sciences*, Third Edition ed. Hoboken, NJ: John Wiley & Sons, Inc., 2006.

[26] K. W. Beck, T. Heidenreich, S. Busch, U. Spicher, T. Gegg, and A. Kölmel, "Spectroscopic Measurements in Small Two-Stroke Engines," presented at the Small Engine Technology Conference, Penang, Malaysia, SAE Technical Paper - 2009-32-0030, 2009, doi: 10.4271/2009-32-0030.

[27] L. S. Rothman, I. E. Gordon, R. J. Barber, H. Dothe, R. R. Gamache, A. Goldman, *et al.*, "HITEMP, the high-temperature molecular spectroscopic database," *Journal of Quantitative Spectroscopy and Radiative Transfer*, vol. 111, pp. 2139-2150, 2010, doi: 10.1016/j.jqsrt.2010.05.001.

[28] K. P. Horn, "Exhaust Composition in a Small Internal Combustion Engine using FTIR Spectroscopy," Master of Science in Aeronautical Engineering Masters Thesis, Department of Aeronautical Engineering, Air Force Institute of Technology, 2015.

[29] P. R. Griffiths, "Photometric Precision in Infrared Spectra Measured by Fourier Transform Spectroscopy," *Applied Spectroscopy*, vol. 29, pp. 11-14, February 1975 1975.

[30] J. W. Cooley and J. W. Tukey, "An Algorithm for the Machine Calculation of Complex Fourier Series," *Mathematics of Computation*, vol. 19, pp. 297-301, April 1965 1965.

[31] L. Mertz, *Transformations in Optics*, 1st ed. New York: Wiley, 1965.

[32] L. Mertz, "Auxiliary computation for Fourier spectrometry," *Infrared Physics*, vol. 7, pp. 17-23, 1967, doi: 10.1016/0020-0891(67)90026-7.
[33] L. A. Kranendonk, A. W. Caswell, and S. T. Sanders, "Robust method for calculating temperature, pressure and absorber mole fraction from broadband spectra," *Applied Optics*, vol. 46, pp. 4117-24, 17571153, Jul 1 2007.
[34] S. A. Tashkun and V. I. Perevalov, "CDSD-4000: High-resolution, high-temperature carbon dioxide spectroscopic databank," *Journal of Quantitative Spectroscopy and Radiative Transfer*, vol. 112, pp. 1403-1410, 2011.
[35] M. R. Rhoby, D. L. Blunck, and K. C. Gross, "Mid-IR hyperspectral imaging of laminar flames for 2-D scalar values," *Opt Express*, vol. 22, pp. 21600-17, 25321539, Sep 8 2014, doi: 10.1364/OE.22.021600.
[36] A. Hamins, M. Bundy, and S. E. Dillon, "Characterization of Candle Flames," *Journal of Fire Protection Engineering*, vol. 15, pp. 265 - 285, November 2005 2005, doi: 10.1177/104239150505316.

REPORT DOCUMENTATION PAGE			Form Approved OMB No. 0704-0188

1. REPORT DATE (DD-MM-YYYY)	2. REPORT TYPE	3. DATES COVERED (From - To)
24-03-2016	Master's Thesis	September 2014 - March 2016

4. TITLE AND SUBTITLE
Spectroscopic Measurement of Gas Temperature in Small Internal Combustion Engines

5a. CONTRACT NUMBER

5b. GRANT NUMBER

5c. PROGRAM ELEMENT NUMBER

6. AUTHOR(S)
Deutsch, Matthew J., Capt

5d. PROJECT NUMBER

5e. TASK NUMBER

5f. WORK UNIT NUMBER

7. PERFORMING ORGANIZATION NAME(S) AND ADDRESS(ES)
Air Force Institute of Technology
Graduate School of Engineering and Management (AFIT/EN)
2950 Hobson Way
Wright-Patterson AFB OH 45433-7765

8. PERFORMING ORGANIZATION REPORT NUMBER
AFIT-ENY-MS-16-M-207

9. SPONSORING/MONITORING AGENCY NAME(S) AND ADDRESS(ES)
Air Force Research Laboratory
Mr. Paul J. Litke, PE
1950 Fifth Street, Bldg 490, Rm 115
Wright-Patterson AFB, OH 45433
paul.litke.3@us.af.mil

10. SPONSOR/MONITOR'S ACRONYM(S)
AFRL/RQTC

11. SPONSOR/MONITOR'S REPORT NUMBER(S)

12. DISTRIBUTION/AVAILABILITY STATEMENT
Distribution Statement A. Approved for Public Release; Distribution Unlimited

13. SUPPLEMENTARY NOTES
This work is declared a work of the U.S. Government and is not subject to copyright protection in the United States.

14. ABSTRACT
The Small Engine Research Bench (SERB) was used previously to measure spatially and temporally averaged heat flux, as well as local, instantaneous heat flux at several external locations, for a series of small engines (1 - 10 kW). This investigation obtained time averaged crank angle resolved measurements of the in-cylinder gas temperature using Fourier transform infrared (FTIR) absorption thermometry. The results, coupled with heat flux measurements, will enable the validation or refinement of existing thermal energy loss models.

15. SUBJECT TERMS
^Fourier Transform infrared; spectrometry; spectroscopy; internal combustion engine; optical engine; optical diagnostics

16. SECURITY CLASSIFICATION OF:			17. LIMITATION OF ABSTRACT	18. NUMBER OF PAGES	19a. NAME OF RESPONSIBLE PERSON
a. REPORT	b. ABSTRACT	c. THIS PAGE			Dr. Marc D. Polanka, AFIT/ENY
U	U	U	UU	173	19b. TELEPHONE NUMBER (Include area code) (937) 255-3636 x4714 marc.polanka@afit.edu